Title
Transient Vehicle Aerodynamics In Four-car Platoons

Authors
Chen, A. L.
Savas, Omer
Hedrick, Karl

Publication Date
1997

CALIFORNIA PATH PROGRAM
INSTITUTE OF TRANSPORTATION STUDIES
UNIVERSITY OF CALIFORNIA, BERKELEY

Transient Vehicle Aerodynamics in Four-Car Platoons

A.L. Chen, Omer Savas, Karl Hedrick
University of California, Berkeley

California PATH Research Report
UCB-ITS-PRR-97-50

This work was performed as part of the California PATH Program of the University of California, in cooperation with the State of California Business, Transportation, and Housing Agency, Department of Transportation; and the United States Department of Transportation, Federal Highway Administration.

Report for MOU 236

December 1997

ISSN 1055-1425

Transient Aerodynamics in Vehicle Interactions

A. L. Chen, J. K. Hedrick, and O. Savaş

Department of Mechanical Engineering

University of California at Berkeley

Berkeley, CA 94720-1740

California PATH Research Report

California PATH Program

Institute of Transportation Studies

University of California, Berkeley

December 1997

Transient Aerodynamics in Vehicle Interactions

A. L. Chen, J. K. Hedrick, and O. Savas

Department of Mechanical Engineering

University of California at Berkeley

Berkeley, CA 94720-1740

Abstract

When the time scale of a lane change maneuver in a platoon of vehicles is on the same order as the time scale of changes in the air flow over the vehicles, the transient forces and moments generated impact the controllability of the vehicles. To characterize these transient effects, measurements are made with a 4-car platoon of scale vehicle models in a wind tunnel. One of the vehicles moves laterally into and out of the platoon to simulate a lane change maneuver. The drag force, side force, and yawing moment on each of the 4 vehicles is measured for various configurations of the platoon. As one vehicle leaves or joins the platoon, the vehicles experience side forces on the same order as changes in the drag due to changes in the flow dynamics. In addition, the side forces experienced by a vehicle in the platoon depend upon the type of maneuver, leaving or joining, and the time scale of the maneuver. The yawing moments on the vehicles also show effects of the transient motion.

Keywords: platoon aerodynamics, bluff-body aerodynamics, bluff-body flow transient aerodynamics, unsteady aerodynamics

Executive Summary

The transient aerodynamic forces on automotive vehicles traveling in close proximity to each other are investigated in a wind tunnel. Scale vehicle models are longitudinally aligned in a "platoon" configuration with various separation distances between the models. One model is actuated such that it is capable of lateral motion at several accelerations with respect to the platoon. The location of the mobile model in the platoon is varied to simulate various lane changing maneuvers of full scale vehicles. The drag force, side force, and yawing moment are measured with strain gage balances to quantify the transient interactions of the vehicle flow fields.

Several important general trends can be observed. The drag coefficients for the vehicles in a platoon are lower than that of a single vehicle, and the coefficients decrease with smaller vehicle spacings. In addition, the drag coefficients on the remaining vehicles increase as a vehicle leaves the platoon. The side force coefficients also increase as a vehicle leaves the platoon. The increase in the side force is on the same order as the increase in the drag. The side force also increases with decreasing vehicle separation. Although the yawing moment is small and, thus, difficult to quantify, the moment also reflects influences of the transient flow field. A significant conclusion of the results is that the transient forces differ depending upon whether a vehicle leaves or joins a platoon. This hysteresis in the flow dynamics is not observable in steady-state measurements.

Several factors affect the magnitudes and behavior of the transient forces and moments, including the time scale of the maneuver, vehicle location in the platoon, vehicle separation, and vehicle shape and size. The effects of these parameters are discussed. These results also apply to the more general case of flow over bluff bodies.

Acknowledgments

We thank Philip Snyder and Lun Tsuei for their assistance.

Contents

List of Tables

List of Figures

Chapter 1

Introduction

This chapter provides an introduction to this investigation of transient aerodynamics of closely spaced vehicles. The background of the automated highway system, which this research directly impacts, is summarized. This research also applies to the fundamental study of bluff-body flow. An explanation of the necessity and application of the current study is provided. A brief review of past work applicable to the current study follows. Lastly, an overview of the present work is presented.

1.1 Background

As the population continues to grow, the problem of mass transportation in urban areas has become an increasing concern for all travelers. Buses, rail systems, and carpooling are mass transportation methods whose use has been encouraged to reduce the daily congestion on heavily used public routes. However, an increasingly larger number of cars continue to make transportation difficult for people in large metropolitan areas such as San Francisco and Los Angeles. Construction of new freeways and expansion of current routes are slow attempts to improve the traffic problem. These solutions are not only time consuming, but

also expensive and limited by the available land. The automated highway, an idea that was proposed as early as 1970 [1], has recently come to the forefront as computer, control, and communication technologies have improved. A conglomeration of various disciplines from universities, industry, and government have come together as the California Partners for Advanced Transit and Highways (PATH) to develop an automated highway system (AHS) [2].

In this system, once a vehicle enters the highway, an on-board computer directs the vehicle's path by communicating with the on-board computers of other vehicles already present on the highway and with roadside markers. California PATH proposes a system where "platoons" or convoys of up to twenty vehicles will travel as a unit by forming a single-file line of closely spaced vehicles, all traveling at the same high speed. By "platooning," the number of vehicles on a highway can be maximized, thereby increasing the "packing density" and the capacity of the highway. The AHS is expected to increase the current estimated highway capacity of 2000 vehicles/lane/hour by a factor of 2 to 6 [1]. The control algorithms being developed for the PATH automated highway system include the processes of following, longitudinal control, and lateral control. For accurate control and passenger safety, the aerodynamic forces encountered during the platoon maneuvers of leaving or joining, i.e. changing lanes, should be included in the vehicle controllers [1].

1.2 Motivation

In characterizing the aerodynamic behavior of road vehicles in isolation or in platoons, drag is perhaps the most important factor from the viewpoint of fuel economy. From a control and stability point of view, however, the side force and yawing moment are the most crucial aerodynamic characteristics of a vehicle. Several studies measuring these quantities

under steady conditions have been conducted. However, the magnitude of these quantities under unsteady conditions remains unexplored. *Unsteady* aerodynamics, in this study, is not the inherently unsteady nature of the flow at high Reynolds numbers and the associated unsteady forces, such as those due to vortex shedding. These forces and moments are steady in that their averages do not change in time. Their unsteady *(rms)* components are usually small fractions of their mean values, and hence, are easily handled by the vehicle control algorithms as random inputs.

The *transient aerodynamic forces and moments* in this study are those experienced by a vehicle during rapid changes in the configurations of closely spaced vehicles. Some possible cases are shown in Figure **1.1.** When a vehicle joins a platoon of vehicles from the rear, the aerodynamic forces on both the joining vehicle and the vehicle ahead of it change in a nonsymmetric way within the time scale of this maneuver. When a vehicle leaves the platoon, the situation is even more severe. If the lead vehicle leaves, the following vehicle will experience a sudden increase in drag, which is of the same order of magnitude as its previous drag, and a side force and yawing moment, which did not exist before. If the vehicle is an intermediate or trailing vehicle, the vehicle itself will experience forces and moments when it leaves the sanctuary of the streamlined flow pattern and crosses the shear layer into the unobstructed free stream. In addition, due to the instantaneous spacing generated, the neighboring vehicles will experience increased drag and side forces as well as yawing moments. These forces and moments are shown on one vehicle in Figure **1.1** as the drag D, side force S, and moment M. Similar unsteady aerodynamic effects result when light and heavy vehicles interact either within a platoon or during lane change and passing maneuvers as well as from wind gusts and wake turbulence.

A platoon may be considered a streamlined body with relatively low drag and no

significant yawing moments. When a vehicle leaves or joins the platoon, the streamlined flow pattern is distorted in a very short time period. Further this distortion occurs asymmetrically. Both the platoon and the maneuvering vehicle experience severe aerodynamic forces and moments over the time scale of the maneuvers. The transient side force and yawing moments, especially, may pose serious controllability problems in a very short time period and small space. As an example, consider the jerk a stationary car experiences when another car passes at close proximity. The mutual interaction forces will be proportional to the square of the relative velocity of the vehicles and strongly dependent on the proximity of the vehicles. Therefore, these forces are extremely important when the relative motion between the vehicles occurs at high speeds. Further, any realistic implementation of an intelligent vehicle/highway system (IVHS) will have to incorporate in its design the presence of different sized vehicles, such as sports cars and recreational vehicles.

1.3 Scope of Past Work

A recent extensive review of the aerodynamics of road vehicles is given by Hucho and Sovran [3]. An older collection of papers from a symposium addressing issues concerning road vehicle aerodynamics, including experimental and numerical studies, can be found in Sovran, et. al. [4]. Scibor-Rylski *[5]* discusses briefly the importance of considering transient aerodynamics, due to close proximity to walls or other vehicles or cross-winds, in vehicle dynamics and control.

Experiments conducted by Zabat, et. al. [6], [7] determined the aerodynamic characteristics for a platoon of vehicles under steady conditions. The drag, side force, and yawing moment for the vehicles in the platoon were measured for various inter-vehicle spacings. They found that the effects of the interacting flow fields increased as the spacing between

the vehicles decreased. **A** few studies have been conducted on the passing of a smaller vehicle by a larger vehicle [8], [9], [10]. These studies found that as a large vehicle passes a smaller one, the larger vehicle induces a side force and yawing moment on the smaller vehicle, which could result in loss of control. Other studies have attempted to simulate a passing maneuver with static measurements. In these experiments, a large vehicle was placed at different longitudinal and lateral spacings with respect to a smaller vehicle [11], [12]. These studies found that certain configurations resulted in large aerodynamic forces induced on the smaller vehicle, although they were not able to capture any transients.

The aerodynamics of road vehicles is essentially flow around bluff bodies. The majority of the studies have concentrated on the steady aerodynamic characteristics of bluff bodies in tandem, including various combinations of cylinders [13], [14], disks [15], boxes [16], and scale vehicle models [17]. Koenig and Roshko [18] performed experiments on a disk and cylinder in tandem. **A** review of data on two cylinders in tandem, lateral alignment, and staggered arrangements was performed by Zdravkovich [19]. The results of these studies showed that drag can be minimized for certain optimal configurations, while other configurations resulted in high values of drag and side forces.

A few studies have attempted to model the flow around a row of spheres as a potential flow [20]. Cai and Wallis [21] arrived at an analytical result. While the results of the above studies are useful, they do not address the problem of transient interactions between the bluff body or vehicle flow fields in viscous fluids. The present study differs from previous studies in that the transient aerodynamics are captured.

1.4 Overview of Present Work

The following issues are crucial to a successful implementation of IVHS in regards to control and safety. The transient aerodynamic drag, side forces, and yawing moment, both on a vehicle maneuvering in and out of a platoon and on the cruising members of the platoon, must be determined and dealt with by the vehicle controllers. The automatic vehicle control algorithms must be capable of handling all expected and unexpected side forces and moments. The side force and yawing moment generated by the unsteady aerodynamics can be extremely significant, especially when augmented by cross winds and gusts.

In order to provide accurate and reliable control algorithms, knowledge of the dynamics associated with these unsteady aerodynamics is critical. Specifically, the control algorithms require estimates of the magnitude and time scales of the forces and moments resulting from interaction of the vehicle flow fields in the fundamental system configurations. The effects of inter-vehicle spacing and location of the maneuvering vehicle are also important. To investigate these problems, experiments are performed in a low turbulence, low-speed wind tunnel on scale model vehicles. The forces and moments on a platoon of scale vehicles are measured to characterize the transient interaction of the flow fields. In addition, this problem can be generalized to the more fundamental problem of transient flow around bluff bodies in close proximity to each other.

The remainder of this document is organized into several sections. A brief discussion of transient aerodynamics and some scaling analysis is presented in the next chapter. The design of the experimental apparatus and the experimental procedure are described next. Results from the experiments and discussions follow. Finally, conclusions derived from this research and recommendations for further investigations are presented.

1.5 Figures

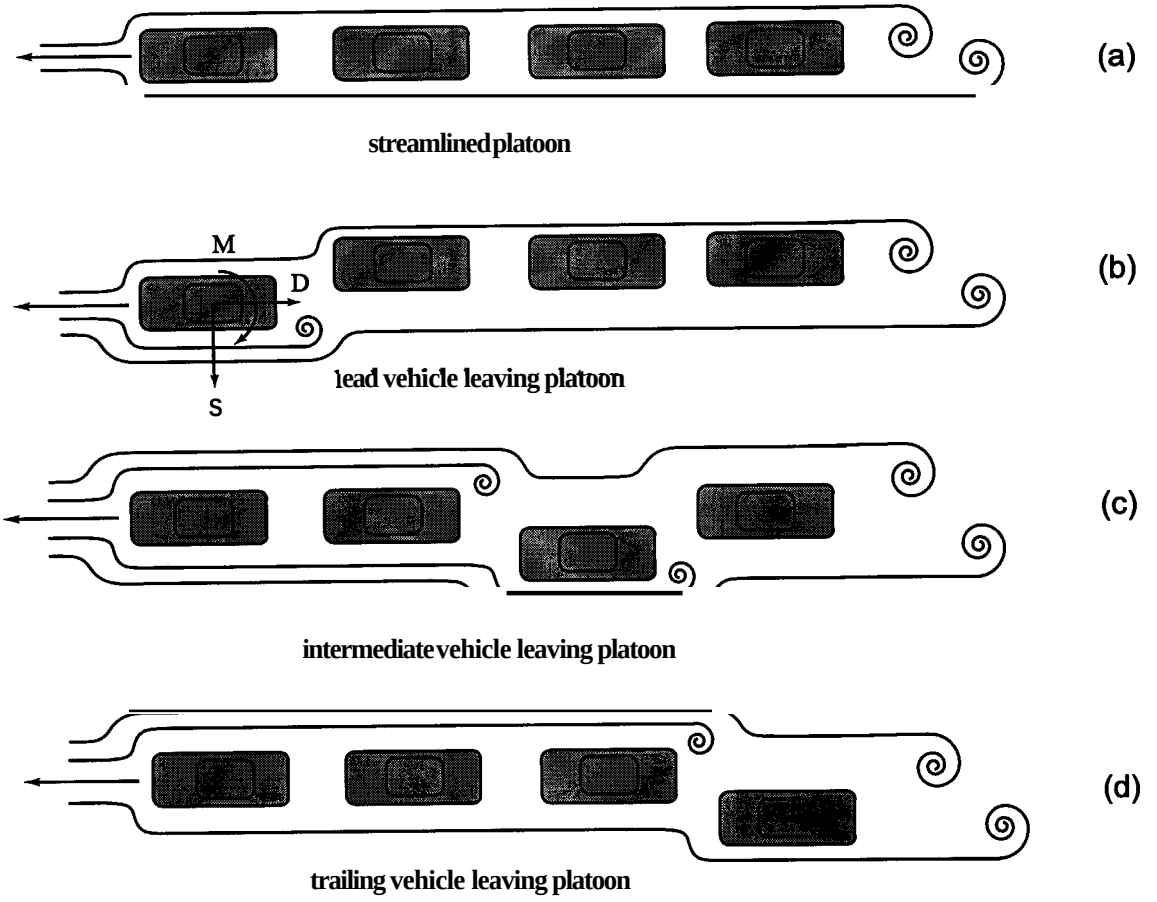

Figure 1.1: Platoon maneuvers.

Frame (a) shows the streamlined flow pattern of a platoon. Frames (b),(c),(d) show interruptions in the streamlined flow when the lead vehicle (b), an intermediate vehicle *(c)*, or the trailing vehicle (d) leaves the platoon.

Chapter 2

Theoretical Considerations

The basis of dynamic similarity is discussed. From a scaling analysis, the relevant flow parameters can be identified as described below. The transient aerodynamics are argued to depend upon a few identifiable variables, which are used in designing the experimental measurements. To compare the results of these measurements to the actual case, the aerodynamic forces and moments are nondimensionalized. In addition, by comparing the characteristic scales of the experiment to the actual flow, the required length and time scales for designing the experiment are determined.

2.1 Equations of Motion

The flow of Newtonian fluids is governed by the Navier-Stokes equations. In the absence of body forces and for incompressible flow, they can be written as [22]

$$\frac{\partial u_i}{\partial t} + u_j \frac{\partial u_i}{\partial x_j} = -\frac{1}{\rho}\frac{\partial p}{\partial x_i} + \nu \frac{\partial^2 u_i}{\partial x_j \partial x_j} \tag{2.1}$$

along with the continuity equation

$$\frac{\partial u_i}{\partial x_i} = 0 \tag{2.2}$$

where u_i is the velocity vector, t is the time, x_i are the spatial coordinates, ρ is the fluid density, p is the pressure, and ν is the kinematic viscosity of the fluid. Equations 2.1 and 2.2 are non-dimensionalized as

$$\frac{\partial u_i^*}{\partial t^*} + u_j^* \frac{\partial u_i^*}{\partial x_j^*} = -\frac{\partial p^*}{\partial x_i^*} + \frac{1}{Re} \frac{\partial^2 u_i^*}{\partial x_j^* \partial x_j^*} \tag{2.3}$$

and

$$\frac{\partial u_i^*}{\partial x_i^*} = 0 \tag{2.4}$$

where the variables are non-dimensionalized as

$$x_i^* = \frac{x_i}{l} \tag{2.5}$$

$$t^* = \frac{t}{l/U} \tag{2.6}$$

$$u_i^* = \frac{u_i}{U} \tag{2.7}$$

$$p^* = \frac{p - p_\infty}{\rho U^2} \tag{2.8}$$

using the length and velocity scales l and U, respectively. In this exercise, the pressure p is scaled with the dynamic head ρU^2 in anticipation of inertia dominated flow fields. The only free parameter of the flow is the Reynolds number defined as

$$Re = \frac{Ul}{\nu} \tag{2.9}$$

which uniquely identifies a flow from a family of flows in similar geometries. To achieve similarity between a flow and its scaled model, Equation 2.3 must be the same for both flows. This requirement implies that the nondimensional parameters in Equations 2.5-2.8 must also be the same for both flows. A non-dimensional time scale can be identified as Equation 2.6. This time scale can be used in a similarity analysis to compare the actual flow conditions with the experimental conditions.

2.2 Incomplete Similarity

For complete dynamic similarity, in addition to geometric similarity, the Reynolds number Re, defined in Equation 2.9, in the experiments must be the same as that of the full scale flow. However, this is often not achievable in the laboratory. In this case, the experiments are conducted at $Re = O(10^5)$ while the full scale flow is at $Re = O(10^7)$, two orders of magnitude higher. Despite the mismatch, the Reynolds number in both cases are sufficiently high that the inertia forces dominate the viscous forces, except in boundary layers. Since the models are bluff bodies, i.e. not streamlined, the flow separates over them; hence, the forces are mostly due to pressure differences over various parts of the bodies. Thus, to achieve similarity between the dynamic variables, the separation patterns on both the model and the actual object must be the same. Separation of the flow is determined by the behavior of the boundary layers. Laminar boundary layers, which occur at low Reynolds number, are more susceptible to early separation along a wall than a turbulent boundary layer, which has more energy to overcome an adverse pressure gradient, over the same wall at higher Reynolds numbers. The boundary layers over the models are expected to be laminar due to the low Reynolds numbers in the experiments. To overcome this problem, the boundary layers are tripped and made turbulent by using pinked strips of tape (discussed further in Section 3.1). Thus, these experiments are conducted in the *incomplete Reynolds number similarity* regime. Since the forces are mostly due to pressure differences, which are relatively insensitive to changes in the Reynolds number at high Reynolds number, the wind tunnel results should realistically simulate the actual flow.

To compare quantities for different flows, nondimensional parameters are defined. The measured transient aerodynamic forces are nondimensionalized by defining force and moment coefficients. A drag coefficient C_D is defined by scaling the drag force with the

dynamic head as

$$C_D = \frac{D}{\frac{1}{2}\rho U^2 A_f} \tag{2.10}$$

where D is the drag force and A_f is the frontal area exposed to the oncoming flow. In this case, the frontal area is

$$A_f = wh \tag{2.11}$$

where w is the width and h is the height of the body displacing the fluid. Similarly, a side force coefficient C_S is defined as

$$C_S = \frac{S}{\frac{1}{2}\rho U^2 A_f} \tag{2.12}$$

where S is the side force. A moment coefficient C_M is defined as

$$C_M = \frac{M}{\frac{1}{2}\rho U^2 V} \tag{2.13}$$

where M is the moment. Here, the moment is scaled with the volume V of the body where

$$V = A_f l \tag{2.14}$$

and l is the length of the body. These nondimensional force and moment coefficients will characterize the transient aerodynamics measured in the different experimental cases and can be applied to the full scale case.

2.3 Model Scaling

The focus of this work is on the transient aerodynamics. Using Equation 2.6, the time scale of the transient events in the actual flow can be compared to those in the experiments as

$$t^* = \left(\frac{Ut}{l}\right)_a = \left(\frac{Ut}{l}\right)_m \tag{2.15}$$

where the subscripts a and m refer to the actual and model cases, respectively. The time scale for the flow around a scale vehicle model can be expressed as

$$t_m = \left(\frac{r_l}{r_v}\right) t_a \tag{2.16}$$

where the ratio of the length scales r_l is defined as

$$r_l = \frac{l_m}{l_a} \tag{2.17}$$

and the ratio of the velocity scales r_v is defined as

$$r_v = \frac{U_m}{U_a} \tag{2.18}$$

Equation 2.16 shows that the relevant parameters in relating the experimental conditions to the actual conditions are the length ratio and velocity ratio. The current time estimate of platoon maneuvers, such as a lane change, is on the order of 5 seconds [23]. Therefore, from Equation 2.16, a 5 second lane change maneuver at a highway velocity of 30 m/s for full scale vehicles would be equivalent to a 0.4 second maneuver by a 1/20 scale model in a wind tunnel with a flow velocity of 20 m/s. Thus, achieving small time scales with the vehicle models is critical to obtaining results which will reflect the actual situation.

2.4 Accelerating Flows

In the case of high Reynolds number flows where inertial forces are dominant ($Re \gg 1$), the viscous term in Equation 2.1 may be ignored in describing the far flow field. Under such conditions, if the vortical layers are also excluded, potential theory may be invoked to examine the forces on a body. At the Reynolds numbers of these experiments, this assumption is justifiable since the time scales for the development of the vortical boundary layers are much shorter than the time scales of the transient events of interest [24]. The

magnitude of inertial forces during accelerations may be estimated using potential flow theory. The pressure field in a potential flow field can be determined from the unsteady Bernoulli equation [22] which can be deduced from Equation 2.1, subject to the assumptions in Section 2.1

$$\frac{\partial \phi}{at} + \frac{1}{2}u^2 + \frac{P}{\rho} = constant \tag{2.19}$$

where ϕ is the unsteady potential function whose gradient is the velocity vector

$$u_i = \partial\phi/\partial x_i \tag{2.20}$$

and u is the magnitude of the velocity vector u_i

$$u^2 = u_i u_i \tag{2.21}$$

The force on the body is determined from an integration of the pressure distribution acting over the body surface

$$F_i = \int_S -p\, dA_i \tag{2.22}$$

For a finite body moving in pure translation (no rotation), this expression reduces to

$$F_i = -\rho V \alpha_{ij} \frac{dU_j}{dt} \tag{2.23}$$

where α_{ij} is the body-shape tensor and dU_j/dt the rate of change of the free stream velocity components. The body-shape tensor α_{ij} is defined as

$$\alpha_{ij} = \frac{-1}{V} \int \Phi_j dA_i \tag{2.24}$$

where Φ_j is a vector function which satisfies the solenoidal boundary conditions on the body surface and is a function of geometry only, i.e. $\phi = U_i \Phi_i$. For example, for a sphere,

$$\alpha_{ij} = \frac{1}{2}\delta_{ij} \tag{2.25}$$

where δ_{ij} is the Kronecker delta. Thus, the sphere experiences a force equivalent to accelerating at the same rate half the amount of fluid displaced by it. This is also known as the *virtual muss* [22].

2.5 Transient Aerodynamic Parameters

In its most general form, one expects the transient force on vehicle i during an interaction to be a rather complex function of many variables (see Table **2.1** and Figure **2.1** for definitions of the symbols):

$$F_i(t) = f(t; \rho, U_1, U_2, L_1, L_2, l_l, d, W_1, W_2) \tag{2.26}$$

First, defining some equivalent variables for convenience

$$F_i(t) = F_i(t; \rho, u_s, U_i, L_i, l_s, d, w_s, W_i) \tag{2.27}$$

The usual procedure of constructing dimensionless groups yields

$$C_{F,i}(\tau) = C_{F,i}(\tau; \tfrac{U_i}{u_s}, \Delta, \tfrac{L_i}{l_s}, \tfrac{W_i}{l_s}, \tfrac{w_s}{l_s}) \tag{2.28}$$

In the special case of the interaction of identical vehicles of a certain aspect ratio, this functional form reduces to

$$C_{F,i}(\tau) = C_{F,i}(\tau; \tfrac{U_i}{u_s}, \Delta) \tag{2.29}$$

Even with these simplifications, the aerodynamic characteristics are functions of three independent groups. **A** careful examination of the problem suggests identifying a few typical speed parameters U_i/u_s and concentrating on those flow conditions. This simplifies the task of describing the aerodynamic parameters as functions of two independent variables, the interaction time τ and the separation of vehicles **A,** as

$$C_{F,i}(\tau) = C_{F,i}(\tau; \Delta) \tag{2.30}$$

for the drag and side force coefficients and

$$C_{M,i}(\tau) = C_{M,i}(\tau; \Delta) \tag{2.31}$$

for the moment coefficients.

2.6 Tables & Figures

parameter	symbol
vehicle length	L_i
vehicle width	W_i
vehicle frontal area	A_f
vehicle volume	V
platoon length	L_p
platoon width	W_p
lateral vehicle separation	d
longitudinal vehicle separation	l_l
vehicle speed, velocity	$U_i, \vec{U}_i$
interaction time	t
density of air	ρ
transient force on vehicle	F_i
transient moment on vehicle	M_i
longitudinal interaction length scale	$l_s = L_p, l_l + L_1 + L_2$
lateral interaction length scale	$w_s = d + W_p, d + W_1 + W_2$
relative speed	$u_s = \lvert \vec{U}_1 - \vec{U}_2 \rvert$
interaction time scale	$\tau_l = l_s / u_s$
dimensionless vehicle separation	$\Delta = d / l_s$
dimensionless interaction time	$\tau = t / \tau_l$
transient force coefficient	$C_{F,i} = \frac{F_i}{\frac{1}{2}\rho u^2 A_f}$
transient moment coefficient	$C_{M,i} = \frac{M_i}{\frac{1}{2}\rho u^2 V}$

Table 2.1: Interaction parameters.

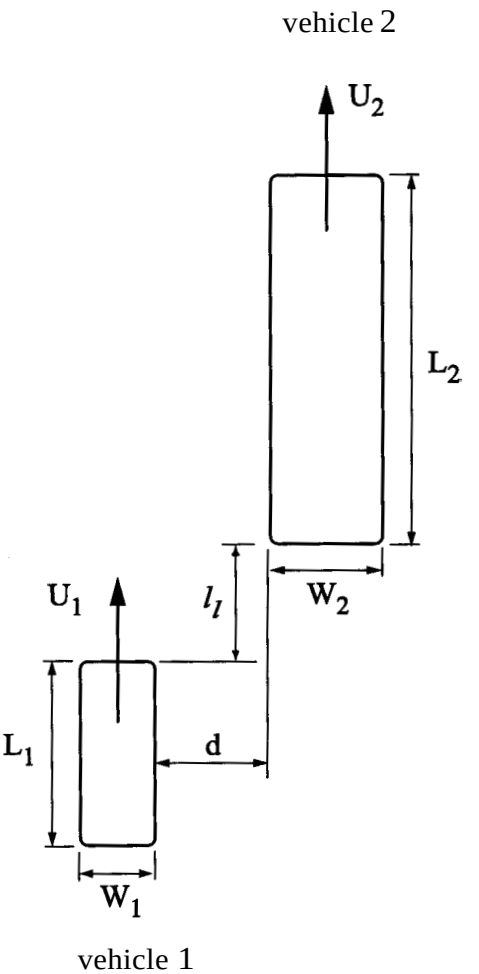

Figure 2.1: Aerodynamic parameters.

Parameters affecting transient aerodynamics on closely spaced vehicles.

Chapter 3

Experimental Apparatus

The simulation of vehicle maneuvers in a platoon requires the careful design and construction of numerous parts, including the scale vehicle models, sensors for the force measurements, a method for actuating the scale models, and a data acquisition system. The design considerations of these and the other parts of the experimental apparatus are described in the following sections. **All** machining, unless otherwise specified, was performed in-house by the Mechanical Engineering Machine Shop of the University of California, Berkeley.

3.1 Scale Models

The 1997 Buick LeSabre is used in these experiments as a representative vehicle shape and size. Specifications for the 1997 Buick LeSabre and the scale model appear in Table **3.1.** Scaling the vehicle down to 1/20 of full scale allows a platoon consisting of four vehicles spaced at one vehicle length apart to be placed in the wind tunnel. This arrangement also allows a lateral separation of 2.5 vehicle widths between a vehicle model and the platoon when a model leaves the platoon to simulate a lane change. In addition, since the ratio of

aerodynamic force to inertial force increases with the cube of the size but decreases with the mass, the scale models should be kept small and light.

The models were constructed by the General Motors Buick subcontractor Modern Engineering located in Troy, MI. Surface coordinates for the 1/20 scale vehicle models are generated from surface data of the full scale vehicle. With the scaled data, a master model is created by stereolithography (SLA). This process involves the solidification of a liquid polymer in successive layers by a computer controlled laser. Since the laser's motion is programmed with the coordinates of the vehicle surface, an extremely accurate 1/20 scale replication of the full scale vehicle is produced. Wheels and wheel-wells are molded into the vehicle exterior. All exterior details such as mirrors and windshield wipers are removed. The vehicle undercarriage is left open and later covered by aluminum plates. Negative RTV molds are produced from the SLA master, and hollow fiberglass replicas of the master are produced from the molds. An aluminum plate is mounted in the interior of each model for attachment of the force sensor. Four access holes are drilled into the surface of each model. The finished scale model weighs **412 g.** The models are painted with an automotive quality matte finish for flow visualization. The completed model appears in Figure **3.1.**

Also apparent in Figure **3.1** is the pinked tape used to trip the boundary layer on the model surface. The thickness of the tape ranges from 0.18 - 1.4 mm. Various thicknesses are obtained by plying layers of PVC electrical tape. The tape introduces known roughness elements to the surface which make the boundary layer turbulent and thus, keep the flow attached over a greater length of the model surface. Therefore, the forces on the model are a result of pressure differences, as are those in the full scale case.

3.2 Force Balances

The balances are constructed from **17-4** precipitation hardened (PH) stainless steel using electric-discharge machining (EDM). One of the force balances is shown in Figure **3.2.** The overall dimensions of the balance are **6.99** cm **(2.75** in.) x **6.99** cm **(2.75** in.) x **1.27** cm **(0.5** in). Each flexure measures **0.178** mm **(0.007** in.) in thickness. This design allows the simultaneous measurement of the drag force, side force, and yawing moment with no electrical cross-talk and minimal mechanical cross-talk between the force measurements [6]. Two arms measure the force in one direction, while two perpendicular arms measure the force in a perpendicular direction. Sixteen **350** Ω strain gages (etched advance/constantan foil grid on cast polyimide backing) are mounted on the arms and wired into three Wheatstone bridges to measure the strain on the thin flexures resulting from the aerodynamic forces on the vehicle. The gages measure **2.79** mm **(0.110** in.) in length and **1.27** mm **(0.050** in.) in width. The gages were mounted and wired by JP Technologies located in San Bernardino, **CA.** The configuration of the gages and the wiring diagrams of the full Wheatstone bridges are shown in Figure **3.3.** Two gages are mounted at each end of the two side arms (a total of four gages) and wired into a Wheatstone bridge to measure the drag force. Two gages are mounted at the end of the top and bottom arms (a total of four gages) and wired to measure the side force. Eight gages mounted and wired around the center of the balance measure the yawing moment. Thus, all of the circuits are independent.

A 9.5 cm **(3.75** in.) x **7.2** cm **(2.83** in.) rectangular cavity in the bottom **of** the scale model allows the balance to fit completely inside. **As** shown in Figure **3.2,** two arms of the balance are attached to an aluminum plate mounted in the interior of the vehicle model. The remaining two arms of the balance are attached to the wind tunnel floor. These arms are mounted on spacers, a cover plate, and streamlined struts. This design allows the

model to "float" on the balance and allows the balance to measure the aerodynamic forces experienced by the model. When the model is mounted on the balance, only the streamlined struts are exposed to the flow, resulting in minimal interruption of the flow underneath the model. No viscous damping is applied to the system.

3.3 Wind Tunnel Actuator

As discussed in Section 2.3, the model simulating a lane change requires a high acceleration. To enable a model to move laterally with respect to the vehicle platoon, an actuating device called the Wind Tunnel Actuator (WTA) was designed and constructed. The WTA is shown in Figure **3.4** and its various components are described below. The WTA has a width of 81 cm (width of the wind tunnel test section) and fits underneath the test section. To achieve the high acceleration required, the main concern in designing the WTA was minimizing the system inertia. The WTA is a motor driven belt system. A 5 hp **DC** brushless servo motor (Compumotor APEX **630)** drives a main wheel which has a steel belt attached. The belt is attached to a carriage which travels linearly along guide rails. The model which simulates the lane change and its instrumentation are attached to the carriage.

The motor was sized with several considerations, including an initial estimate of the system inertia and acceleration requirements of the model. Motion of the motor is dictated through software control of the motor hardware control box (Compumotor APEX **6154).** The main drive wheel has a diameter of 25.4 cm and is sized to allow the carriage to move either to the left or to the right with less than a 1/2 turn of the wheel. The wheel is constructed of 7070 aluminum and designed to minimize its rotational inertial without compromising strength.

The steel belt is made of tempered carbon steel and measures 0.002 inches thick. The belt is attached to the main wheel with a small tensioning post. The tensioning post is shown in Figure **3.5.** The design of the post incorporates some spring or flexibility in the side arms to allow increased tension to be applied without risking breakage of the belt. These pieces are constructed from A-10 air hardened carbon steel by EDM, Additional tension can be applied to the belt with a tensioning roller as shown in Figure **3.6.** Various amounts of tension are achieved with the design of placing the center of the roller eccentric from the center of its holder. The amount of tension applied to the belt can be adjusted by rotating the holder to different angles, thereby changing the vertical location of the roller. The other rollers in the system are constructed from hollow cylinders with press-fit ends to minimize their rotational inertia.

The traversing carriage is shown in Figure **3.7.** The carriage is constructed of **7070** aluminum by EDM and was designed with minimal mass. Smooth and quick motion of the carriage is achieved with steel ball bearings traveling on ground, case-hardened steel rails. With a scale model and its instrumentation mounted on the carriage, the WTA has a maximum acceleration of **15.6** m/s^2, well beyond the required acceleration of **3.9** m/s^2 to simulate a lane change in 0.5 seconds, which is equivalent to a 5-second lane change in the full scale case.

3.4 Wind Tunnel

A schematic of the low turbulence wind tunnel located in the Fluid Mechanics Laboratory of the University of California at Berkeley is shown in Figure **3.8.** The test section measures **3.65** m in length and has a cross section of 81 cm x 81 cm. The tunnel is an open return system. A schematic of the wind tunnel control system is shown in Figure **3.9.**

The wind tunnel velocity is controlled through a personal computer and can be set at a maximum velocity of 20 m/s. The specified velocity is maintained by a pressure feedback loop.

For these experiments, the ground plane is modified to accommodate **a** four vehicle platoon. The ground plane consists of modular sections which allow maximum flexibility in the placement of the vehicle models in the tunnel. The vehicle models are mounted at various separation distances, and the mobile model can be any one of the four vehicles in the platoon. In addition, the first 6 inches of the ground plane is replaced with a suction box for removal of the boundary layer at the test section entrance.

3.5 Data Acquisition

To quantify the transient aerodynamic forces resulting from the interaction of the flow fields on the vehicles in the platoon, the drag force, side force, and yawing moment for each vehicle model are measured with a force balance. In addition, to determine the inertial force of the moving model, information on the motion of the scale model is obtained from three sources: an encoder, a resolver, and an accelerometer. Position information is obtained from an optical encoder mounted on the motor rotor and from the resolver of the motor controller, and acceleration information is obtained from an accelerometer mounted on the moving scale model. The tunnel dynamic pressure is also measured. Therefore, for a platoon consisting of four vehicles, the experiments require the continuous and simultaneous acquisition of 16 signals. A brief description of the data acquisition system is provided here. Additional details can be found in Snyder [25].

A 16-bit, 8 channel, 200 kHz analog-to-digital (A/D) board (Analogic DVX-2502) is used in conjunction with a 200 kHz, 16 channel multiplexer with simultaneous sample-and-

hold (Analogic DVX-2601) in a workstation (Solbourne 601) for data acquisition. Software is written in **C** to allow flexibility in specifying the sampling rate of each channel. To measure the position of the mobile model with a high degree of accuracy, the encoder and resolver signals are sampled at 14 times the sampling rate of the remaining channels. To obtain the higher sampling rate for the encoder and resolver, the encoder and resolver signals are sent directly to the A/D board, while the other channels are first sent to the simultaneous sample-and-hold multiplexer. An algorithm was developed which samples the faster channels each time before sampling one of the slower channels, until all of the remaining 14 channels are read. The encoder and resolver are sampled at a rate of 72.8 **kHz,** while the other 14 channels are sampled at a rate of 5.2 kHz.

Before amplification and acquisition by the data acquisition system, the signals from the force balances are each passed through a wide bandwidth strain gage signal conditioner (Analog Devices 1B31AN) to filter out high frequency noise. In addition, various noise reduction techniques are used such as grounding of electrically conducting structures and low pass signal filters.

3.6 Tables & Figures

dimensions	car	model
vehicle length	5.1 m	25.5 cm
vehicle width	1.9 m	9.4 cm
vehicle height	1.4 m	7.1 cm
ground clearance	0.26 m	1.3 cm

Table 3.1: 1997 Buick LeSabre dimensions.

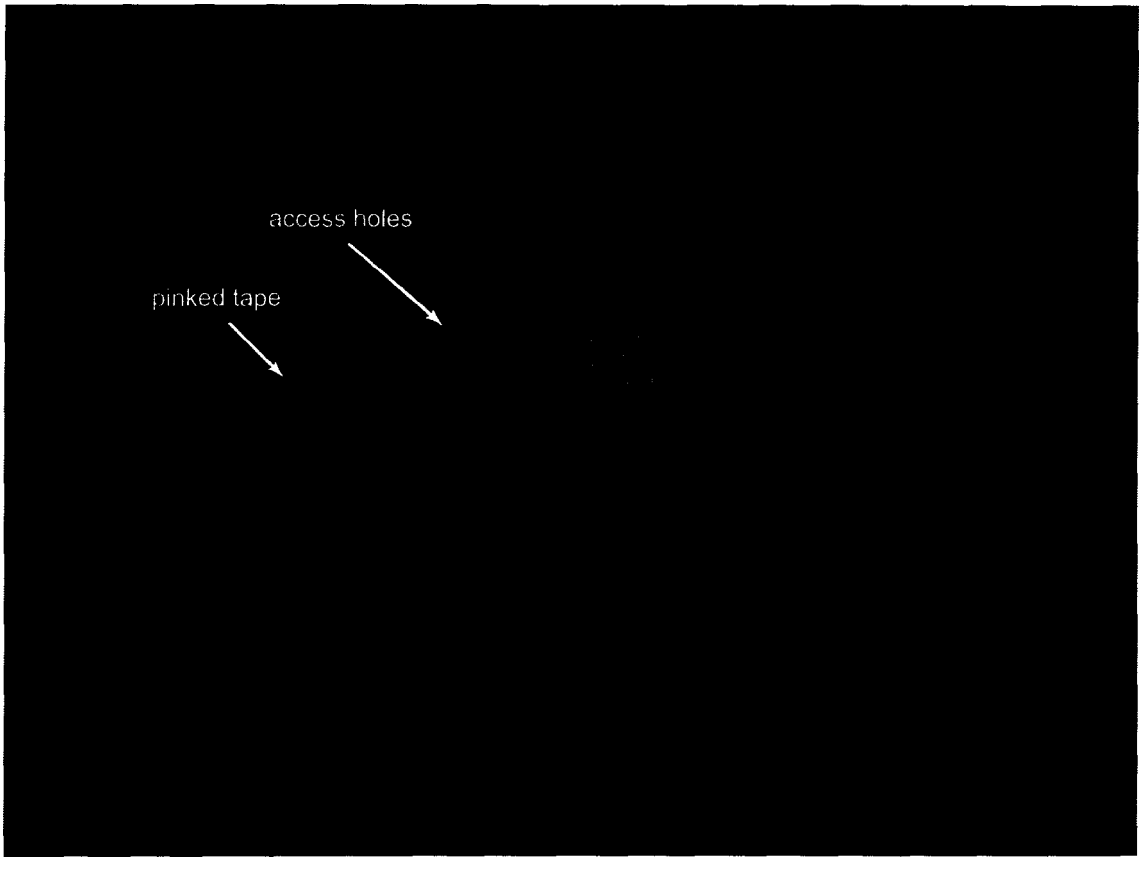

Figure 3.1: Scale model.

Photograph of the 1/20 scale model of the Buick LeSabre used in the wind tunnel experiments. The model measures 25.5 cm in length, 9.4 cm in width, and 7.1 cm in height.

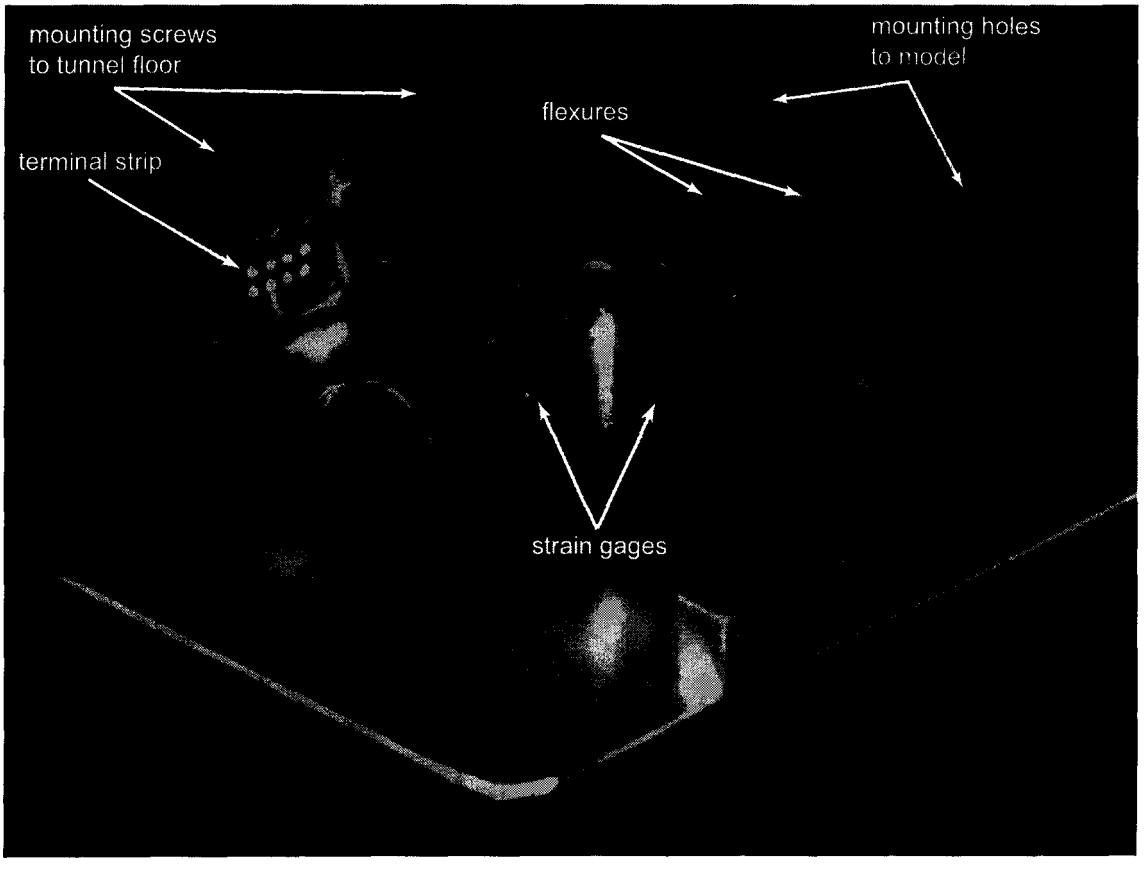

Figure **3.2:** Force balance.

Photograph of a force balance used to measure aerodynamic forces and moments on the models. The balance has dimensions of 6.99 cm x 6.99 cm x 1.27 cm. The flexure thickness is 0.178 mm. Sixteen strain gages are mounted on the flexures.

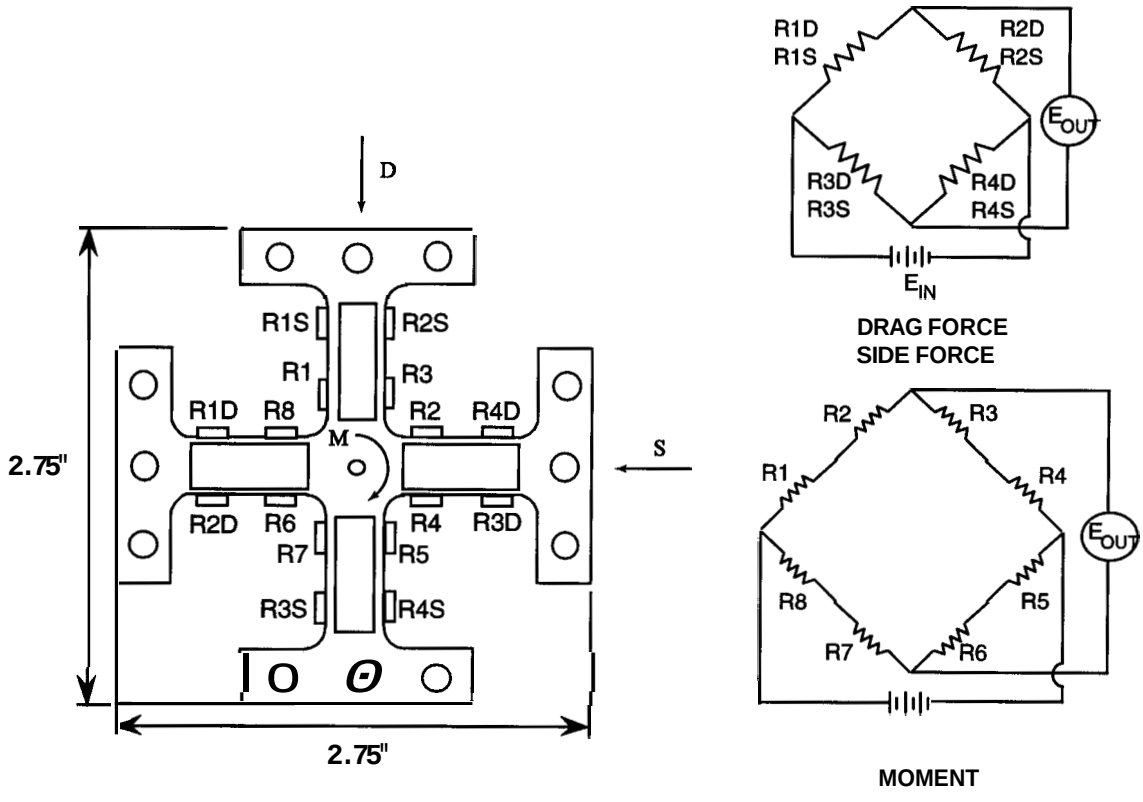

Figure **3.3:** Force balance wiring diagram.

Sixteen strain gages are wired into three full Wheatstone bridges. Four gages are wired together to measure the drag force, four gages are wired to measure the side force, and eight gages are wired to measure the yawing moment.

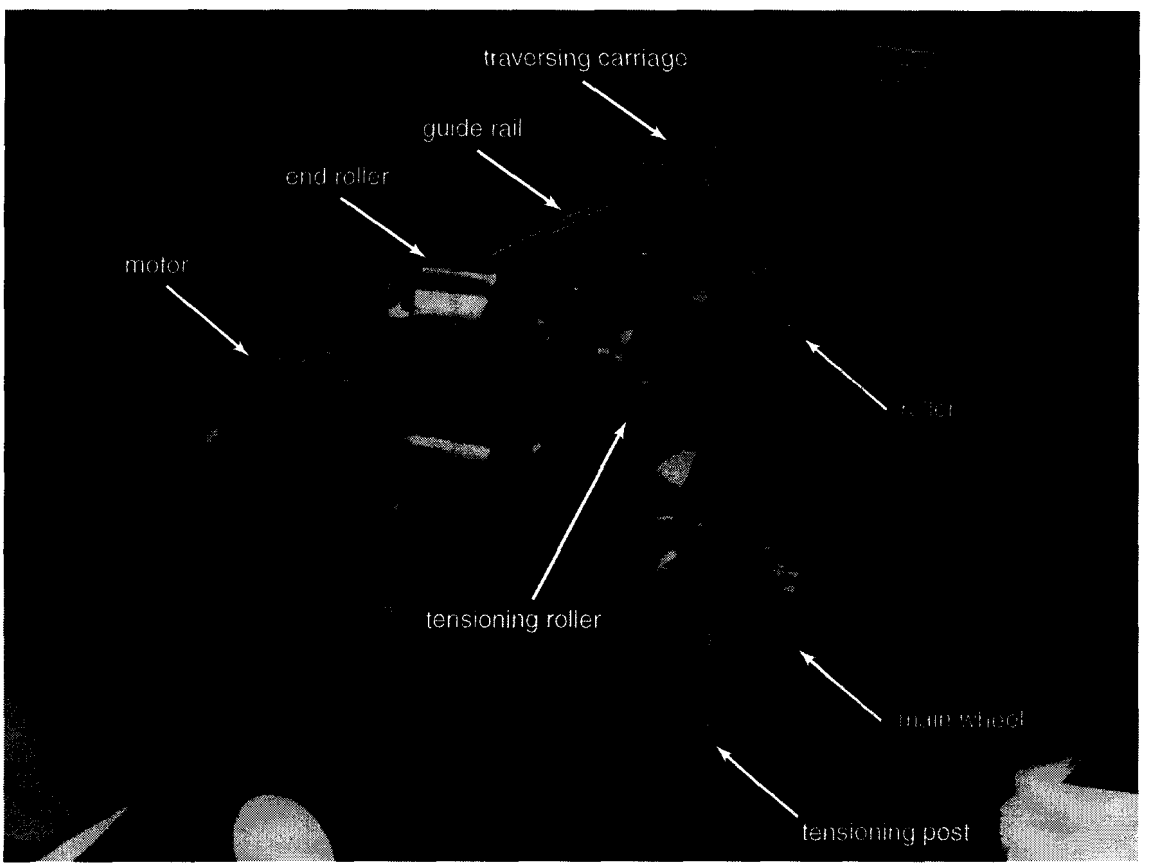

Figure **3.4:** Wind Tunnel Actuator.

Photograph of the Wind Tunnel Actuator (WTA). When a force balance and a vehicle model are mounted on the traversing carriage, the WTA allows a model to simulate platoon maneuvers.

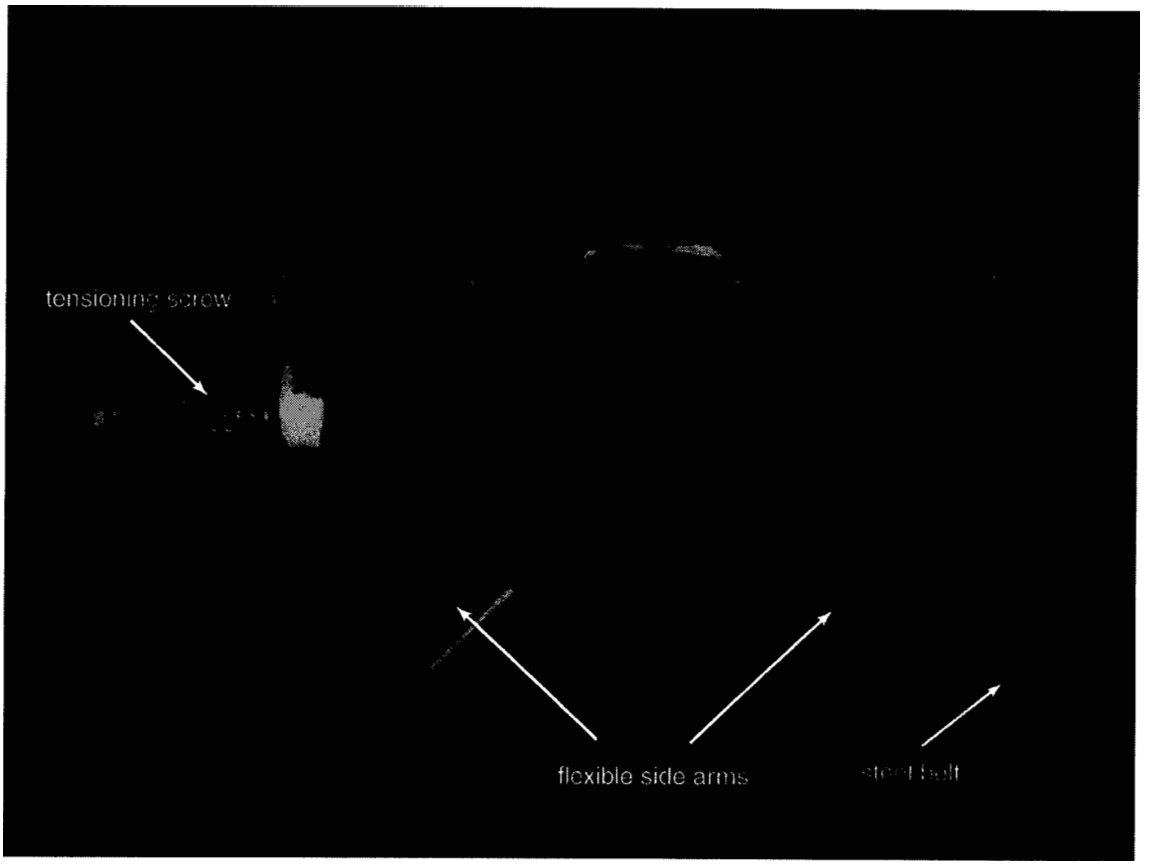

Figure **3.5:** Tensioning post.

Photograph of the tensioning post. **As** the main screw is tightened, the side arms remove slack in the steel belt.

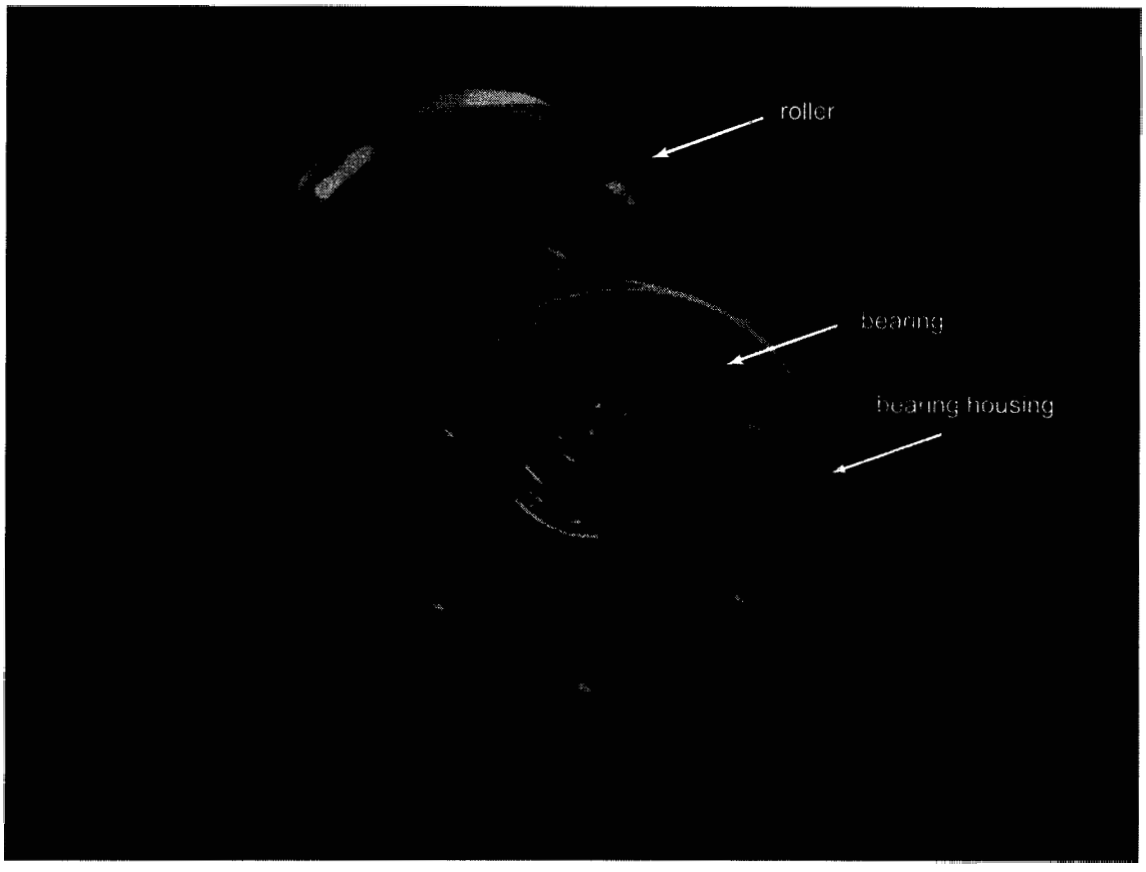

Figure **3.6:** Tensioning roller.

Photograph of the tensioning roller. The eccentric alignment of the bearing in the housing allows the **roller** to apply various amounts of tension to the steel band.

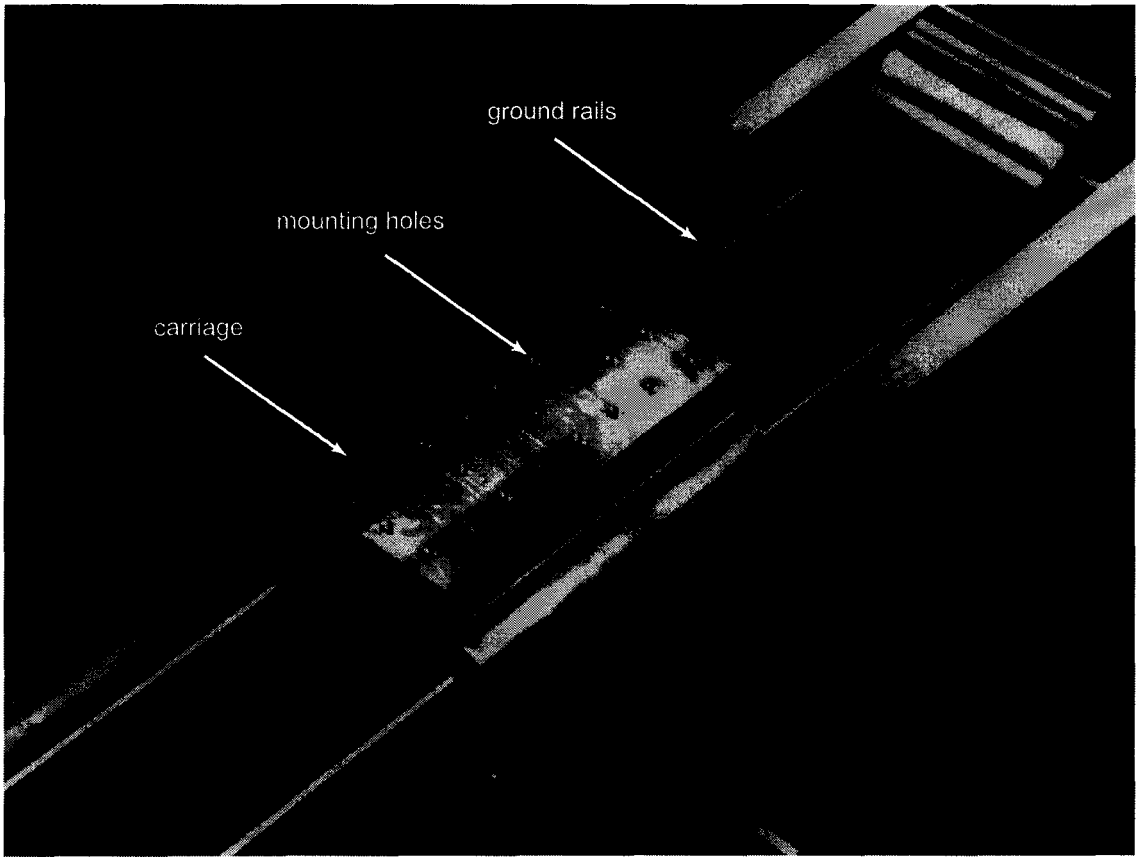

Figure **3.7:** Traversing carriage.

Photograph of the traversing carriage. The actuated model and balance are attached to the mounting holes of the carriage breadboard.

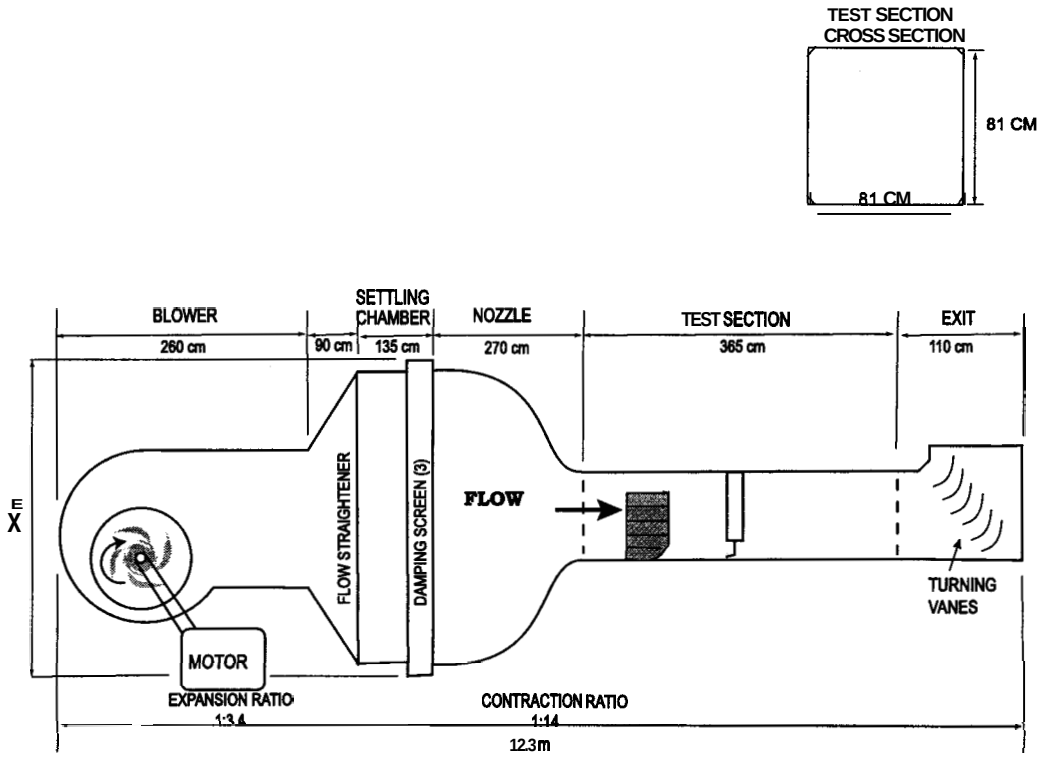

Figure **3.8:** Wind tunnel schematic.

The major components of the low-turbulence wind tunnel are shown. The test section measures **3.65** m x 81 cm x 81 cm.

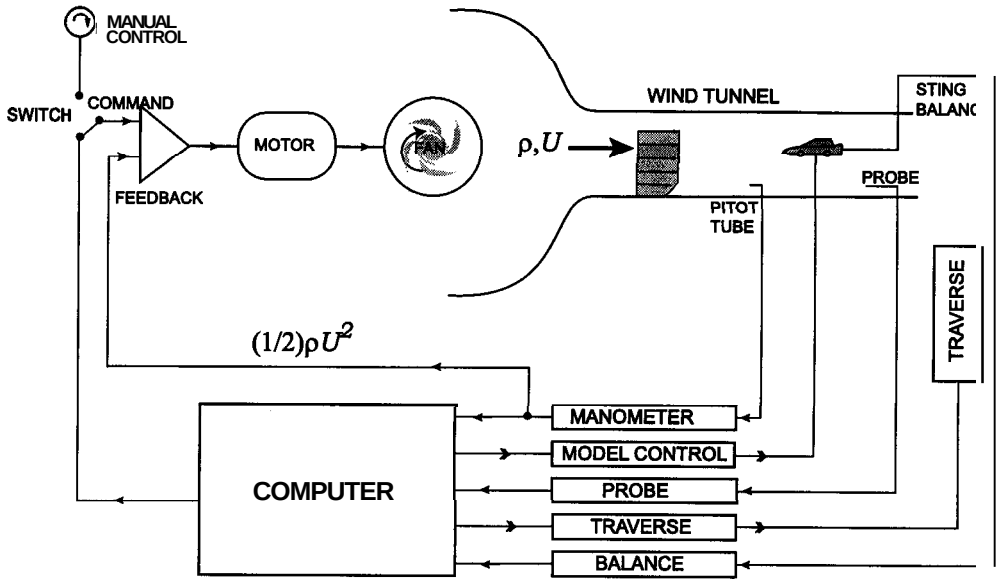

Figure **3.9:** Wind tunnel instrumentation.
The tunnel velocity is maintained by a computer through a pressure feedback circuit.

Chapter 4

Experimental Procedure

This chapter describes the procedures used in the following preliminary measurements. The force balances which will measure the aerodynamic forces and moments on the vehicles are calibrated. To isolate the aerodynamic forces on the mobile model, the inertial force and, thus, the acceleration of the mobile model are determined. Also, the ground plane boundary layer is characterized. In addition, procedures and parameters used in measuring the transient aerodynamics on the vehicle models are described.

4.1 Calibration of the Balances

The balances are calibrated through a careful loading procedure using a calibration frame. Known loads are applied in the longitudinal and lateral directions on each of the force balances as shown in Figure 4.1. The masses are yoked to the balance arms using only dowel pins, thus, avoiding additional torsion on the balance, and hung over precision bearings to minimize friction. The voltage outputs of the three circuits on a balance are measured simultaneously as the loads are applied. The calibration curves for each of the four balances used in the experiments are shown in Figures 4.2 - 4.5. In these figures, frames

(a)-(c), frames (d)-(f), and frames (g)-(i) show the balance outputs when a side force, drag force, and moment, respectively, is applied to the balance arms. As can be seen from the curves, the linearity of the circuits, for the forces and moments they are intended to measure, is better than 0.1% beyond the range of the expected force measurements. Comparing the outputs when a particular force or moment is applied, the mechanical cross-talk between the measured forces and moments ranges from 1%- 10%, depending upon the particular balance and circuit.

4.2 Encoder, Resolver, and Accelerometer

As a model is accelerated laterally with respect to the platoon, its force balance will measure a large lateral force, which includes the inertial force of the model along with the aerodynamic force experienced by the model. Therefore, to extract the aerodynamic force from the measured signal, the force due to the inertia of the model must be determined to a high degree of precision and accuracy and then subtracted from the signal. In determining the acceleration of the scale model, three separate measurement devices are used, a brief description of which is provided here. A more detailed explanation can be found in Snyder [25]. An optical encoder (Renco RM21), attached to the back of the motor driving the WTA, provides discrete position information. The encoder has a resolution of 2048 counts, and the output signal is sampled at a rate of 72.8 kHz by the data acquisition system. The encoder produces a pulse train, as shown in Figure 4.6, where each transition from a high voltage to a low voltage (or low to high) indicates an incremental change in the position of the rotor of the motor. The acceleration profile of the model is obtained by taking the derivative of the position information twice. The motor resolver, which provides positional feedback to the motor controller, produces an output similar to the encoder. The resolver

has a resolution of 1024 counts and is also sampled at a rate of 72.8 kHz.

Since both the encoder and resolver only directly provide position information of the motor, an accelerometer is attached to the traversing carriage to obtain a direct measure of the acceleration. The accelerometer (Silicon Designs 2210) is an analog, capacitive module with a range of ± 25 G. The accelerometer is calibrated over its entire range by securing it at a fixed radius to a rotary table and applying several centripetal accelerations. The rotary table is rotated at several angular velocities by a microstepper motor controlled through a personal computer. Using the relation for centripetal acceleration a_c,

$$a_c = \Omega^2 r \tag{4.1}$$

where Ω is the angular velocity and r is the radius, the accelerometer is calibrated for several accelerations. As shown in the calibration curve of Figure 4.7, the accelerometer is linear up to ± 90% of full-scale, as stated in its specifications.

4.3 Evaluation of the Boundary Layer

For full scale vehicles traveling on the road, no relative motion occurs between the air and the ground. In a wind tunnel, however, air flows over the ground plane, generating a boundary layer due to viscous effects. To simulate the motion of a vehicle in a wind tunnel, this boundary layer should be removed. The best solution is to use a moving ground plane. Since this is not feasible in the experiments, due to complexity and cost, an acceptable alternative is to remove part of the boundary layer with a suitable suction mechanism. As shown in Figure 4.8, suction is applied to a 1.2 mm x 81 cm slot located at the test section entrance to remove part of the boundary layer.

To determine the characteristics of the boundary layer, velocity profiles are measured at several points in the streamwise and cross-stream directions as shown in Figure 4.8 with

and without suction. The profiles are taken with a flattened total head pitot tube traversed by a computer controlled mechanism. Examples of these velocity profiles are shown in Figure **4.9.** The measured velocity profiles at several streamwise locations and one cross-stream point are shown. The solid lines represent the measurements when suction is applied, while the dotted lines represent measurements without suction of the boundary layer. The left column [frames (a)-(e)] shows the boundary layer without a platoon of vehicle models in the test section, and the right column [frames(f)-(j)] shows the boundary layer with the models present. Comparing the two columns, the presence of the models clearly disturbs the formation of the boundary layer, as shown by the less developed velocity profiles in the right column. The data points are logarithmically spaced across the boundary layer. When plotted on a semi-logarithmic scale (not shown here), the boundary layer exhibits the characteristics of zero-pressure gradient turbulent boundary layers. The velocity profiles show that suction removes the low speed air near the ground plane, resulting in fuller velocity profiles closer to the ground plane, and thus, a thinner boundary layer.

Three measures of the boundary layer thickness are shown as vertical lines in Figure **4.9:** the **95%** boundary layer thickness δ_{95}, defined as $u = 0.95U$, the displacement thickness S*, defined as

$$\delta^* = \int_0^\infty \left(1 - \frac{u}{U}\right) \mathrm{dy} \tag{4.2}$$

and the momentum thickness θ, defined as

$$\theta = \int_0^\infty \frac{u}{U}\left(1 - \frac{u}{U}\right) dy \tag{4.3}$$

Figure **4.9** shows that the boundary layer thickness is reduced in all cases when suction is applied. However, the presence of the models increases the boundary layer thickness. This adverse effect is more pronounced downstream, where the displacement effects and vortex

shedding from the models are thought to alter the naturally developing boundary layer flow over the tunnel floor.

Figure 4.10 shows the boundary layer growth with downstream distance. Again, the boundary layer thicknesses δ_{95}, δ^*, and θ are shown with and without suction. The symmetry between the measurements taken to the left [frames (a), (c), (e)] of the tunnel centerline and those taken to the right [frames (b), (d), (f)] indicates a fairly uniform flow across the tunnel. Growth of the boundary layer thickness is approximately linear, which is characteristic of turbulent boundary layers with no pressure gradient. Suction reduces the boundary layer thickness in all cases. The displacement thickness δ^* measures about 1 mm near the test section entrance and 4 mm at 108 cm downstream when suction is applied, which is small compared to the model ground clearance of 13 mm (Table 3.1). Thus, the wind tunnel tests are deemed suitable for simulating the operation of a platoon on the highway.

4.4 Description of Experiments

In the experiments, a platoon of four vehicle models is aligned in the center of the wind tunnel test section as shown in Figure 4.11. The experiments are designed around the expected operating conditions of a full scale platoon. The design conditions are defined as follows: inter-vehicle spacing of $s_d = 0.41$ (anticipated vehicle separation in a full scale platoon) and lane change duration of $t_d = 0.5$ seconds (equivalent to a 5 second lane change by a full scale vehicle). Figure 4.12 shows the platoon configurations used in the experiments. Three inter-vehicle spacings are tested: 0.21, 0.41, 1. In addition, any one of the four models can be arranged as the mobile car. For each location of the mobile vehicle and each vehicle separation, the mobile car is moved at six different accelerations (equivalent

to different durations of time required for a lane change). Further details are provided in Section **5.3.** These three variables result in a minimum of **72** platoon configurations. The time required for the slowest move (lowest acceleration) is much longer than the time required for the flow to recover and become steady. Thus, these measurements are labeled *static (t,)* and represent steady-state measurements. Three experimental runs are made for each configuration of the platoon. For each experimental run, the mobile car is moved out of the platoon $2.5w$, paused, and returned back into the platoon. For example, in the design case, the mobile car moves out of the platoon at the design acceleration, completing the move in **0.5** seconds, which is equivalent to a 5-second lane change maneuver by a full scale vehicle. The mobile car pauses for **0.3** seconds and then returns into the platoon at the design acceleration, completing the return in **0.5** seconds. Thus, the entire run takes **1.3** seconds. During these motion profiles, the drag, side force, and yawing moment of each car is simultaneously sampled at a rate of **5.2** kHz. The accelerometer mounted underneath the mobile car and the tunnel velocity are also sampled at a rate of **5.2** kHz. The position of the mobile car is determined by sampling the encoder and resolver signals at 72.8 kHz. Typically, three experimental runs are performed for each setting. All measurements are made at $Re = 3.4 \cdot 10^5$, where the Reynolds number is defined by Equation **2.9** and the characteristic length is the model length.

Measurements are also made on a single vehicle model for comparison with the measurements for vehicles in a platoon configuration. In addition, measurements are made at the design separation s_d using a platoon of rectangular boxes, simpler shapes than the cars, for comparison. These boxes have dimensions of **25.4** cm **(10** in.) x **10.2** cm **(4**in.) x **7.6** cm **(3** in.) and approximate the volume of the vehicle models. Measurements on a single rectangular box are also made for comparison.

4.5 Figures

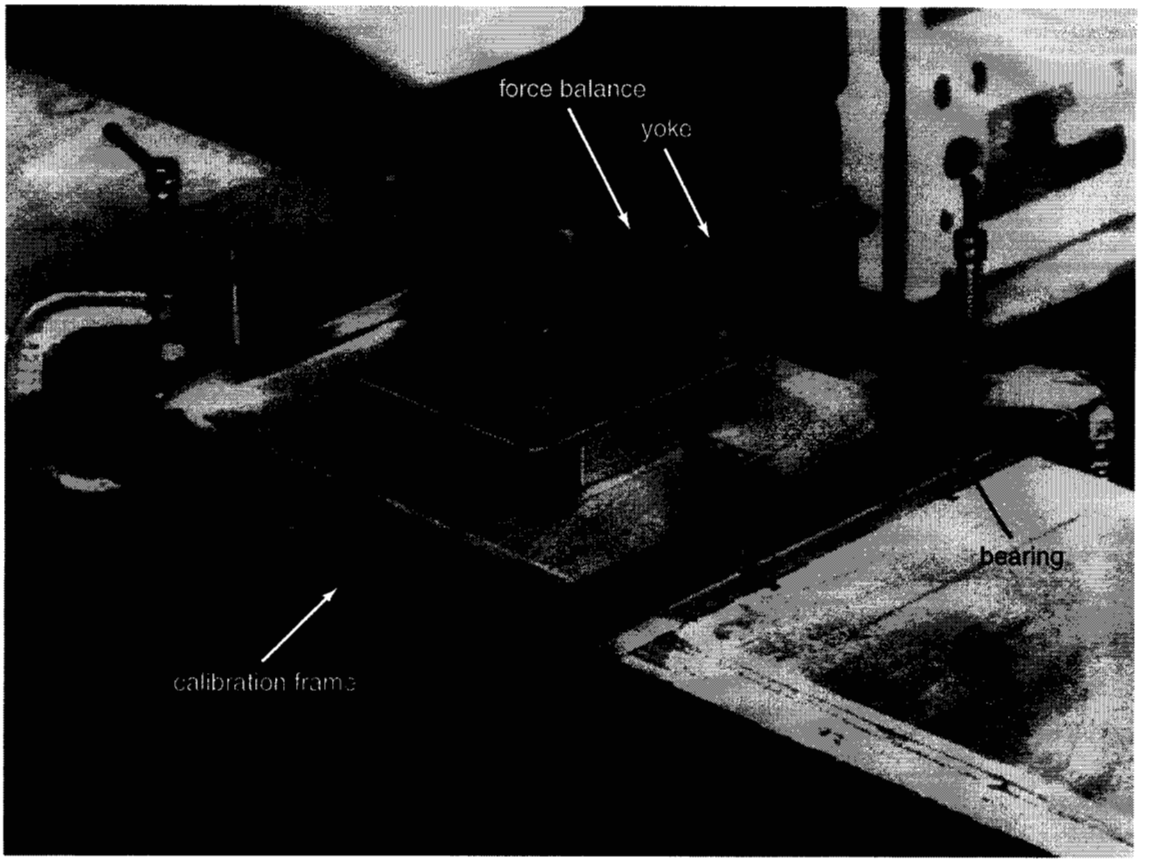

Figure 4.1: Force balance calibration frame.
Photograph of the calibration frame. A balance is calibrated by yoking masses to the balance arms with dowel pins and hanging the masses over precision bearings.

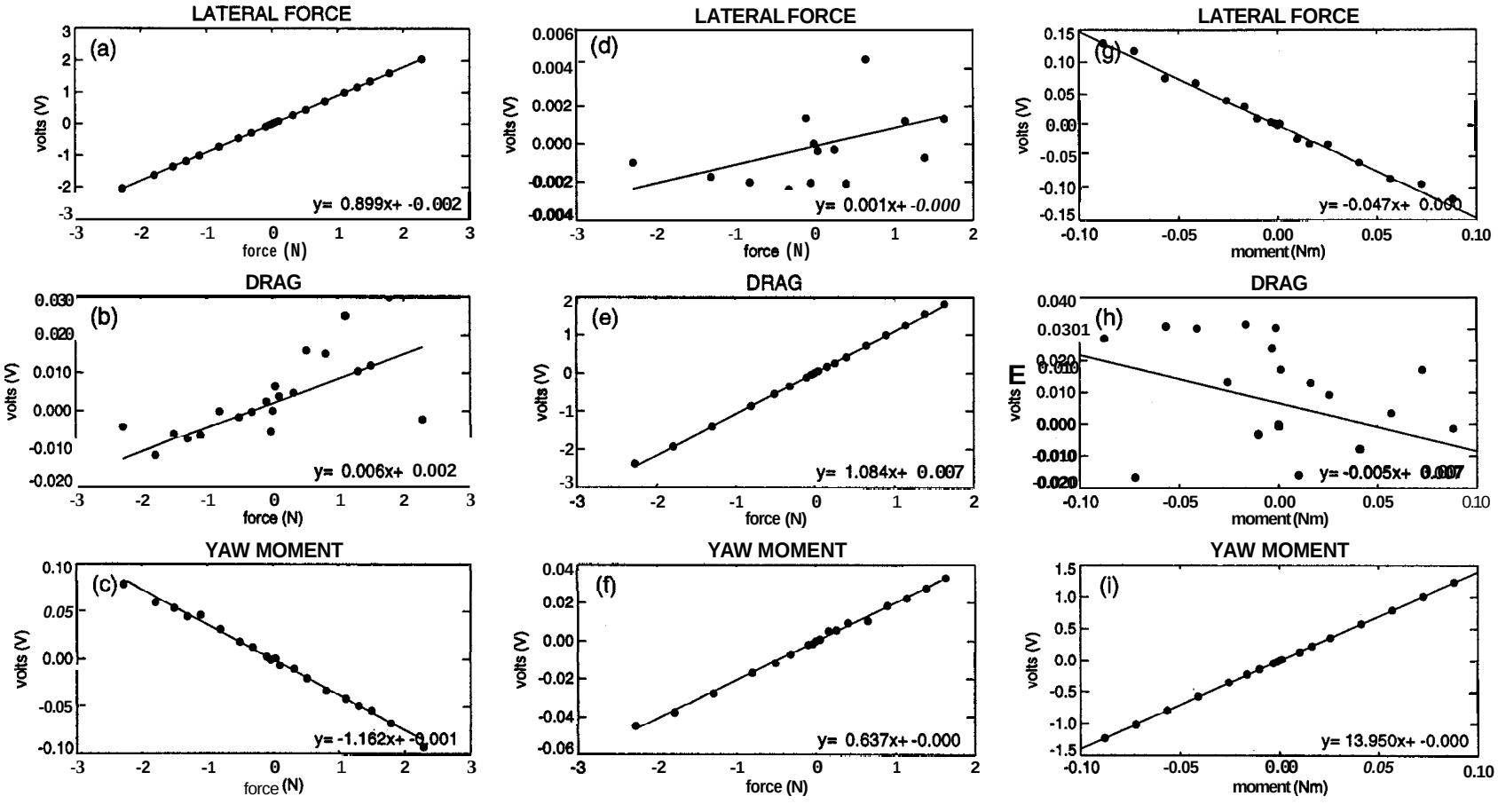

Figure **4.2:** Calibration of Balance **#1.**

Strain gage calibration curves for Balance **#1.** Frames (a)-(c) show the calibration and cross-talk when a lateral force is applied. Frames (d)-(f) show the outputs when a drag force is applied. Frames (g)-(i) show the outputs when a yawing moment **is** applied.

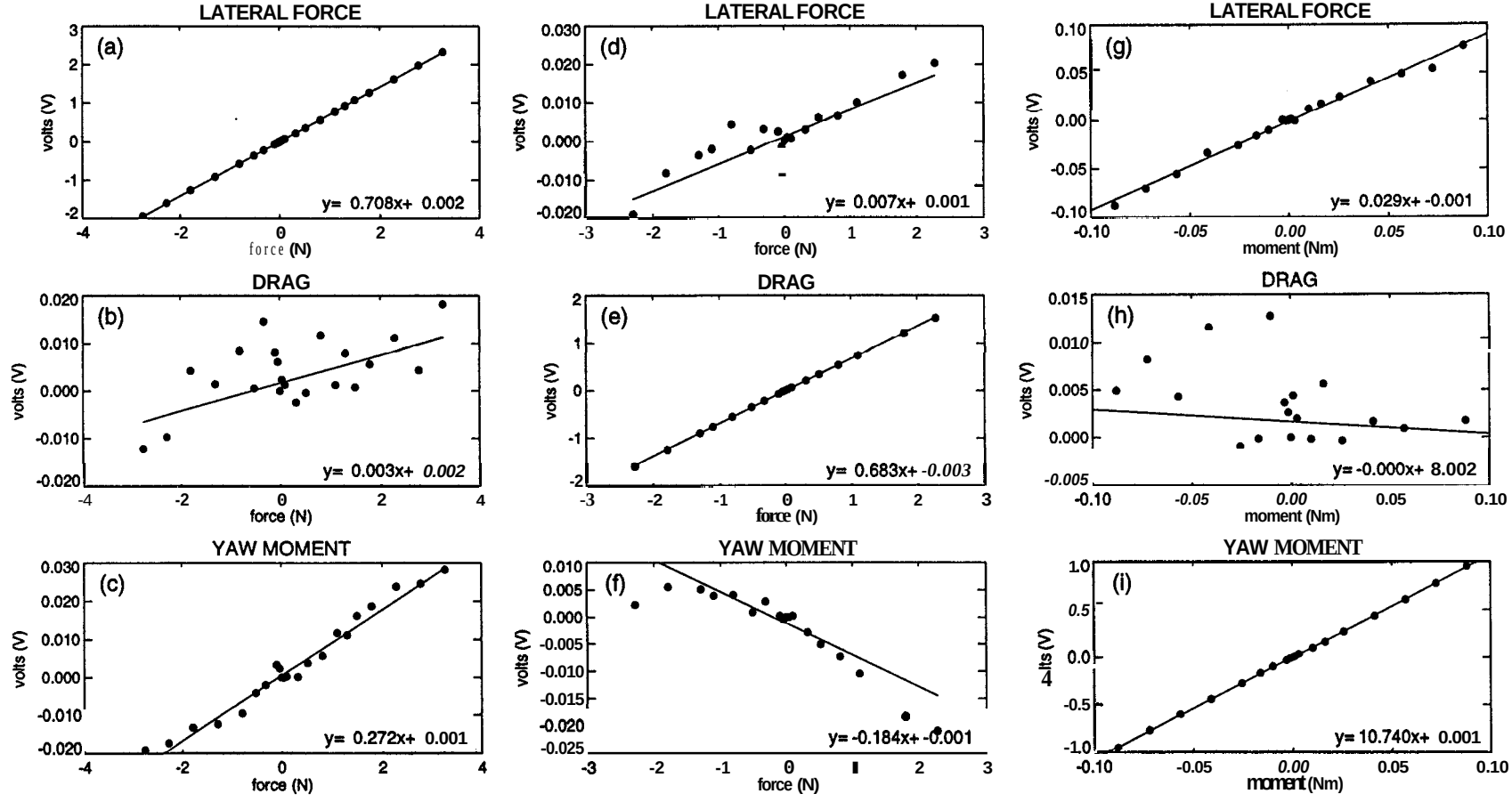

Figure 4.3: Calibration of Balance #2.

Strain gage calibration curves for Balance #2. Frames (a)-(c) show the calibration and cross-talk when a lateral force is applied. Frames (d)-(f) show the outputs when a drag force is applied. Frames (g)-(i) show the outputs when a yawing moment is applied.

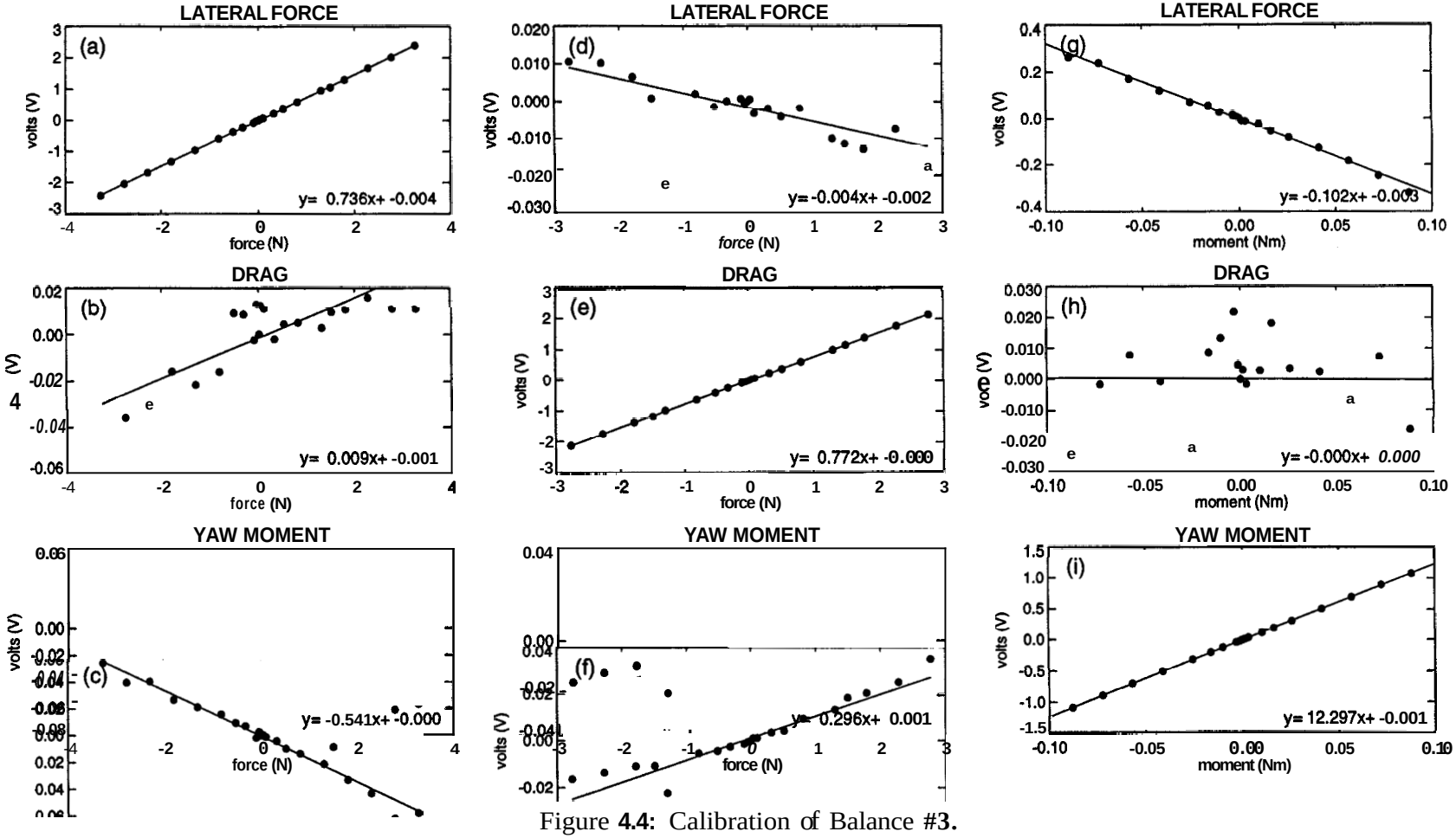

Figure **4.4**: Calibration of Balance #**3.**

Strain gage calibration curves for Balance #**3.** Frames (a)-(c) show the calibration and cross-talk when a lateral force is applied. Frames (d)-(f) show the outputs when a drag force is applied. Frames (g)-(i) show the outputs when a yawing moment is applied.

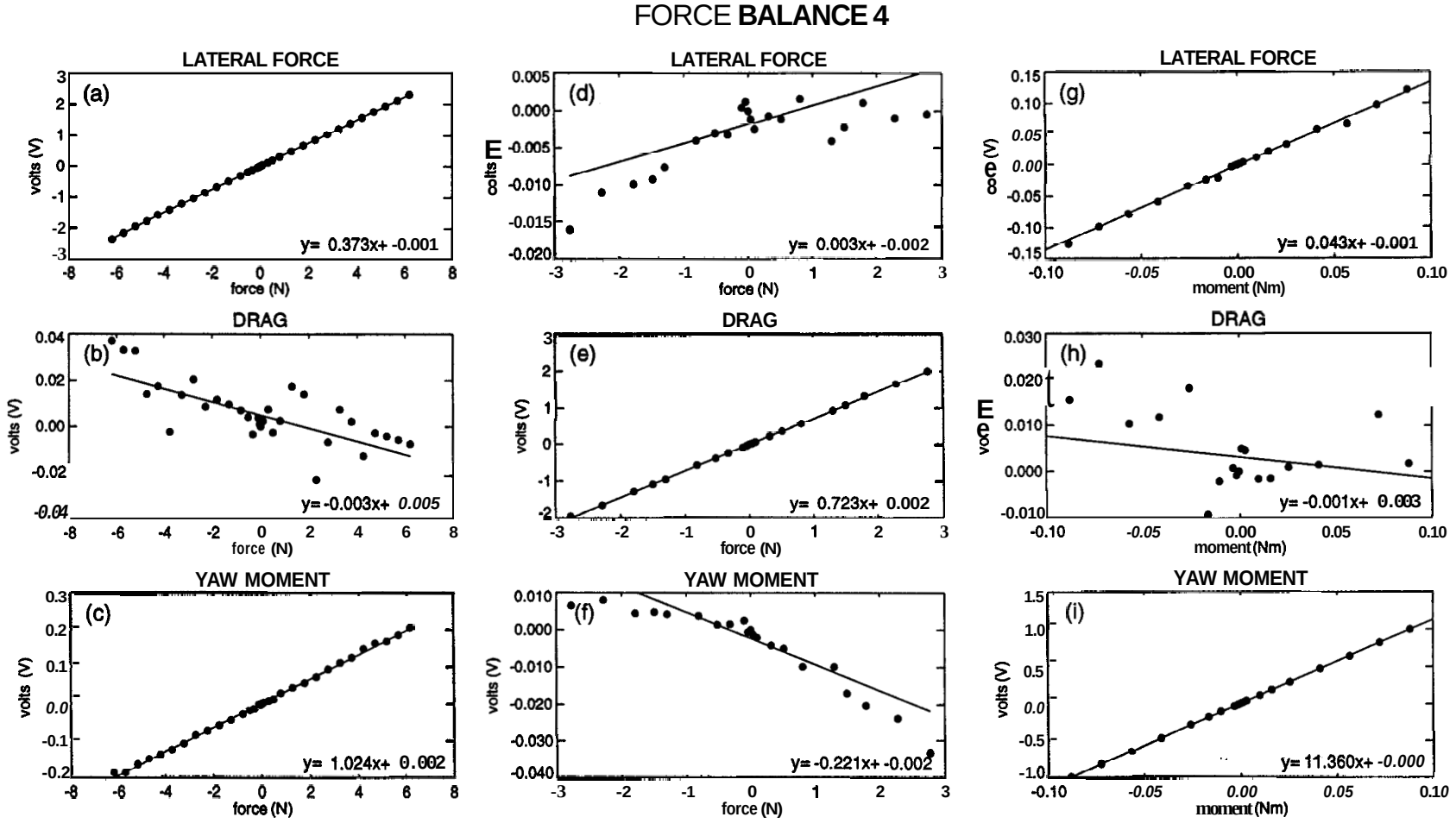

Figure 4.5: Calibration of Balance #4.

Strain gage calibration curves for Balance #4. Frames (a)-(c) show the calibration and cross-talk when a lateral force is applied. Frames (d)-(f) show the outputs when a drag force is applied. Frames (g)-(i) show the outputs when a yawing moment is applied.

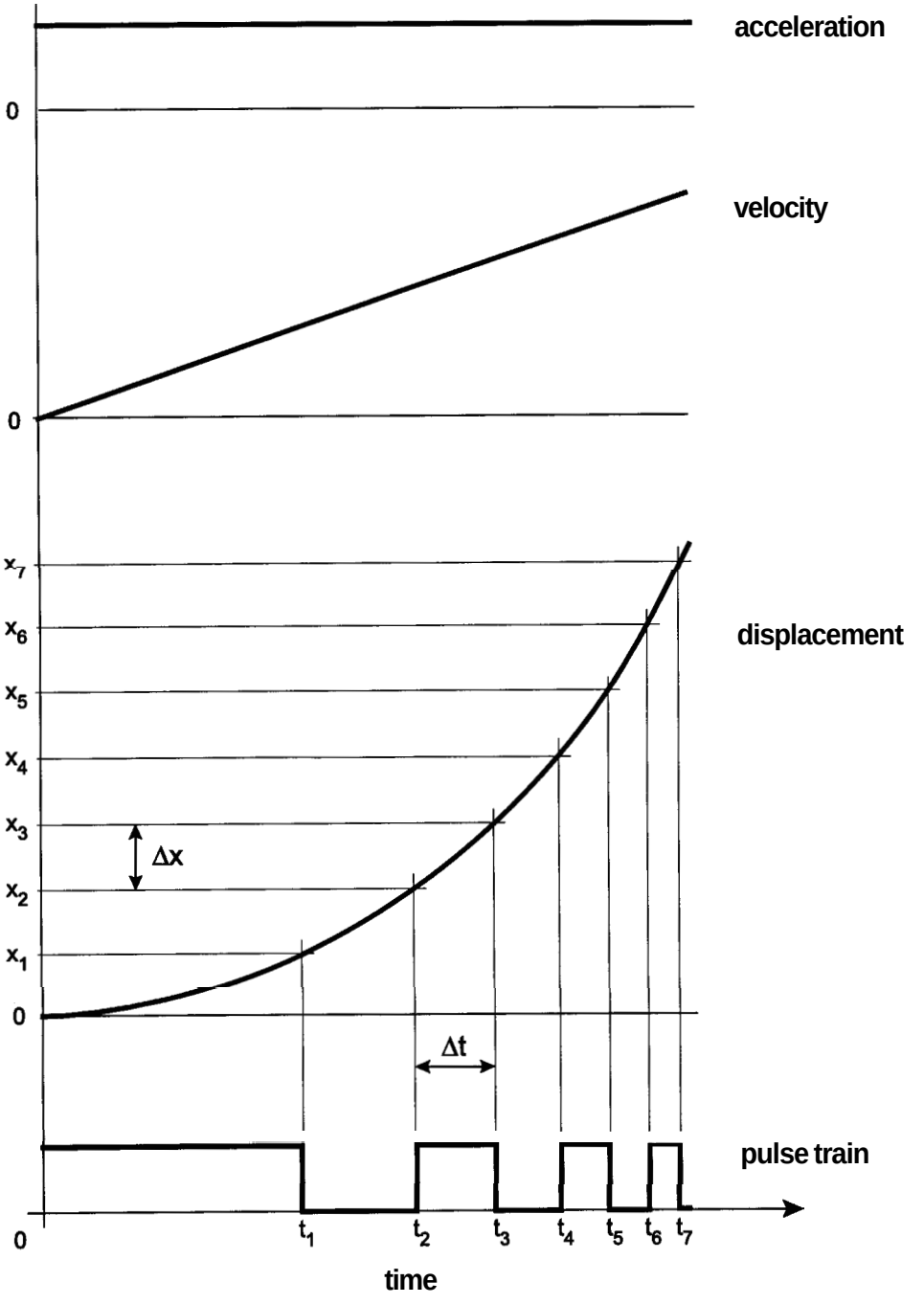

Figure **4.6:** Encoder output.

The optical encoder produces a pulse train representing the rotation of the encoder. More pulses are produced during a faster rotation, while fewer are generated during a slow rotation.

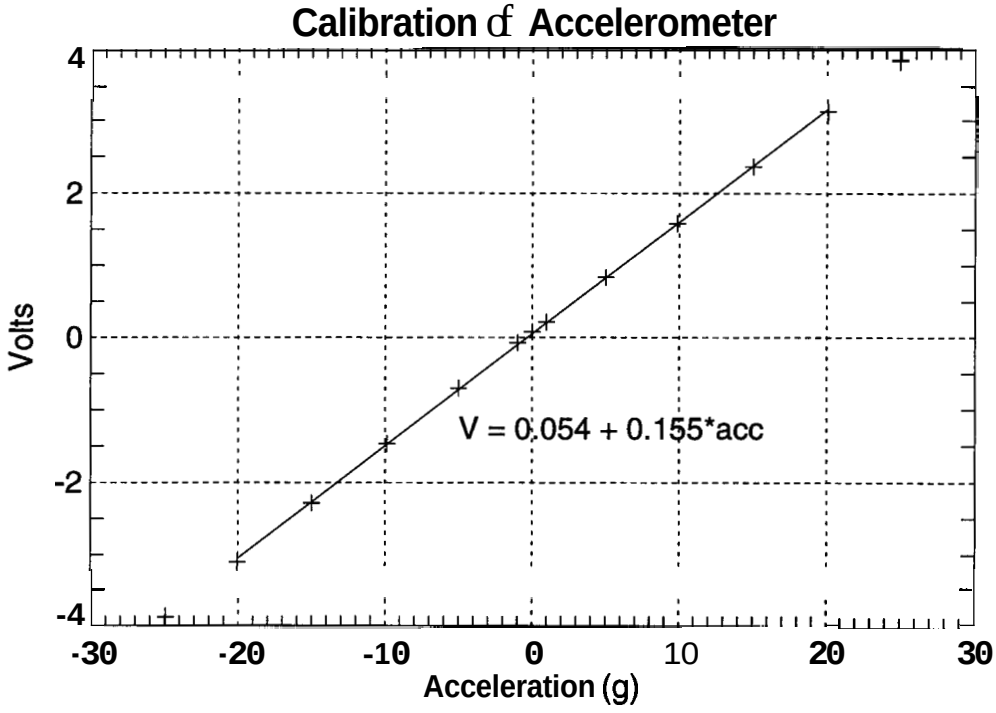

Figure 4.7: Accelerometer calibration.

Calibration curve for the accelerometer. The accelerometer is linear up to ± 90% of full-scale.

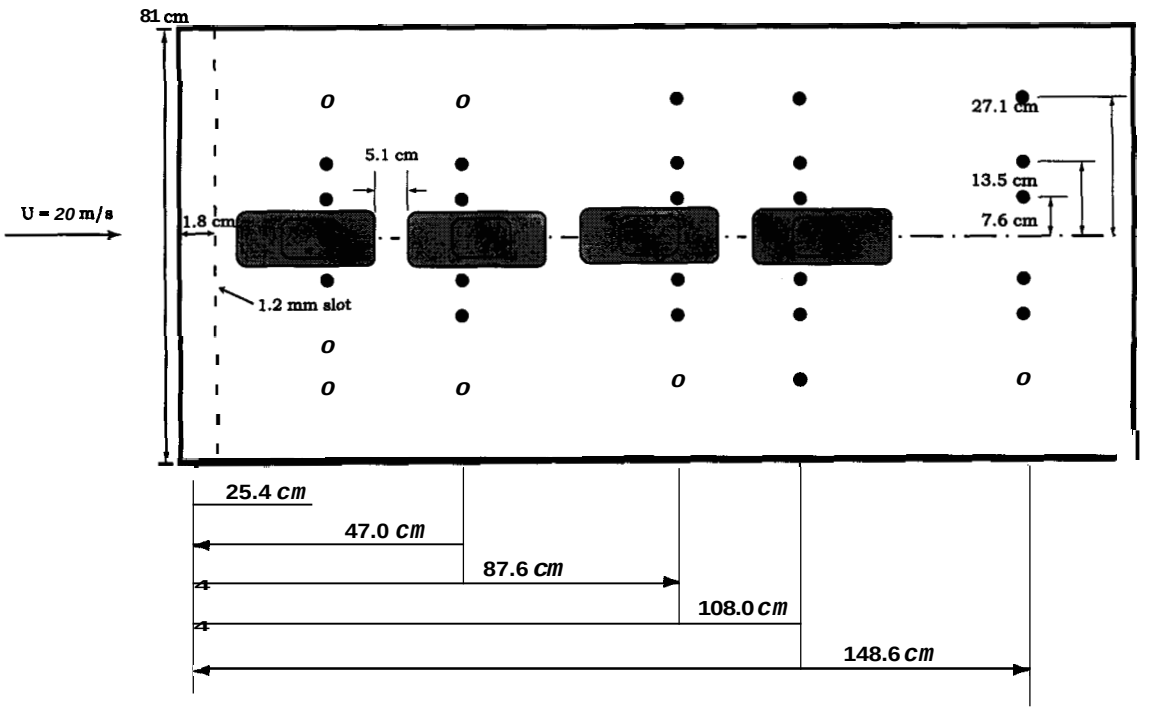

Figure 4.8: Boundary layer survey.

Boundary layer velocity profiles are measured at the locations marked by dots with and without the presence of the vehicle models.

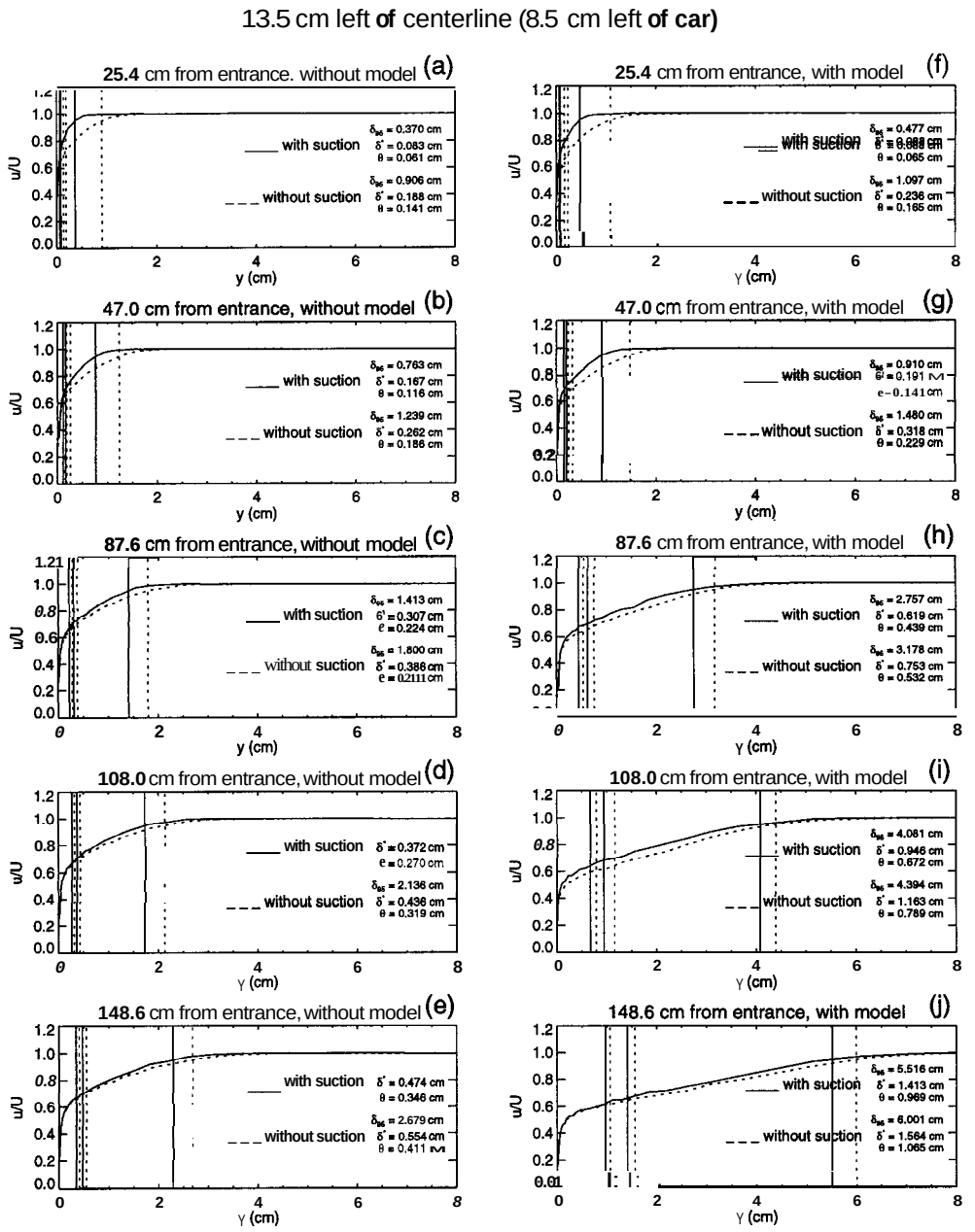

Figure **4.9:** Boundary layer velocity profiles.

Boundary layer velocity profiles at several downstream locations and one cross-stream location with and without suction. Frames (a)-(e) show profiles without the presence of the models, while frames (f)-(j) show the effect of the models' presence.

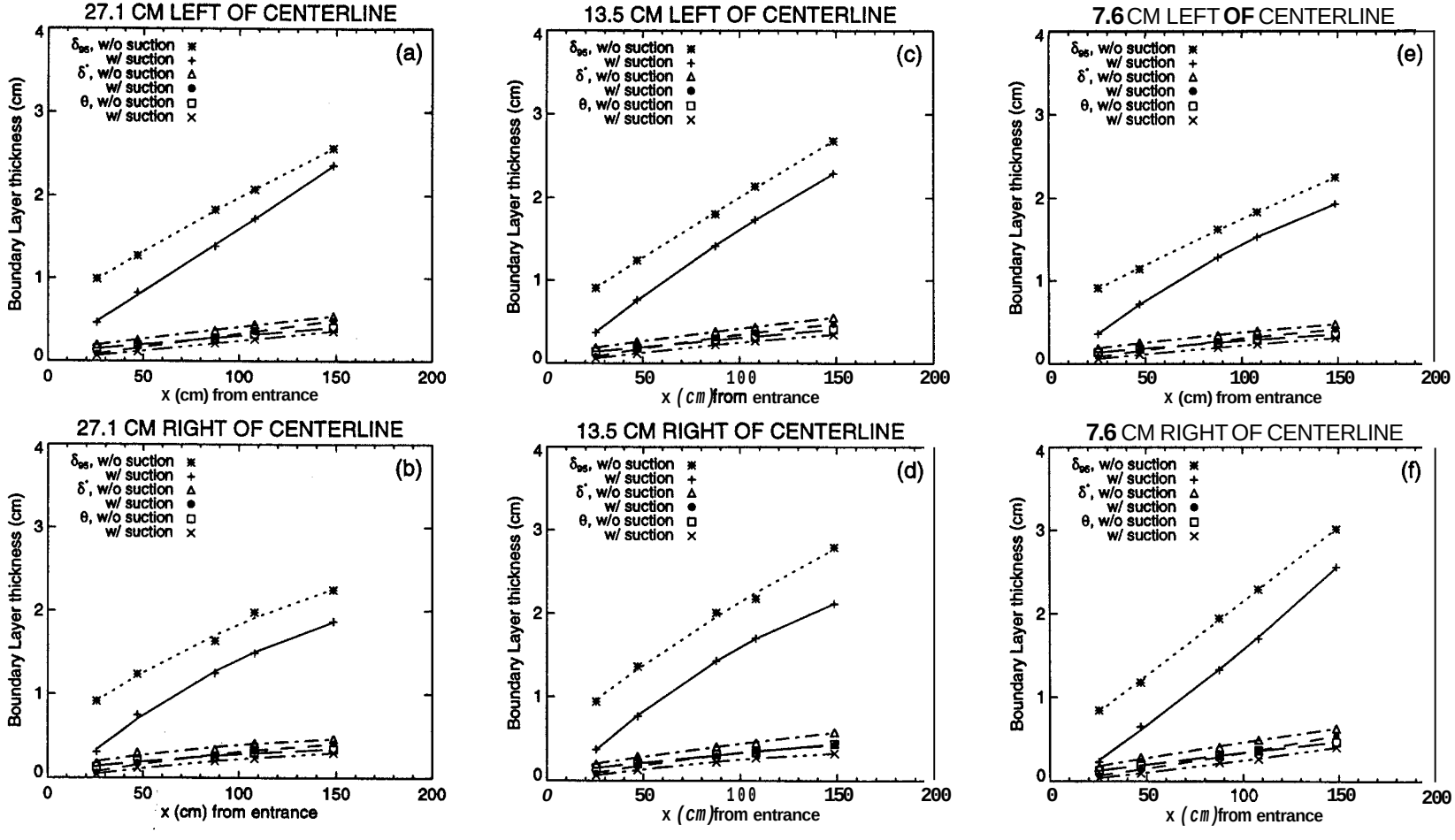

Figure **4.10:** Boundary layer growth.
The boundary layer growth with downstream distance is shown with and without suction. Suction reduces the boundary layer thickness in all cases.

Figure **4.11:** Four-car platoon.

Four scale vehicle models aligned in a platoon configuration in the wind tunnel test section. The pitot tube used in the boundary layer survey is also visible.

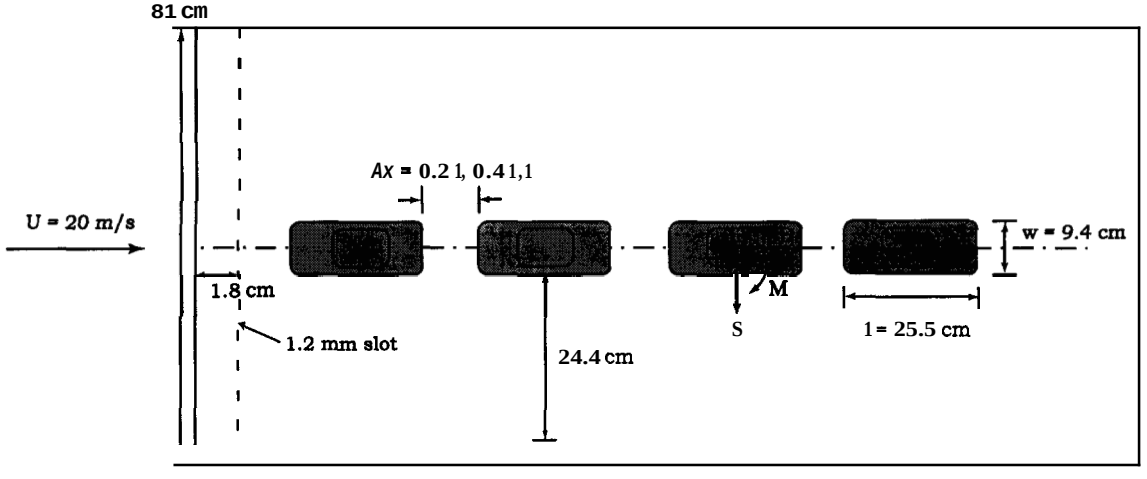

Figure 4.12: Experiment parameters.

The parameters for the measurements of the transient aerodynamic forces and moments on a four-car platoon are shown. Any one of the four cars is moved in and out of the platoon at six different accelerations. In addition, three vehicle spacings are used.

Chapter 5

Data Analysis

This section describes the process of filtering the measured signals to obtain force and moment measurements. The derivation of acceleration information from the position information of the encoder and resolver is also described. In addition, the large amount of data requires a systematic identification scheme, and the identification parameters are described here. All data processing is performed with Research Systems Incorporated Interactive Data Language (IDL).

5.1 Signal Filtering

To minimize electrical noise induced by EM transmission from the WTA motor and mechanical noise from vibrations of the building on the measured signal lines, standard noise reduction techniques are used. All parts of the WTA which might act as electrical capacitors are grounded. In addition, the signal lines and amplifier boxes are shielded, and the signals are passed through low-pass band filters. Using these techniques, the noise is reduced from about **30%** to about **3%** of the measured signal, an order of magnitude in reduction. An example of the signals obtained with these methods is shown in Figure 5.1.

The three outputs, drag [frames (a)-(d)], side force [frames (e)-(h)], and yawing moment [frames (i)-(l)], from the balances of the four vehicle models in the test section are shown as voltages versus time. In this example, the mobile model is the first car in the platoon and moves laterally out of the platoon, and after a brief pause, returns into the platoon. The mobile car moves at the design acceleration (equivalent to a time scale of t_d) and the vehicle separation is 0.41. The signals still appear noisy and are difficult to interpret.

Applying a standard Fast-Fourier Transform (FFT) algorithm [26] to transform the signals $h(t)$ from the time domain to the frequency domain as

$$H(f) = \mathcal{F}[h(t)] \equiv \int_{-\infty}^{\infty} h(t) e^{2\pi i f t} dt \tag{5.1}$$

the actual measurements, containing the lower frequency components, can be separated from the noise, consisting of the higher frequency components of the spectrum. Frames (b), (h), (n) of Figures 5.2 - 5.5 show the Fourier transforms of the signals in Figure 5.1, which are reproduced in frames (a), (g), (m). Since the spectra are symmetric, only the positive frequencies are shown here. In addition, the plots are on a semi-log scale to improve visual resolution of the peaks. The drag, side force, and yawing moment for each car are plotted in the same figure. Multiplying the Fourier transformed signals by a filter kernel which is narrower than the lowest frequency of the noise preserves the signal of the actual measurements while removing the noise. A variety of filters are available from square to various parabolas. A Gaussian window of the form

$$G(f) = e^{-\frac{f^2}{\sigma^2}} \tag{5.2}$$

where f is the frequency and σ is the window width, is selected here as the best compromise between avoiding false ringing in the signal (Gibbs phenomenon [26]) and preservation of the original signal. The size of the Gaussian window can be chosen from a systematic

examination of the effect of filter width on the signal. Several Gaussian windows of different widths are shown with the Fourier transforms in frames (b), (h), (n). The Gaussian windows appear parabolic due to the semi-log plot. The signals are filtered by taking the inverse Fourier transform of the product of the frequency spectrum of the measured signal and the Gaussian window as

$$< H >= \mathcal{F}^{-1}[H(f) \cdot G(f)] \equiv \int_{-\infty}^{\infty} H(f) \cdot G(f) e^{-2\pi i f t} df \tag{5.3}$$

The filtered signals obtained with Gaussian windows of various widths are shown in frames (c)-(f), (i)-(l), (o)-(r). The width of the Gaussian window should be only slightly narrower than the lowest mode of the noise to avoid attenuating the original measurement as in frames (c), (i), (o). To determine the lowest mode of the noise, the resonant frequency of the model and balance system is obtained by applying a sharp tap to the system. The resulting frequency spectra are shown in Figure 5.6. From Figures 5.2 - 5.5 and Figure 5.6, a filter width of $\sigma = 8.0$ Hz is chosen for filtering of all the force and moment measurements. The resulting signals obtained with this Gaussian window function are summarized in Figure 5.7. These filtered signals contain the flow dynamics and are used for all of the following comparisons and discussions.

5.2 Position and Acceleration

The position profile of the model simulating a lane change is obtained from the encoder mounted on the rotor of the WTA motor and the resolver of the motor controller. As described in Section 4.2, the encoder produces a pulse train, where each pulse represents an incremental change in the position of the motor rotor. The motor resolver produces an output similar to the encoder; thus, the position profiles should be nearly identical, as shown in Figure 5.8(a), (b). As described in the previous section, in this example, the mobile model

is the first of four cars in a platoon and moves laterally $2.5w$ out of the platoon, and after a brief pause, returns into the platoon. The encoder and resolver produce more pulses when the motor rotates faster and fewer pulses during a slow rotation; therefore, the position data are unevenly spaced in time. The encoder and resolver data are linearly interpolated to correspond to the time points at which the forces are measured and then averaged. The average position appears in Figure 5.8(c).

The acceleration profile of the mobile model is obtained by taking the derivative of the position information twice in the Fourier domain as:

$$\frac{d^n h(t)}{dt^n} \Longleftrightarrow (2\pi i f)^n H(f) \tag{5.4}$$

where $H(f)$ is the Fourier transform of the function $h(t)$ as defined in Equation 5.1. However, differentiation is a noise-amplifying process, requiring filtering after each step to retain only the physical action and not the artifacts of the processing. **As** with the forces and moments, a filter kernel (Gaussian window) is applied in the frequency spectrum to separate the actual measurement from noise generated from the differentiation. The filtered velocity and acceleration profiles from the average position profile are shown in Figure 5.8(d), (e). The filtered output of the accelerometer mounted on the WTA carriage is shown in Figure 5.8(f) for comparison. The acceleration profile of the accelerometer resembles that derived from the average position profile of the encoder and resolver. However, a discrepancy exists between the magnitudes of the two profiles due to a switchover problem with the accelerometer. The accelerometer has difficulty switching between positive and negative accelerations quickly. **A** more sensitive or adjustable accelerometer is required. Since no definitive conclusions can be made with the acceleration information available, the acceleration of the mobile model and separation of its inertial force from its aerodynamic side force and yawing moment will not be discussed further here, but will be deferred to future experiments.

5.3 Organization of Data

Three main parameters are varied in the experiments and are designated by the indices **ijk.** The variables of the experiment are the location of the mobile car in the platoon [four locations, $i = 1$ (first car), **..., 4** (last car)], the separation distance between the models [three separations, $j = 1\ (0.2l)$, 2 $(0.4l)$, **3** (l)], and the acceleration profile of the moving car [six profiles, **k = l** (t_∞), **..., 6** $(0.5\,t_d)$]. In addition, measurements for each configuration are repeated three times, where each trial is specified by the index 1. All combinations of these variables result in a minimum of **216** experimental runs. Each run is uniquely specified as E_{ijkl} by the four indices representing these variables as shown in Tables 5.1 and **5.2.** Similarly, each experimental run with the platoon of boxes is designated by B_{ijkl} as shown in Table ***5.3.*** Since measurements are made for the box platoon with only one separation **0.41,** j is always 2 in the box designations.

After filtering the signals obtained from the balances by FFT, the forces are converted from voltages to Newtons and the moments from voltages to Newton-meters with the calibration curves shown in Figures **4.2 - 4.5.** Any initial offsets are removed by subtracting an initial reading taken with no flow in the test section from the measured signals. The forces are then scaled with the dynamic head of the flow and the frontal area of the scale model (or volume of the model in the case of moments) as described in Section 2.2. **All** further discussion of the results will be with respect to the nondimensional force and moment coefficients.

5.4 Tables & Figures

acceleration (time scale)	trial	maneuver position					
		1			2		
		separation			separation		
		1	2	3	1	2	3
t_∞	1	E_{1111}	E_{1211}	E1311	E2111	E2211	E2311
	2	E1112	E_{1212}	E1312	E2112	E2212	E2312
	3	E_{1113}	E_{1213}	E1313	E2113	E2213	E2313
$2t_d$	1	E_{1121}	E_{1221}	E1321	E2112	E_{2221}	E2321
	2	E1122	E1222	E1322	E2122	E2222	E2322
	3	E_{1123}	E_{1223}	E1323	E2123	E2223	E2323
$1.5t_d$	1	E_{1131}	E_{1231}	E1331	E2131	E2231	E2331
	2	E_{1132}	E_{1232}	E1332	E2132	E2232	E2332
	3	E_{1133}	E_{1233}	E1333	E2133	E_{2233}	E2333
t_d	1	E_{1141}	E_{1241}	E1341	E2141	E2241	E2341
	2	E_{1142}	E_{1242}	E1342	E2142	E2242	E2342
	3	E_{1143}	E_{1243}	E1343	E2143	E_{2243}	E_{2343}
$0.67t_d$	1	E_{1151}	E_{1251}	E1351	E2151	E_{2251}	E_{2351}
	2	E_{1152}	E_{1252}	E1352	E2152	E_{2252}	E_{2352}
	3	E_{1153}	E_{1253}	E1353	E2153	E_{2253}	E_{2353}
$0.5t_d$	1	E_{1161}	E_{1261}	E1361	E2161	E_{2261}	E_{2361}
	2	E1162	E1262	E1362	E_{2162}	E_{2262}	E_{2362}
	3	E1163	E1263	E1363	E2163	E_{2263}	E_{2363}

Table 5.1: Test Matrix (a) - Cars.

acceleration (time scale)	trial	maneuver position					
		3			4		
		separation			separation		
		1	2	3	1	2	3
t_∞	1	E3111	E3211	E3311	E4111	E4211	E4311
	2	E3112	E3212	E3312	E4112	E4212	E4312
	3	E3113	E3213	E3313	E4113	E4213	E4313
$2t_d$	1	E3121	E3221	E3321	E4112	E4221	E4321
	2	E3122	E3222	E3322	E4122	E4222	E4322
	3	E3123	E3223	E3323	E4123	E4223	E4323
$1.5t_d$	1	E3131	E3231	E3331	E4131	E4231	E4331
	2	E3132	E3232	E3332	E4132	E4232	E4332
	3	E3133	E3233	E3333	E4133	E4233	E4333
t_d	1	E3141	E3241	E3341	E4141	E4241	E4341
	2	E3142	E3242	E3342	E4142	E4242	E4342
	3	E3143	E3243	E3343	E4143	E4243	E_{4343}
$0.67t_d$	1	E3151	E3251	E3351	E4151	E4251	E_{4351}
	2	E3152	E_{3252}	E3352	E4152	E4252	E4352
	3	E3153	E3253	E3353	E4153	E4253	E4353
$0.5t_d$	1	E3161	E3261	E3361	E4161	E4261	E4361
	2	E3162	E3262	E3362	E4162	E4262	E4362
	3	E3163	E3263	E3363	E4163	E4263	E4363

Table *5.2:* Test Matrix (b) - Cars.

acceleration (time scale)	trial	maneuver position 1	2	3	4
t_∞	1	B_{1211}	B_{2211}	B_{3211}	B_{4211}
	2	B_{1212}	B_{2212}	B_{3212}	B_{4212}
	3	B_{1213}	B_{2213}	B_{3213}	B_{4213}
$2t_d$	1	B_{1221}	B_{2221}	B_{3221}	B_{4212}
	2	B_{1222}	B_{2222}	B_{3222}	B_{4222}
	3	B_{1223}	B_{2223}	B_{3223}	B_{4223}
$1.5t_d$	1	B_{1231}	B_{2231}	B_{3231}	B_{4231}
	2	B_{1232}	B_{2232}	B_{3232}	B_{4232}
	3	B_{1233}	B_{2233}	B_{3233}	B_{4233}
t_d	1	B_{1241}	B_{2241}	B_{3241}	B_{4241}
	2	B_{1242}	B_{2242}	B_{3242}	B_{4242}
	3	B_{1243}	B_{2243}	B_{3243}	B_{4243}
$0.67t_d$	1	B_{1251}	B_{2251}	B_{3251}	B_{4251}
	2	B_{1252}	B_{2252}	B_{3252}	B_{4252}
	3	B_{1253}	B_{2253}	B_{3253}	B_{4253}
$0.5t_d$	1	B_{1261}	B_{2261}	B_{3261}	B_{4261}
	2	B_{1262}	B_{2262}	B_{3262}	B_{4262}
	3	B_{1263}	B_{2263}	B_{3263}	B_{4263}

Table *5.3:* Test Matrix - Boxes.

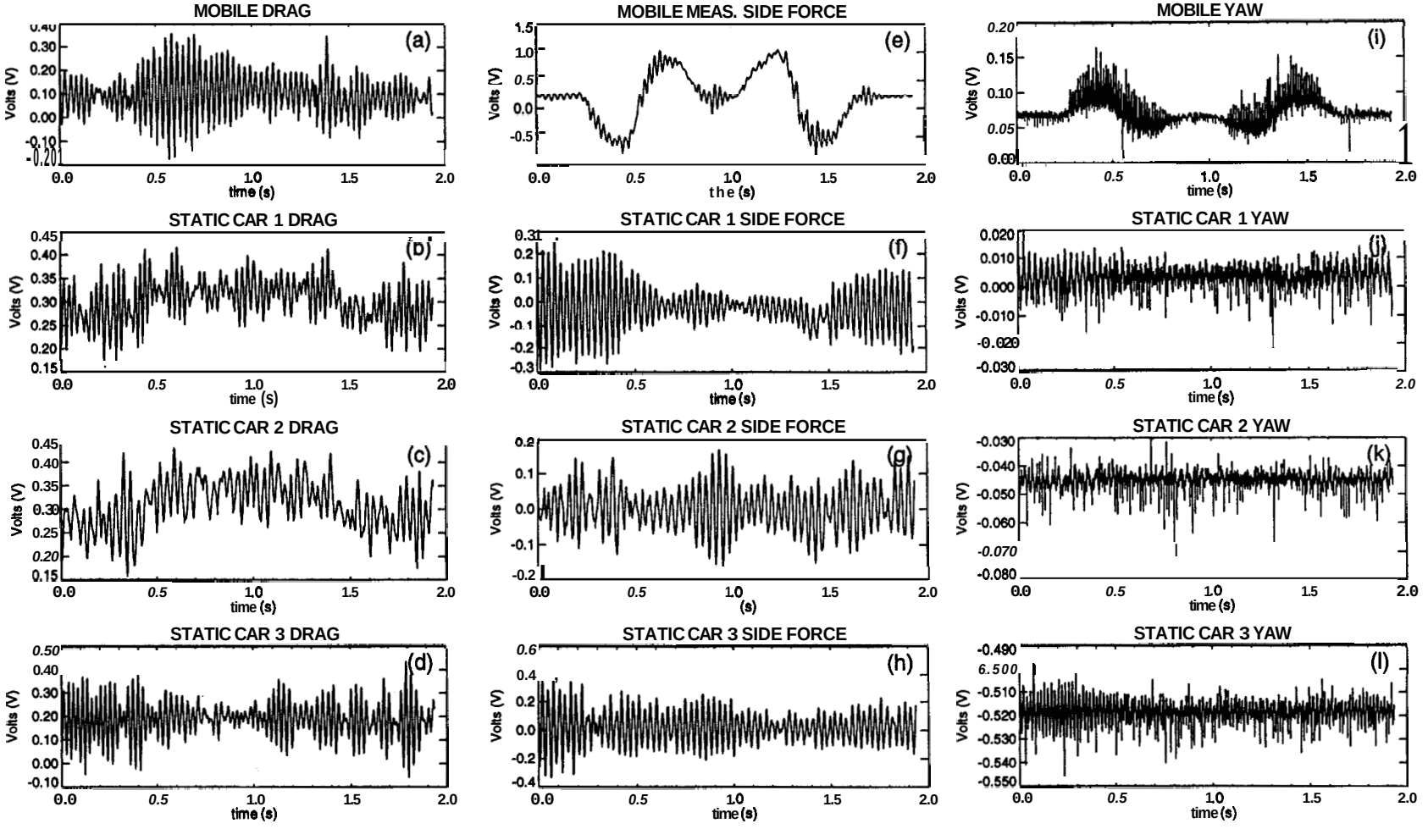

Figure **5.1:** Measured signals.

The measured signals are affected by electrical and mechanical noise. The drag [frames (a)-(d)], side force,[frames(e)-(h)], and yawing moment [frames(i)-(l)] from each balance inside the four **cars** in the platoon are shown.

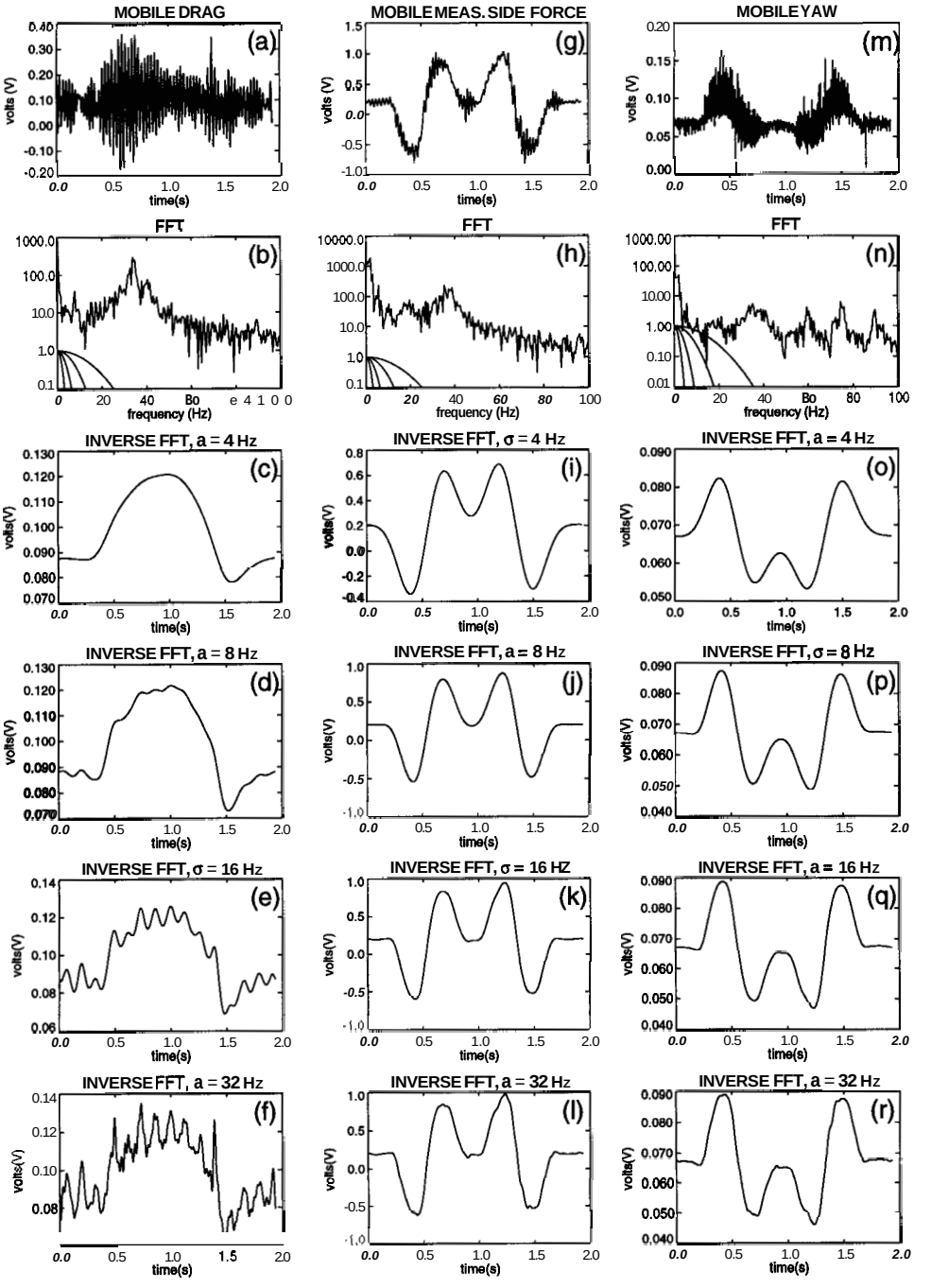

Figure 5.2: Filtering of mobile car signals.

Frames (a), **(g),** (m) show the original measured signals of drag, side force, and yawing moment. Frames (b), (h), (n) show the signals in the Fourier domain and the Gaussian windows. Frames (c)-(f), (i)-(l), (o)-(r) show the effects of altering the filter width.

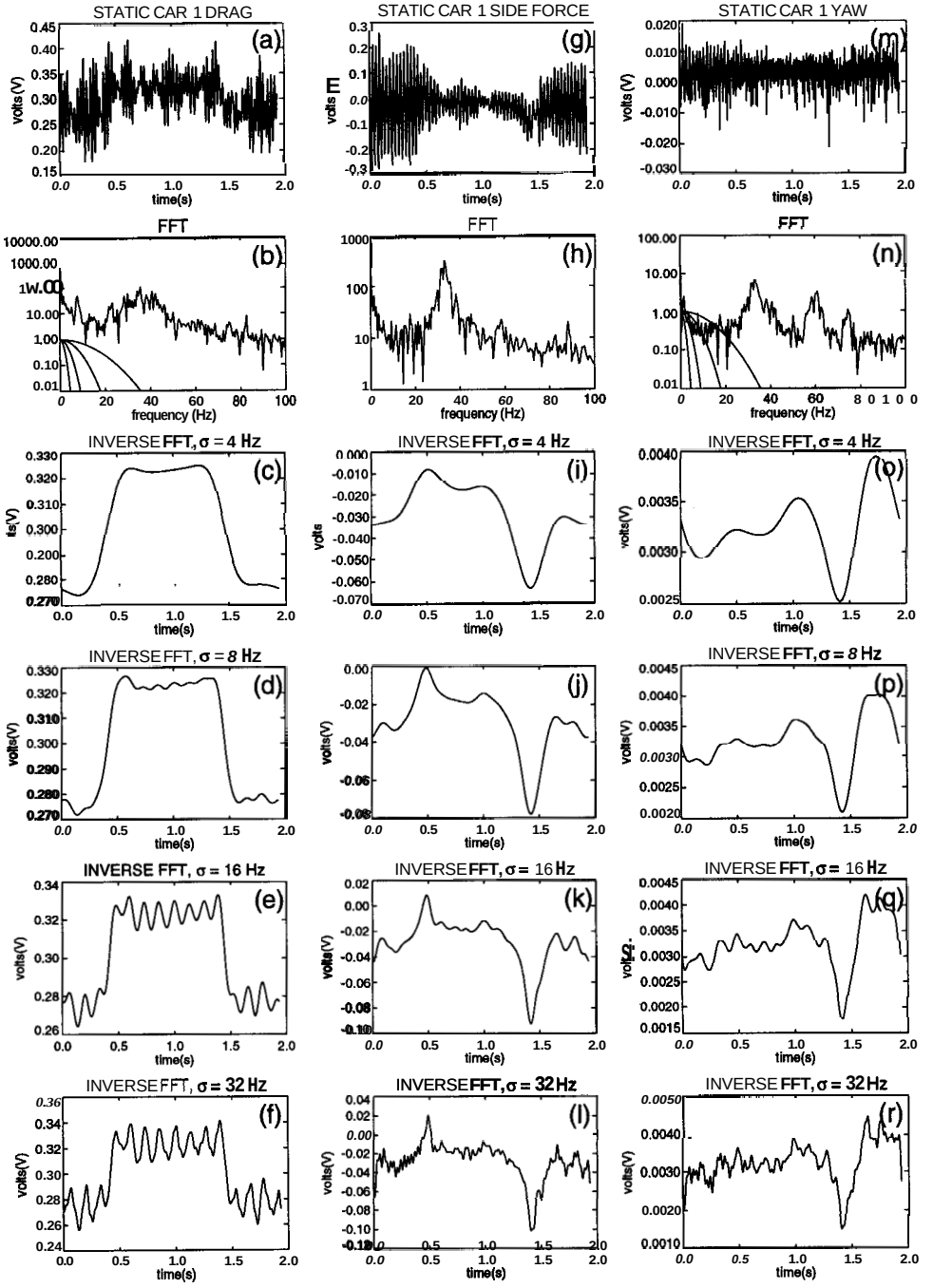

Figure **5.3:** Filtering of first static car signals.

Frames (a), **(g),** (m) show the original measured signals of drag, side force, and yawing moment. Frames (b), (h), (n) show the signals in the Fourier domain and the Gaussian windows. Frames (c)-(f), (i)-(l), (o)-(r) show the effects of altering the filter width.

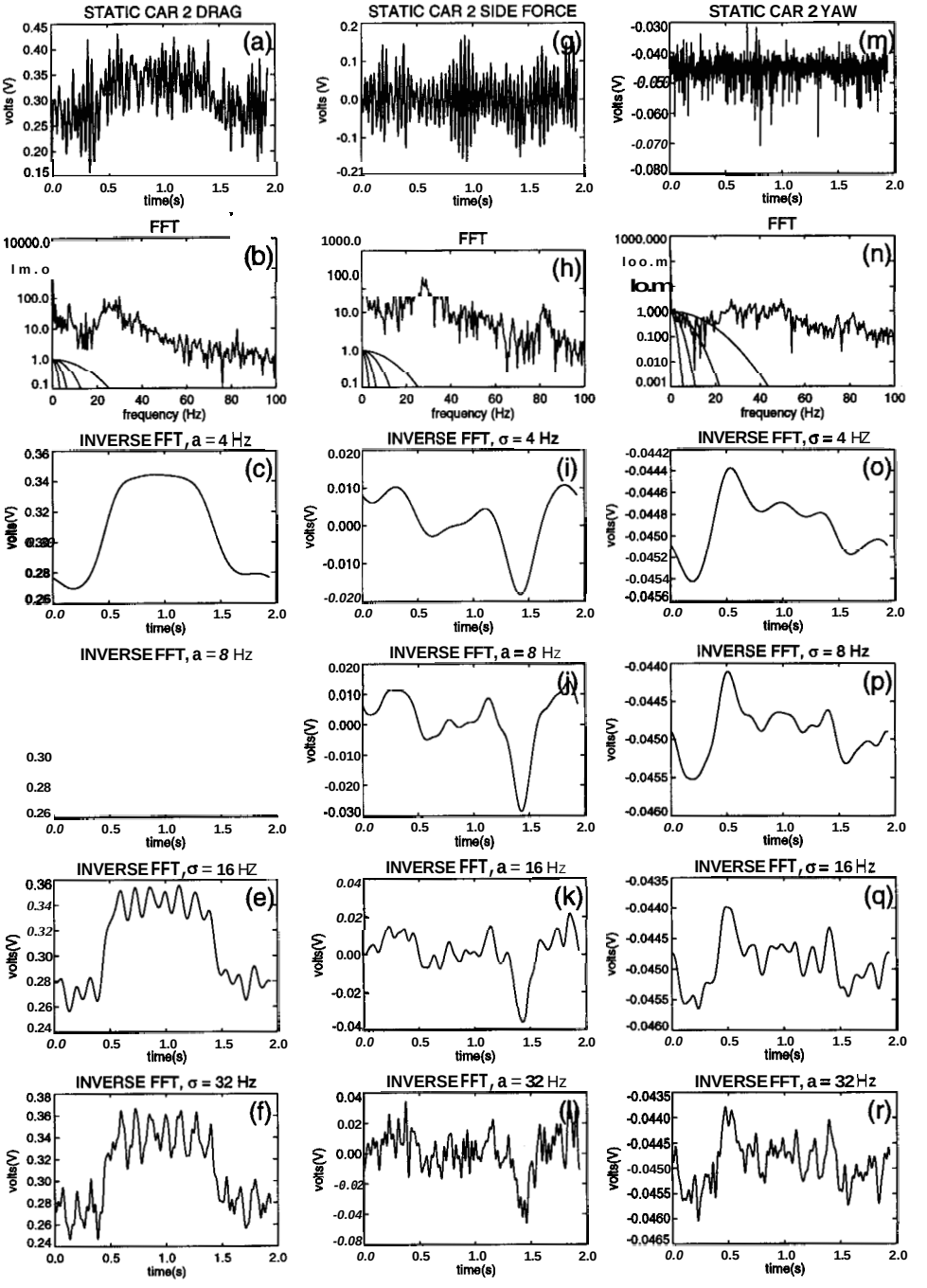

Figure 5.4: Filtering of second static car signals.

Frames (a), **(g),** (m) show the original measured signals of drag, side force, and yawing moment. Frames (b), (h), (n) show the signals in the Fourier domain and the Gaussian windows. Frames (c)-(f), (i)-(l), (o)-(r) show the effects of altering the filter width.

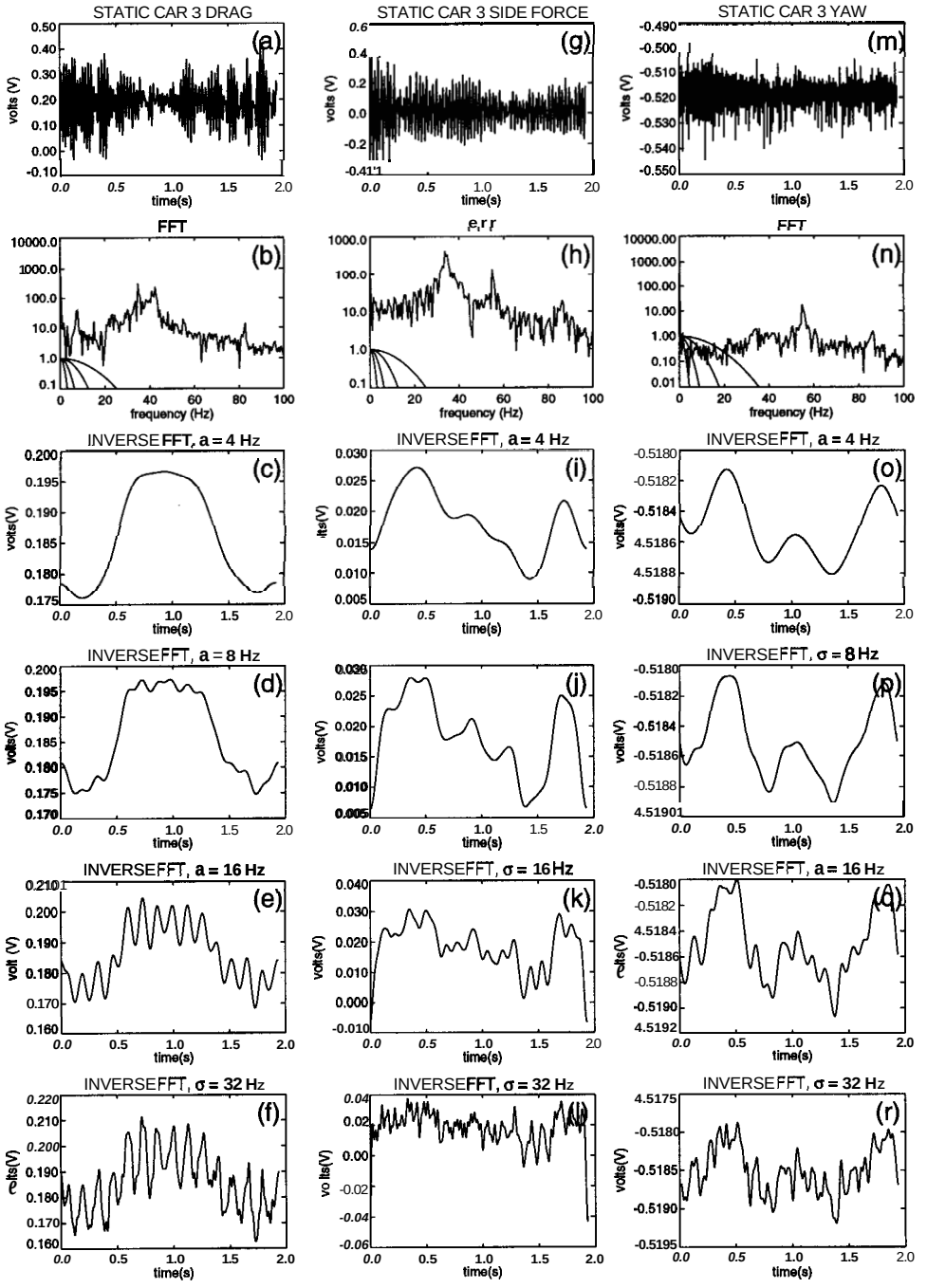

Figure ***5.5:*** Filtering of third static car signals.

Frames (a), (g), (m) show the original measured signals of drag, side force, and yawing moment. names (b), (h), (n) show the signals in the Fourier domain and the Gaussian windows. names (c)-(f), (i)-(l), (o)-(r) show the effects of altering the filter width.

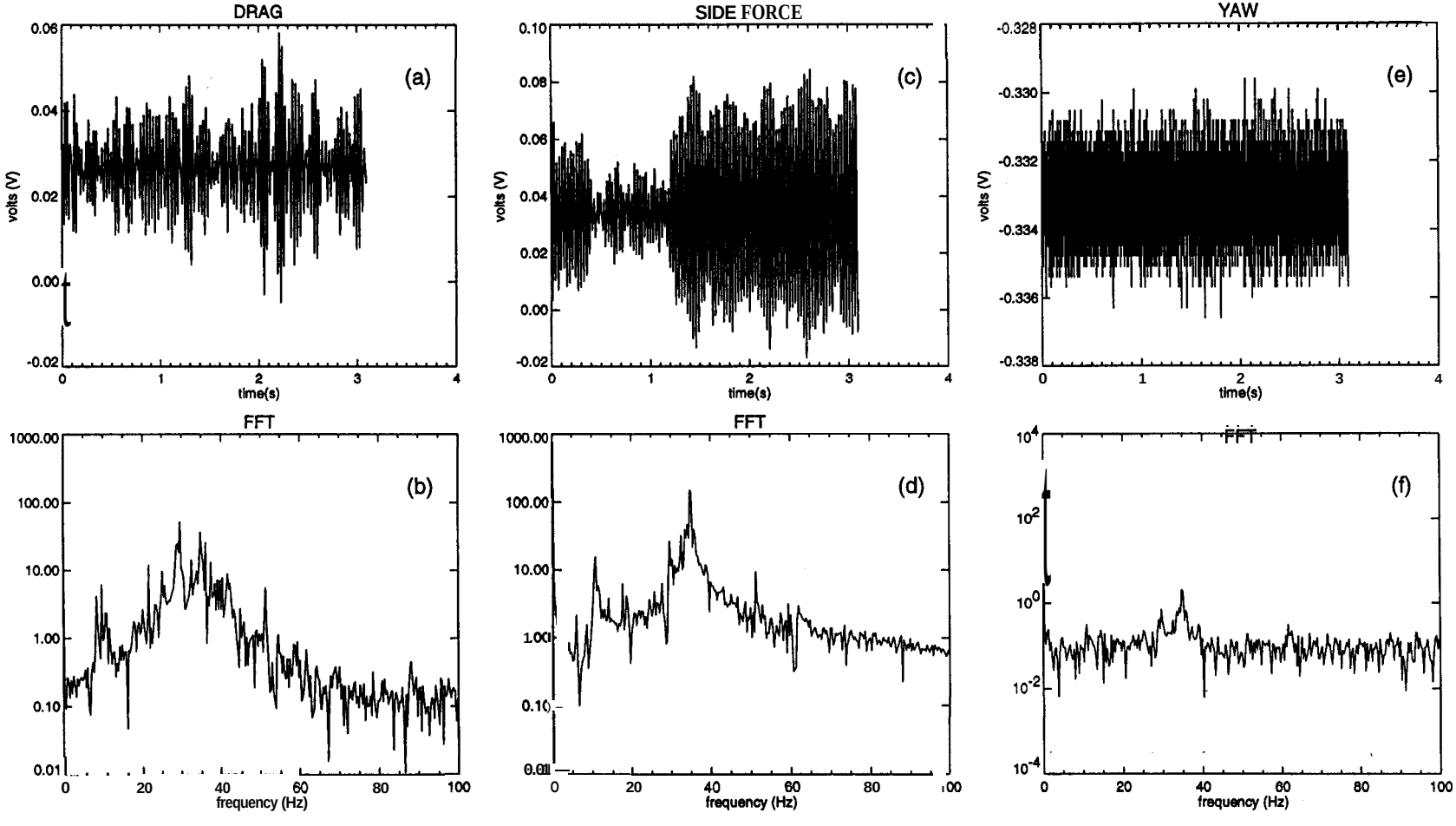

Figure 5.6: System resonance.
The frequency response of a balance when tapped is shown. The frequency spectra of the drag, side force, and yawing moment are shown.

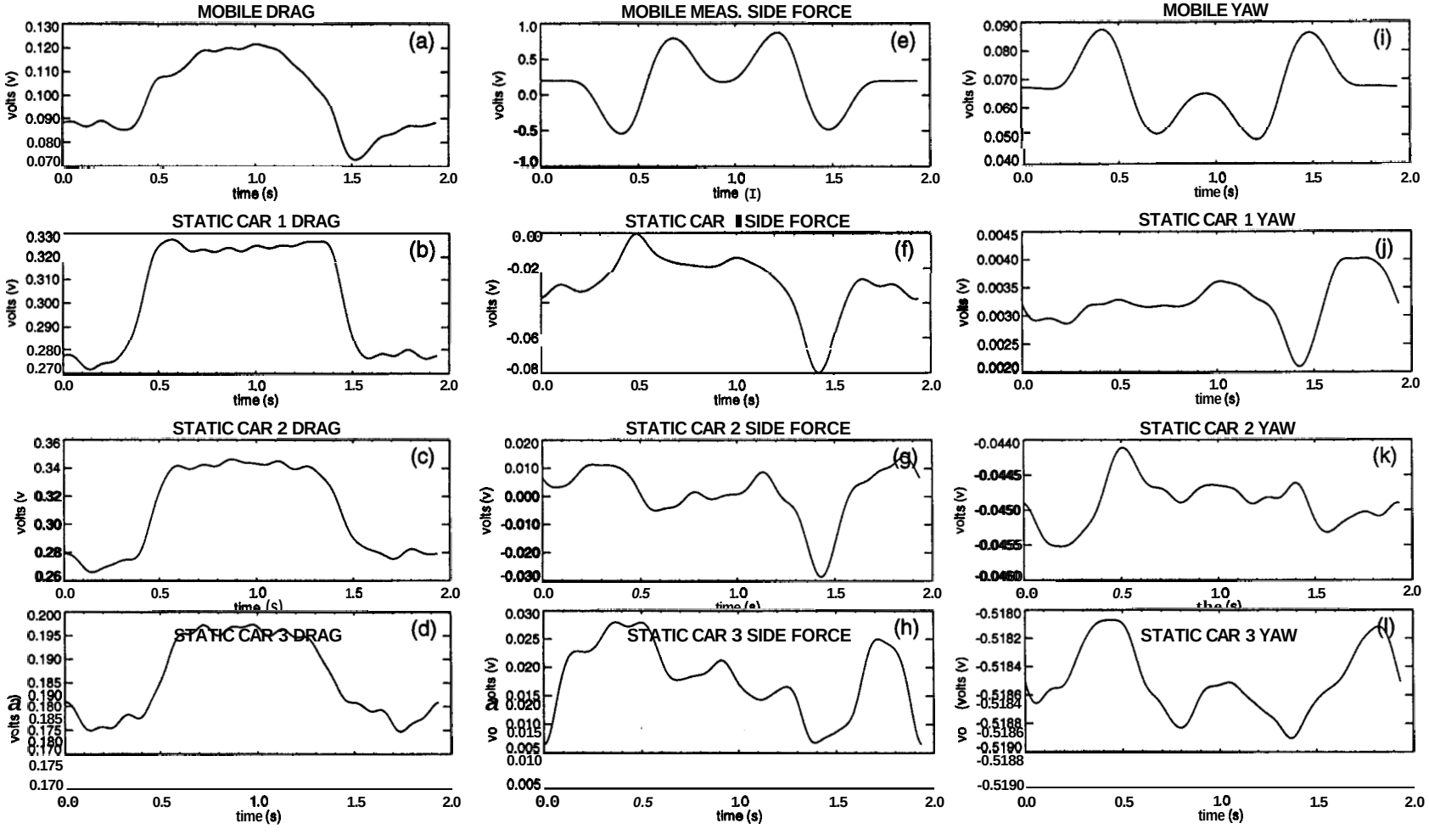

Figure **5.7:** Filtered signals.

The filtered signals obtained by applying a Gaussian window with a = 8.0 Hz are summarized. The drag [frames (a)-(d)], side force [frames(e)-(h)], and yawing moment [frames(i)-(l)] for each balance are shown.

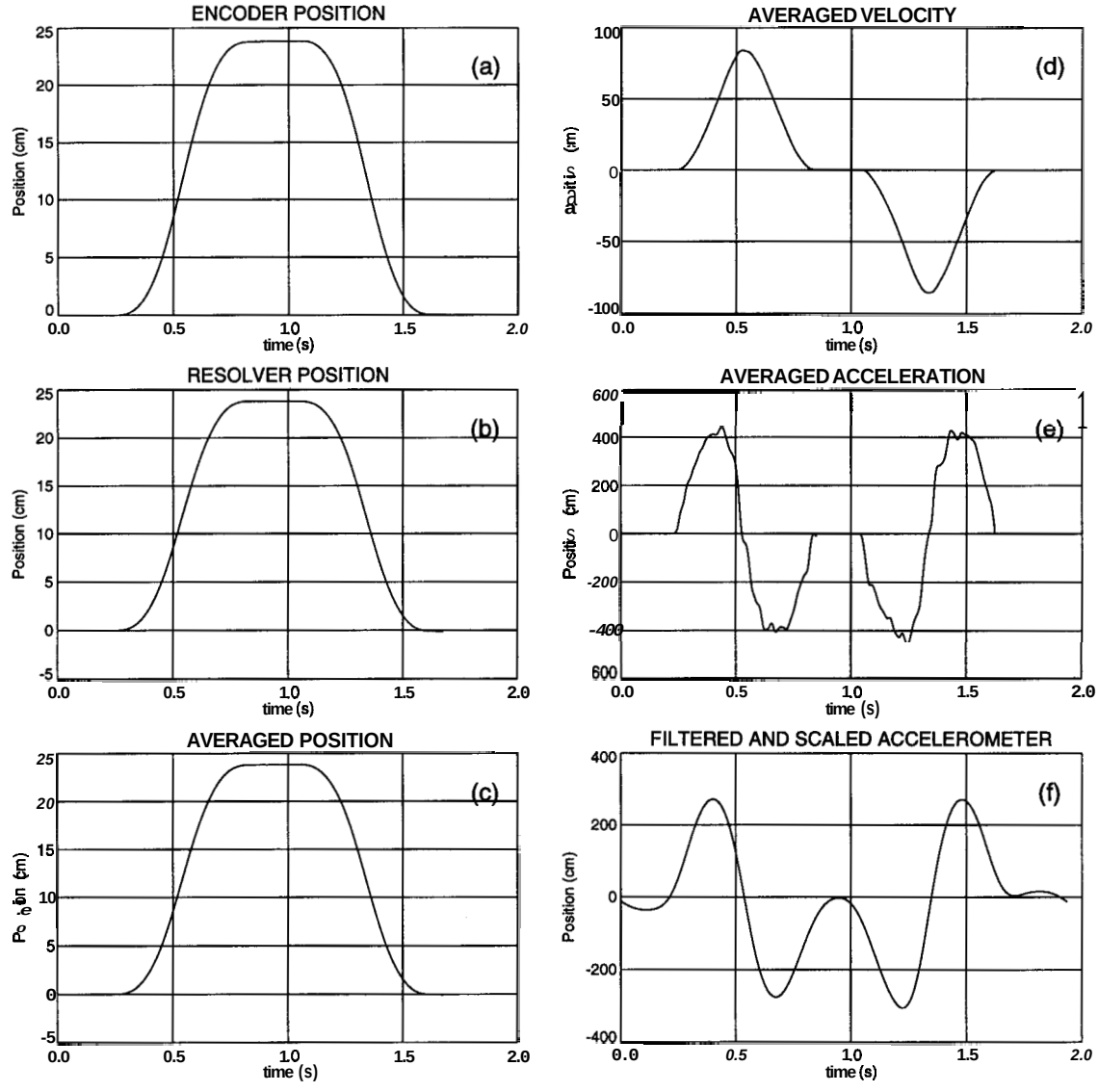

Figure 5.8: Encoder, resolver, and accelerometer profiles.

Frames (a), (b), (c) show the position from the encoder and resolver and their average, respectively. Frame (d) shows the velocity from the average position profile. Frames (e), (f) show the acceleration derived from the encoder/resolver and the accelerometer, respectively.

Chapter 6

Discussion of Results

Measurements are made for several cases of a single car and a platoon of cars. Static measurements are made with several separations between the vehicles in the platoon and lateral displacement of one of the vehicles in the platoon. Transient measurements are made with one vehicle in the platoon simulating a leaving and joining maneuver. The effects of the time scale of the maneuver, separation of the vehicles, and location of the maneuvering vehicle are discussed. The effect of the shape of the vehicles composing the platoon is determined by making measurements for a single rectangular box and a platoon of boxes. All of the results are presented as nondimensionalized coefficients as discussed in Section 2.2. The side force and yawing moment measured on the car or box simulating a lane change are shown for completeness, but will not be discussed because the inertial force could not be reliably extracted from the total measured force to determine the force resulting from the flow dynamics. Due to the large amount of data, only a few representative plots are discussed here. **A** complete summary of the data appears in Chen, et. al. [27].

6.1 Single Car

The drag coefficient C_D of a single car model, described in Section 3.1, is measured to be about 0.3. To determine the effect of platooning, the drag coefficient for a car in a platoon $C_{Dplatoon}$ is scaled with that for a single car $C_{Dsingle}$ in Figure 6.1. The ratio of drag coefficients is plotted with respect to a car's possible location in the platoon in Figure 6.1(a). The three different spacings used between the cars in the platoon in the experiments are shown as curves. Examining the curve for an inter-vehicle spacing of 0.21, several interesting effects can be noted. From platooning, the drag reduction on the first car is about 20%. As the second car in the platoon, the drag reduction is about 35%. A maximum drag reduction of about 40% is achieved with the third car in the platoon. A smaller drag reduction of about 25% is achieved on the last car. These trends are also reflected on the curves for other car spacings, though not as pronounced.

The effect of the spacing between the cars in the platoon on the drag coefficient can be more easily seen in Figure 6.1(b). Here, the ratio of the drag coefficient for a car in a platoon to that of a single car is plotted with the nondimensional car spacing l_l/l for each car position in the platoon, resulting in four curves. For all of the cars, a greater reduction in drag is achieved with smaller car separations. The drag reduction achievable with an inter-vehicle spacing of 0.21 can be 10% greater than that achieved with an inter-vehicle spacing of 1. Again, the highest reduction in drag appears on the third car in the platoon. For all of the vehicle separations, $C_{Dplatoon}/C_{Dsingle}$ is less than 1 for each car; thus, all of members of the platoon benefit from platooning by experiencing a reduction in drag compared to the case of a single car for all of the platoon configurations.

These results are comparable to those of Zabat, et. al. [7], which are shown as symbols for comparison. Zabat, et. al. also found that the interior vehicles in their four

vehicle platoon experience the most drag reduction, with the largest reduction occurring for the third vehicle. In addition, the largest reduction in drag for every vehicle in the platoon occurred at the smallest inter-vehicle separation. The experiments were conducted with scale model vans, which are larger and more blunt in shape than the sedans used here, accounting for the differences in the quantitative results. The qualitative trends are, nevertheless, the same.

6.2 Single Box

To further determine the influence of vehicle shape on the flow dynamics, measurements on boxes of equivalent size as the sedans are also made as described in Section 4.4. The C_D for a single box is about 1.0, which is much higher than that for a single car due to extensive flow separation. The drag reduction achieved by platooning for the box shape is also shown in Figure 6.1(a). The ratio of the drag coefficients for a single box to that of a box in a platoon is plotted with the position of the box in the platoon for a box separation of $0.4l(s_d)$. A 15% reduction in drag is obtained for the first box in the platoon. The second box experiences a drag reduction of about a 55%. As with a platoon of cars, the largest drag reduction is realized on the third box and is about 70%. The last box in the platoon has a drag reduction of about 60% compared to the case of an isolated box.

The box is a bluff shape with sharp corners, resulting in a drag coefficient that is more than three times larger than that of a car model. Since the box originally has a large drag coefficient, a greater reduction in drag is achieved from platooning. Though the effects of platooning are less pronounced on the car models, with their more streamlined shape, a reduction in drag is still observable, as discussed above. The differences in the results between a platoon of boxes and a platoon of cars show that the flow dynamics depend upon

the shapes and sizes of the vehicles composing the platoon. The influence of vehicle shape on the platoon dynamics is further discussed below.

6.3 Static Results

6.3.1 Effect of Location of Lateral Displacement

To obtain measurements for several lateral displacements of one member of the platoon, the mobile car is moved on a time scale that is much larger than the flow time scale, resulting in quasi-steady measurements. Since the mobile car is moved laterally at a velocity of 8 cm/s and the flow velocity is 20 m/s, the lateral movement of the mobile car is 250 times slower than the flow; thus, the flow has ample time to recover from the disturbances caused by the lateral motion of the model. Using this method, steady measurements for several lateral displacements can be obtained during one experimental run. For all of the results discussed below, the mobile car moves out of the platoon $2.5w$, and pauses for $0.3s$, which is equivalent to 24 car lengths at a flow velocity of 20 m/s; thus, this pause allows enough time for the flow to fully recover from the motion out of the platoon. After this pause, the mobile car returns back into the platoon. The location of the mobile car is varied to be any one of the four cars in the platoon as described in Section 4.4. The changes in the drag coefficient, side force coefficient, and yawing moment coefficient are measured on each vehicle in the platoon during the entire lateral motion of the mobile car.

These results are shown in Figure 6.2 with respect to the lateral displacement d of the moving car, which has been scaled with the vehicle width w. The drag coefficient on each car in the platoon is shown in frames (a)-(d). The side force coefficient is shown in frames (e)-(h), and the yawing moment is shown in frames (i)-(l). In this figure and all of the following figures, the first static car always refers to the first of the three stationary

cars, regardless of the location of the displaced car in the platoon. The same applies for the second and third static cars. Thus, the fact that the displaced car changes its location in the platoon should be kept in mind. The laterally displaced car moves a total distance of $2.5w$ out of the platoon in Figure 6.2. The different linetypes in each frame represent the four possible locations of the laterally displaced car in the platoon. For each type of line, three curves are shown, representing the three trials conducted with that particular platoon configuration. Figure 6.2 shows the results when the inter-vehicle spacing is 0.21.

Examining Figure 6.2, the largest effects appear on the closest neighbors of the laterally displaced car. First, examining the drag coefficient, the largest change occurs for the car immediately ahead of the laterally displaced car. At a lateral displacement of about $0.5w$, the drag begins to increase, reaching a value about 30% greater than its original value in a streamlined platoon. For the car immediately behind the laterally displaced car, the drag coefficient also begins to increase when the lateral displacement is $0.5w$ and increases to a value about 20% greater than its initial value. For the laterally displaced car, the increase in drag, when the car leaves the platoon, becomes larger when the car is located farther back in the platoon. When the car is located at the head of the platoon, the increase in C_D is about 20%, while the increase is about 60% when the car is located at the rear of the platoon.

Examining the side force coefficient C_S, the car immediately behind the laterally displaced car is affected the most. The following car experiences a side force which is at least 2 times, but can be as much as 4 times, larger than its initial value in a direction opposite to the direction of displacement (hence, the negative values of C_S). The following car experiences this force until the lateral displacement of the mobile car is about $0.5w - lw$. Then, the side forces changes direction, and the car experiences a force in the same direction

as the displacement (positive C_S). This side force is about 1.5 to 3 times the original value. The car immediately in front of the laterally displaced car experiences a slight side force in the same direction as the displacement until the displacement is about 0.220. Then, the car experiences a large force, about 2 to 4 times the initial value, in the opposite direction until the displacement is about 1.520. Then, the side force again changes to the same direction as the displacement. The side forces on the remaining cars in the platoon behind the laterally displaced car follow the same trend. These cars also initially experience a slight side force in same direction as the displacement. When the displacement is about $0.5w$, the side force changes to a direction opposite of the displacement. At about $1.5w$, the side force changes to the same direction as the displacement. These changes in the side force coefficient are much larger than the changes in the drag coefficient, although the magnitudes are small. Therefore, these changes are significant and cannot be ignored.

Some changes appear on the yawing moment coefficient as one of the cars is laterally displaced. However, no general trends are observable. In addition, the magnitudes of the yawing moment coefficient are very small, on the order of 10^{-4}. To better quantify changes in the yawing moment, lighter models are required.

Figure 6.3 corresponds to the case of Figure 6.2, where the vehicle separation is 0.21. However, in Figure 6.3, the measurements begin with the maximum lateral displacement of $2.5w$, and the mobile car is slowly moved into the platoon. The curves end at 0.2520, because the time of the car's return into the platoon was longer than the data acquisition time. By comparing Figures 6.2 and 6.3, the forces and moments display the same behavior for either case of outward displacement from the platoon or inward displacement into the platoon.

6.3.2 Effect of Longitudinal Spacing

Figures 6.4 - 6.6 show the force and moment coefficients as a function of the nondimensional lateral displacement d/w and the inter-vehicle spacing. In these figures, one car is displaced outward from its initial position in the platoon. Each figure represents a different location of the displaced car in the platoon. Figure 6.4 is the case of displacement of the first car in the platoon. Figure 6.5 shows the displacement of the third car, representing a case of the displacement of an intermediate car. Figure 6.6 is the case of displacement of the last car in the platoon. In these figures, the different linetypes represent the three vehicle spacings used in the experiment. The three curves for each linetype represent the three experimental trials. One immediate observation is that larger changes in the force coefficients occur for smaller vehicle spacings. The change in the drag coefficient for all of the cars is largest at 0.21 spacing. The change in the side force coefficient is also largest at 0.21 spacing. These changes in the force coefficients are largest for the car positioned just behind the laterally displaced car. The other following cars also experience these changes but to a lesser degree. Also, changes in the yawing moment are largest on the car immediately behind the maneuvering car and very small for the remaining cars.

Figure 6.7 corresponds to the case shown in Figure 6.5, except that the displaced car is moving into the platoon from an initial displacement of 2.520. Again, the curves end at a displacement of 0.2520, because the car's return into the platoon exceeded the data acquisition time. As noted above, the changes in the force coefficients do not depend upon the direction of the displacement (either into or out of the platoon).

6.4 Transient Results

6.4.1 Effect of Maneuver Time Scale

To measure the transient aerodynamic forces generated during lane change maneuvers, one car is moved out of the platoon and returned into the platoon at six different accelerations, as shown in Tables 5.1 and 5.2, to simulate lane changes of different time scales. Figures 6.8 - 6.10 show the force and moment coefficients with respect to the nondimensional lateral displacement d/w of the moving car for all six acceleration profiles, shown as different linetypes. Each figure represents a different position of the moving car in the platoon for an inter-vehicle spacing of 0.21. In Figure 6.8, the first car is the maneuvering car. Figure 6.9 represents the case of an intermediate member performing the maneuver. In Figure 6.10, the last car is the mobile vehicle. In all the figures, the actuated car is moved out of the platoon to a final distance of $2.5w$. For simplification, the three experimental trials of each acceleration profile are averaged and shown as one curve in these figures. The slowest acceleration, profile 1, represents the quasi-steady case t_∞ as discussed above and is shown as a solid line in the following figures for comparison. Acceleration profile 4 represents the design time scale $t_d = 0.5$ seconds, equivalent to a lane change maneuver which takes 5 seconds by a full scale vehicle. The fastest acceleration, profile 6, is equivalent to a time scale that is half of design $0.5t_d$.

The largest effect appears on the car immediately following the moving car. Similar changes in the drag coefficient occur for all of the acceleration profiles. The drag coefficient begins to increase when the moving car is at a distance of $0.5w$ away from the platoon, eventually resulting in a 15%-35% increase in C_D, depending upon the location of the maneuvering car in the platoon. At accelerations equivalent to time scales longer than t_d, the side force shows similar trends to the static case described in detail above. The side

force on the car immediately behind the mobile car experiences a large force in a direction opposite to the mobile car's motion. However, as the acceleration increases and the time scale of the lane change becomes shorter than t_d, *the direction* of *the side force changes on the cars following the moving car.* **As** the mobile car leaves the streamlined flow of the platoon, the side force applied to the car immediately behind is now in the same direction as the motion. When the moving car is about $0.5w - lw$ away from the platoon, the following car then experiences a side force in a direction opposite to the mobile car's direction of motion. An important observation is that *this effect does not appear on the cars ahead of the maneuvering car.* Some changes are observed on the yawing moment coefficients, especially on the car immediately behind the mobile car. However, general trends are again difficult to determine.

Figure *6.11* shows the force and moment coefficients as the mobile car moves into the platoon at an intermediate location and a spacing of *0.21.* The curves extend from a displacement of $2.5w$ to $0.25w$, because the motion into the platoon was longer than the data acquisition period. Comparing Figure *6.11* to Figure **6.9,** the side force, along with the drag and yawing moment, shows the same trends when the mobile car joins the platoon as when the mobile car leaves the platoon at accelerations equivalent to time scales greater than t_d. When the mobile car moves into the platoon on a time scale smaller than t_d, the side force continues to exhibit the same trends. However, as noted above, the side force changes direction for the case of outward motion of the mobile car when the acceleration exceeds the design acceleration. Therefore, *the side force coefficient displays a hysteresis at time scales shorter than* t_d *for cars behind the car performing a lane change maneuver.* By examining all of the plots showing the effect of the vehicle separation or of the location of the lane change maneuver [27], the hysteresis of the side force coefficient is clearly a function

of the acceleration of the mobile car and occurs for all vehicle separations and locations of the mobile car in the platoon.

6.4.2 Effect of Inter-Vehicle Spacing

Figures 6.12 - 6.14 show the effect of the longitudinal spacing between the vehicles on the transient forces and moments. The nondimensional coefficients are plotted with the nondimensional lateral displacement of the maneuvering vehicle. The different linetypes represent the three inter-vehicle spacings, and all three experimental trials are shown. In each of these figures, the mobile car is moved out of the platoon at the design acceleration, but from a different position in the platoon. In Figure 6.12, the mobile car is the lead car in the platoon. In Figure 6.13, the mobile car is an intermediate car. In Figure 6.14, the mobile car is the last car. As in the static case, a larger change in the drag coefficient is observed at smaller separations. The change in the side force coefficient is also greater for smaller inter-vehicle spacings. The largest changes occur for the car immediately behind the moving car. The effects are smaller for the other following cars, but the changes are still evident. Any changes on the yawing moment coefficient are small and difficult to define, although the largest change appears to be on the car following the maneuvering car. These effects are observable for all locations of the mobile car in the platoon.

6.4.3 Effect of Maneuver Location

Figure 6.15 shows the effect of changing the location at which the lane change maneuver occurs in the platoon. The force and moment coefficients are shown with the nondimensional displacement of the maneuvering vehicle. The different linetypes represent a different member of the platoon performing the lane change maneuver. The three experimental trials are shown for each location. In this case, the inter-vehicle spacing is 0.21 and the acceleration

is equivalent to the design time scale t_d. The mobile car moves outward from the platoon. In this figure, the car immediately ahead of the moving car experiences the largest change in drag when the mobile car leaves the platoon, increasing to a value 20%-40% greater than its initial value in the streamlined platoon. The largest increase occurs when the mobile car is the last member in the platoon. The drag coefficient also increases for the remaining cars in the platoon, but the effect is smaller. The largest change in the side force coefficient occurs for the cars immediately ahead of and behind the mobile car in the platoon. The side forces that these cars experience are initially in the same direction as the motion of the mobile car. The side force changes to the opposite direction at about $0.2w$. At about $1.5w$, the side force changes to the same direction as the motion. For cars in the platoon located more than one car away from the mobile car, the side force increases slightly in the same direction as the motion. These trends appear regardless of where the lane change maneuver takes place in the platoon. Some changes are apparent on the yawing moment coefficient as the mobile car leaves the platoon. However, since the magnitudes are on the order of $10^{-3} - 10^{-4}$ and the changes are less than 10%, a general trend is difficult to determine.

6.5 Influence of Vehicle Shape

A platoon operating on an IVHS will realistically contain vehicles of various shapes and sizes. To determine the effect of the shape and size of the vehicles on the transient aerodynamics, additional measurements are made with a platoon of boxes with the same overall dimensions as the car models as described in Section 4.4. Since measurements are only made with one vehicle spacing of 0.41, the results are presented with respect to the different acceleration profiles and the location of the platoon maneuver. Figures **6.16** - **6.18** show the effect of the acceleration of the mobile box on the force and moment coefficients

for a specific location of the mobile box in the platoon. The coefficients are shown with the nondimensional lateral displacement d/w of the maneuvering box. The different linetypes represent the different acceleration profiles. Each curve is an average of the three experimental trials performed with that acceleration profile and platoon configuration. Figure **6.16** represents the case of the mobile box as the first member of the platoon. Figure **6.17** is the case when an intermediate box in the platoon performs a maneuver. Figure **6.18** is the case when the maneuvering box is the last box in the platoon. In all of these figures, the mobile box moves from its original position in the platoon outward to a lateral distance of $2.5w$. The measurements for the platoon of boxes show some of the same trends as those for the platoon of cars but to a greater degree. The change in the drag coefficient as the mobile box leaves the platoon is greatest for the box immediately behind the mobile box and can increase by as much as 2 to **3** times. The drag also increases on the other boxes in the platoon, but the change is smaller for boxes located farther away from the maneuver. For the boxes nearest the maneuver, the static case (shown as the solid line) produces the greatest change, while the highest acceleration profile produces the smallest change. For boxes located farther away, the greatest change occurs for the highest acceleration profile. In addition, the location at which the maximum change in the side force coefficient occurs appears to shift from $0.5w$ to $1w$ as the acceleration of the mobile box increases. **As** with the drag, the effects on the side force are less for boxes located farther from the mobile box. **As** with the platoon of cars, the changes in the yawing moment coefficient are difficult to characterize. Some changes occur for the boxes closest to the maneuvering box, but general trends are difficult to identify.

Figure **6.19** corresponds to the same case as Figure **6.17** of a maneuver at an intermediate location in the platoon, except that the mobile box now moves into the platoon

from an initial distance of $2.5w$. Again, the curves in Figure 6.19 end at $0.25w$, because the time for the return of the box into the platoon was longer than the data acquisition period. As with the platoon of cars, *the side force is nonmonotonic on the boxes behind the mobile box* when comparing the case of motion outward to motion inward and *when the maneuver occurs on a time scale less than* t_d. When the motion occurs on a time scale larger than t_d, the side force is initially in a direction opposite to the motion of the mobile box. However, when the time scale of the motion is shorter than t_d, the side force is in the same direction as the motion. As with the platoon of cars, *this hysteresis does not appear on the boxes located ahead of the maneuvering box.*

Figure 6.20 shows the effect of the location of the maneuver in the platoon on the measured forces and moments when the mobile box moves outward at the design acceleration, equivalent to the design time scale t_d. The force and moment coefficients are plotted with the nondimensional displacement of the mobile box. The different linetypes represent the four possible locations of the maneuvering box in the platoon, and all three experimental trials for each location are shown. **As** the mobile box leaves the platoon, the largest increase in the drag coefficient occurs on the box immediately behind the moving box, and the drag increases by as much as 2.5 times. Boxes located farther away from the mobile box experience slighter increases. The change in the side force coefficient is greatest for the box located immediately in front of the mobile box. The side force is in a direction opposite to the motion of the mobile car, reaching a maximum at about $2w$. As with the car platoon, the box located immediately behind the moving box experiences a slight side force in the same direction as the motion of the maneuvering box. Then, the following box experiences a side force in a direction opposite to the motion, reaching a maximum at about $0.5w - w$. Then, the side force on the following box is in the same direction as the motion, returning

nearly to its original value when the mobile box is $2.5w$ away from the platoon. Because of their more streamlined shape, this behavior is not as obvious with a platoon of cars. These trends also occur for the side force on boxes located more than one box away from the mobile box, although these effects are less noticeable. For the yawing moment, general trends are difficult to identify.

6.6 Figures

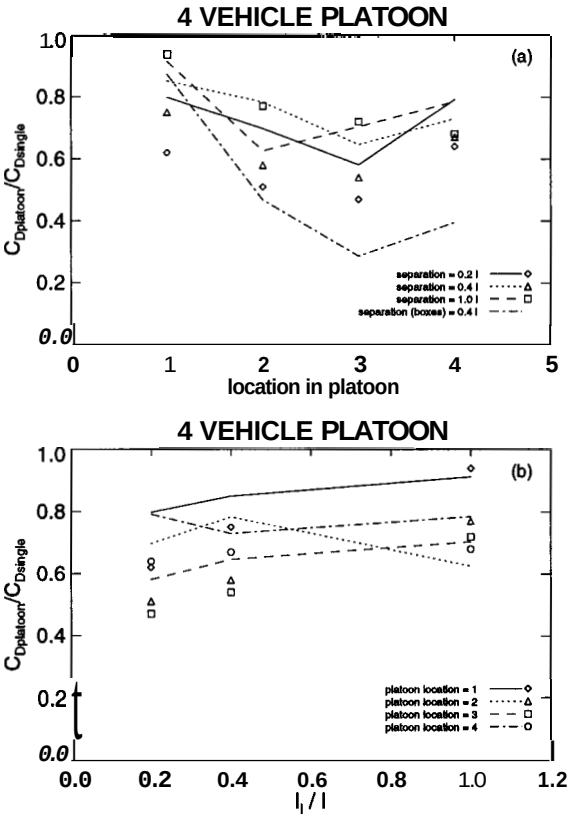

Figure 6.1: Drag reduction.

names (a) and (b) show the ratio of the drag coefficient for vehicles in a platoon to that of a single vehicle versus the vehicle location in the platoon and the vehicle separation, respectively. The data of this study are shown as lines, while those of Zabat, et. al. [7] are shown as symbols.

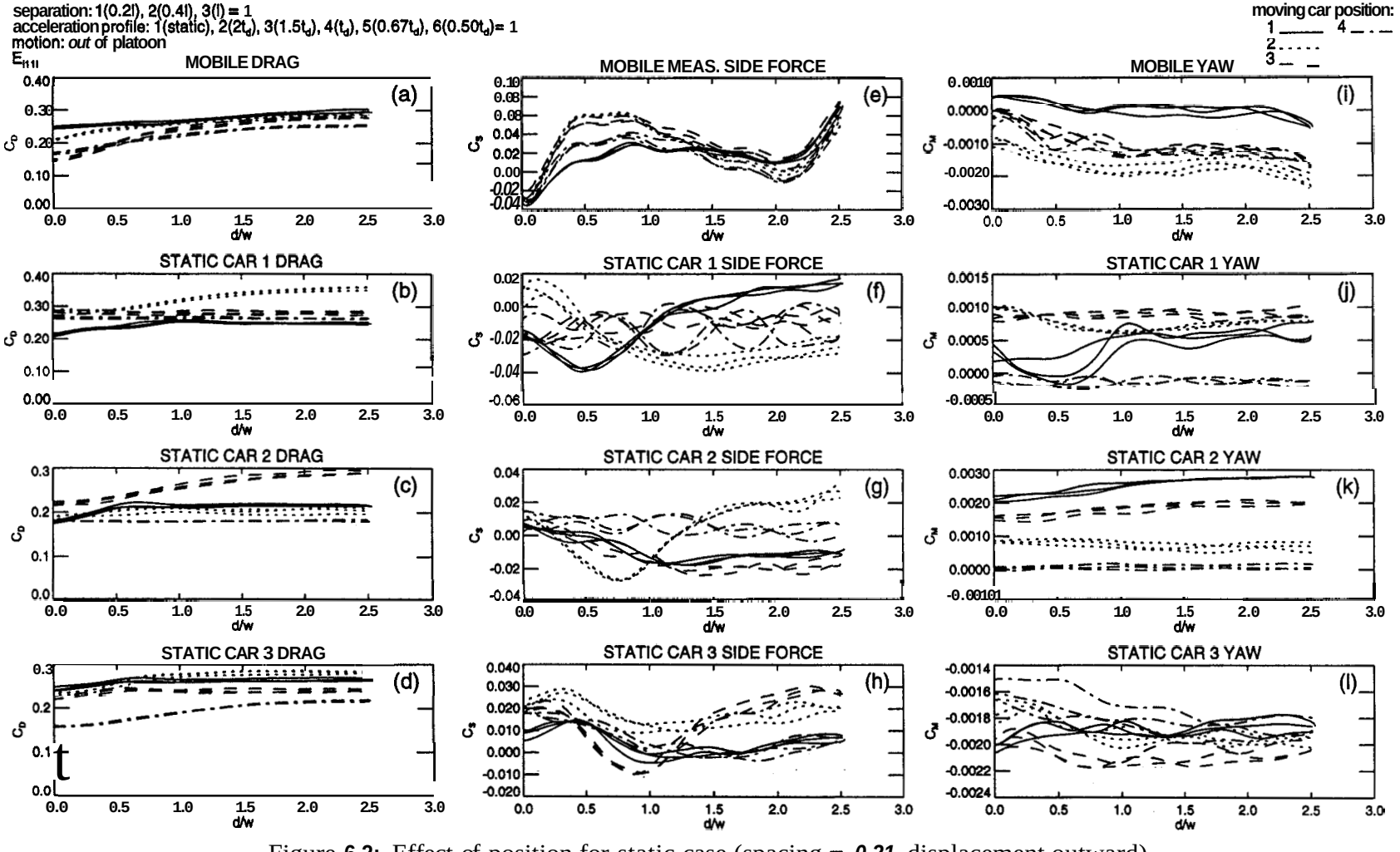

Figure **6.2:** Effect of position for static case (spacing = ***0.21,*** displacement outward). The drag [frames (a)-(d)], side force [frames(e)-(h)], and yawing moment [frames(i)-(l)] coefficients on each car are shown with respect to lateral displacement of the mobile car. The different lines represent the four possible locations of the mobile car in the platoon.

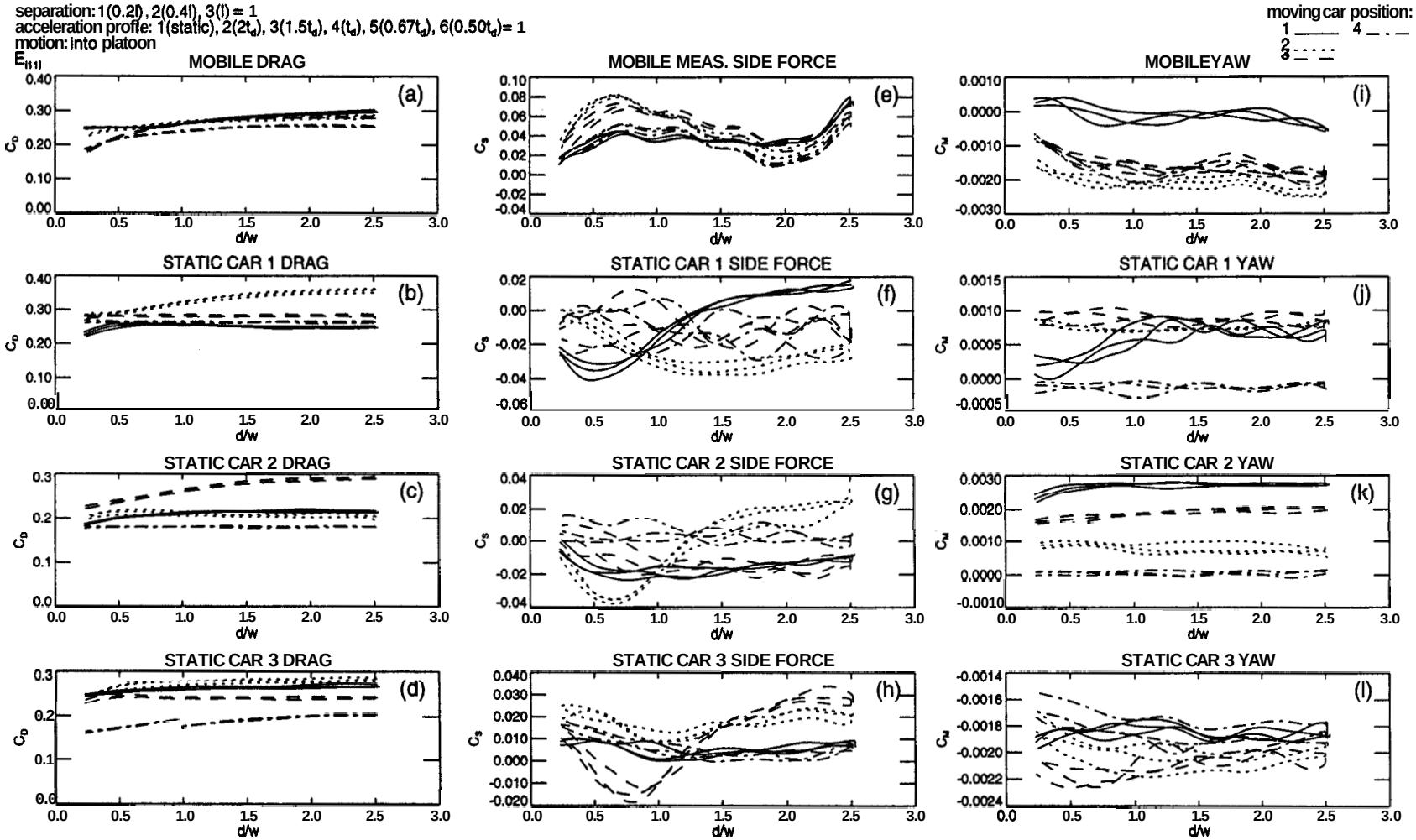

Figure **6.3:** Effect of position for static case (spacing = *0.21,* displacement inward). The drag [frames (a)-(d)], side force [frames(e)-(h)], and yawing moment [frames(i)-(l)] coefficients on each car are shown with respect to lateral displacement **of** the mobile car.. The different lines represent the four possible locations of the mobile car in the platoon.

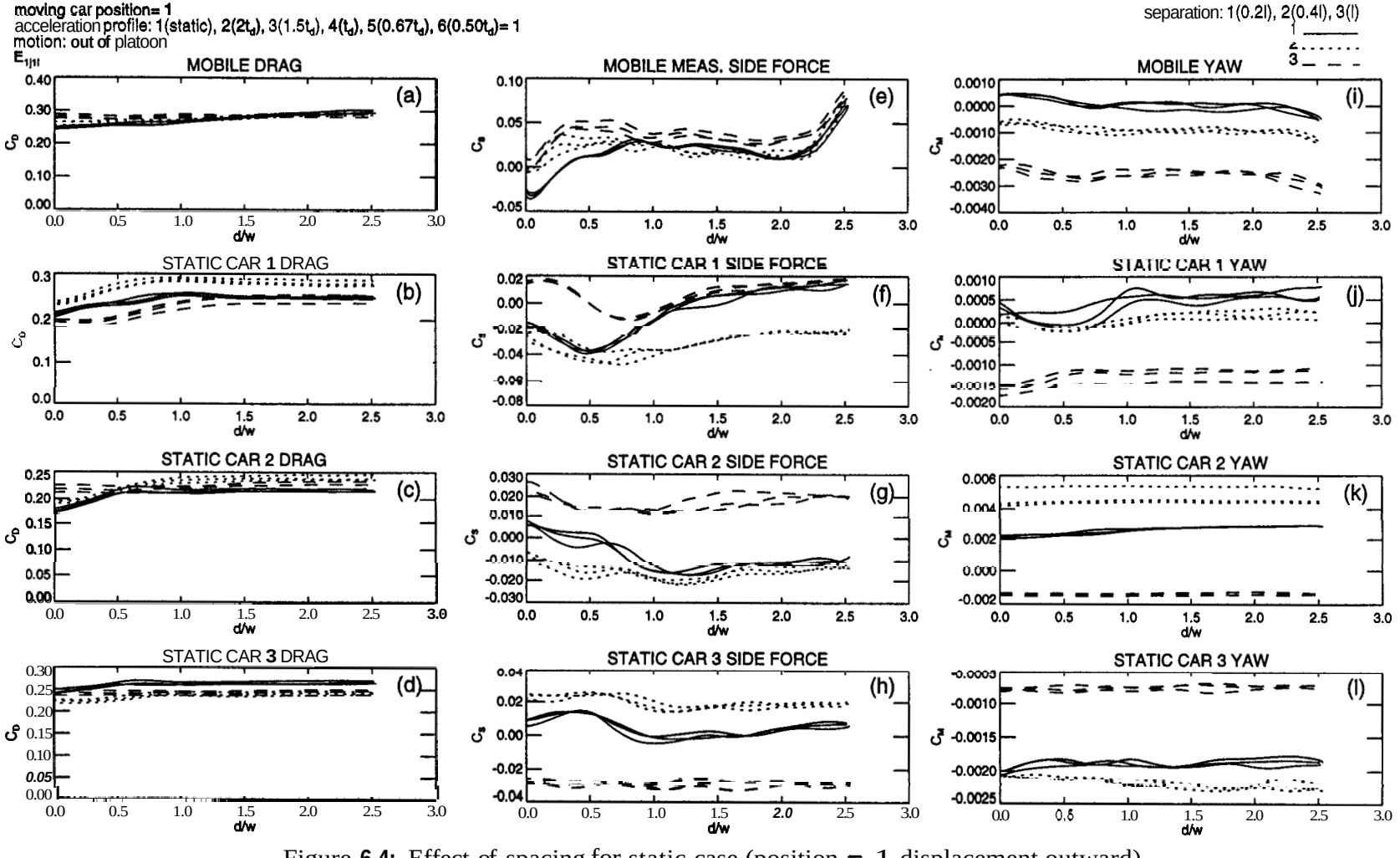

Figure **6.4:** Effect of spacing for static case (position = 1, displacement outward). The drag [frames (a)-(d)], side force [frames(e)-(h)], and yawing moment [frames(i)-(l)] coefficients on each car are shown with respect to lateral displacement of the mobile car. The different lines represent the three inter-vehicle spacings.

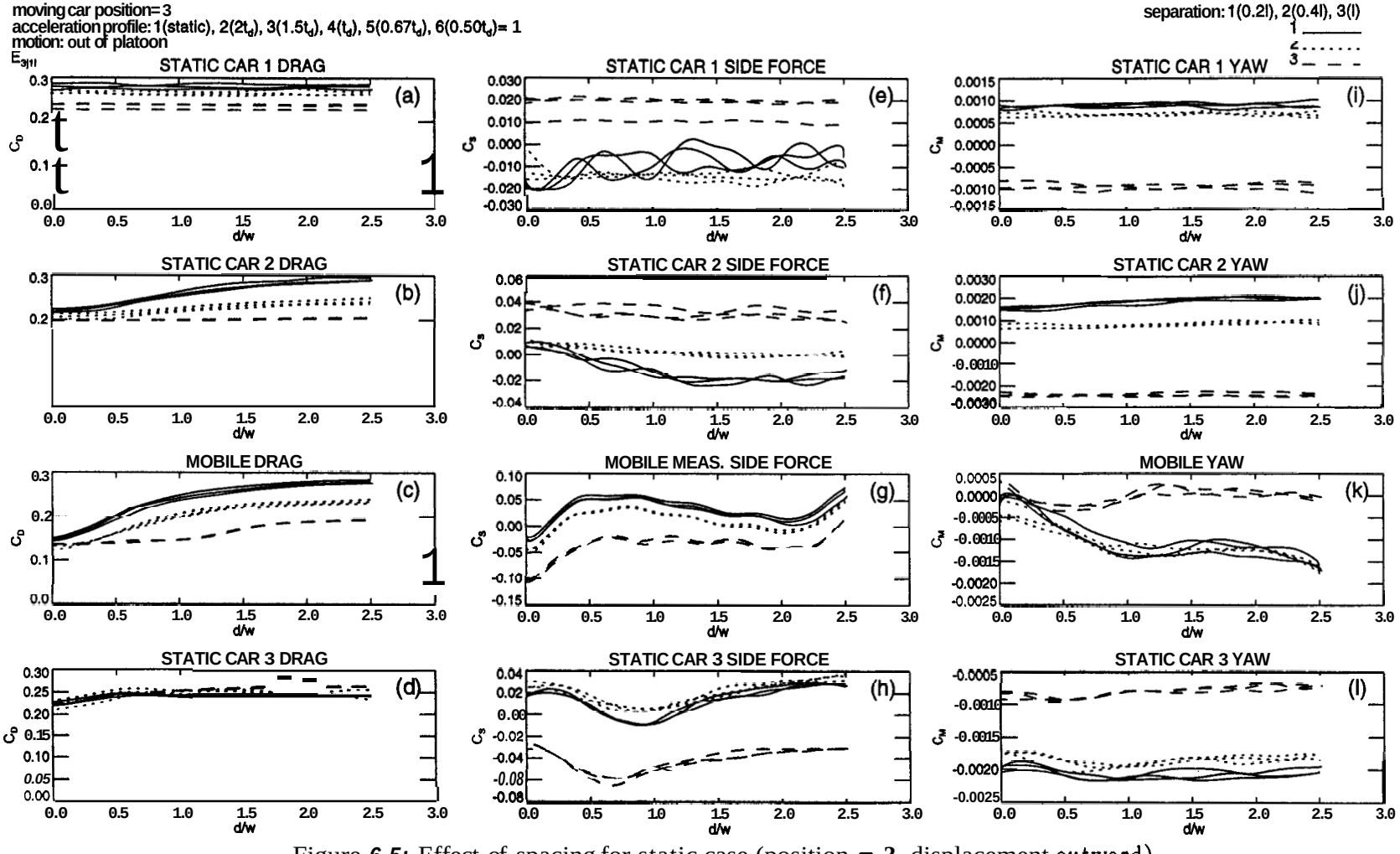

Figure *6.5:* Effect of spacing for static case (position = 3, displacement outward). The drag [frames (a)-(d)], side force [frames(e)-(h)], and yawing moment [frames(i)-(l)] coefficients on each car are shown with respect to lateral displacement of the mobile car. The different lines represent the three inter-vehicle spacings.

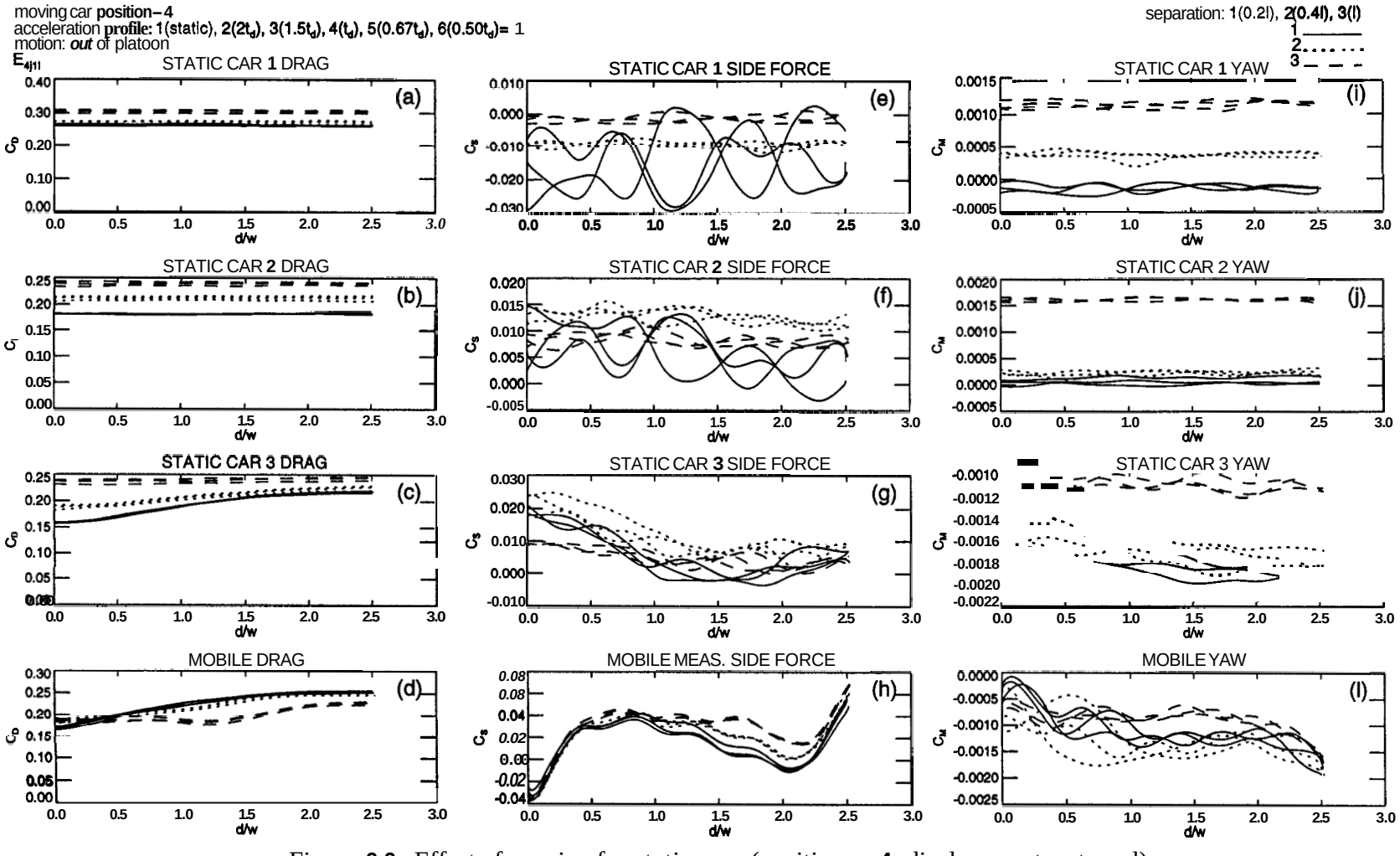

Figure **6.6:** Effect of spacing for static case (position = **4,** displacement outward). The drag [frames (a)-(d)], side force [frames(e)-(h)], and yawing moment [frames(i)-(l)] coefficients on **each** car are shown with respect to lateral displacement of the mobile car. The different lines represent the three inter-vehicle spacings.

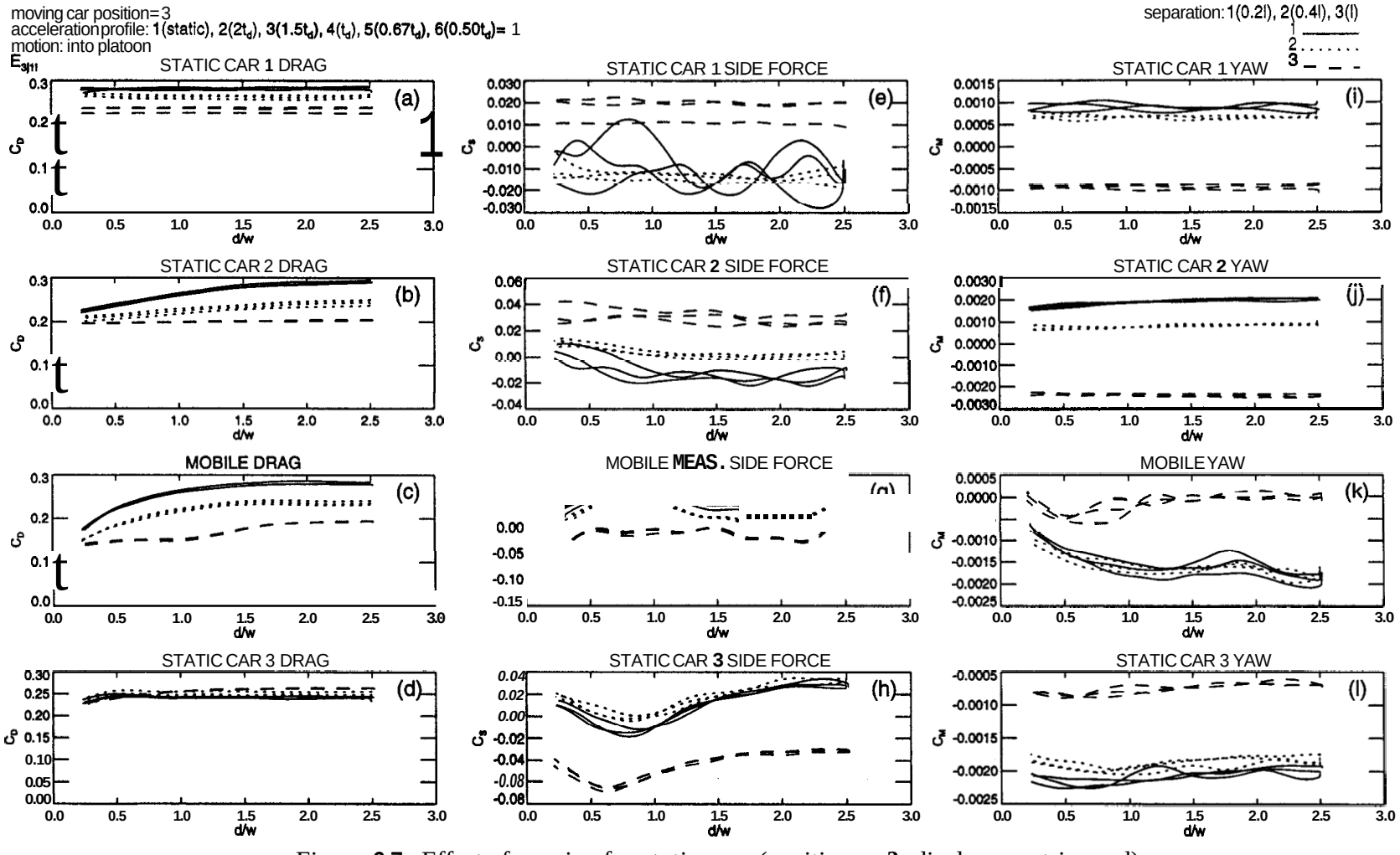

Figure **6.7:** Effect of spacing for static case (position = **3,** displacement inward). The drag [frames (a)-(d)], side force [frames(e)-(h)], and yawing moment [frames(i)-(l)] coefficients on each car are shown with respect to lateral displacement of the mobile car. The different lines represent the three inter-vehicle spacings.

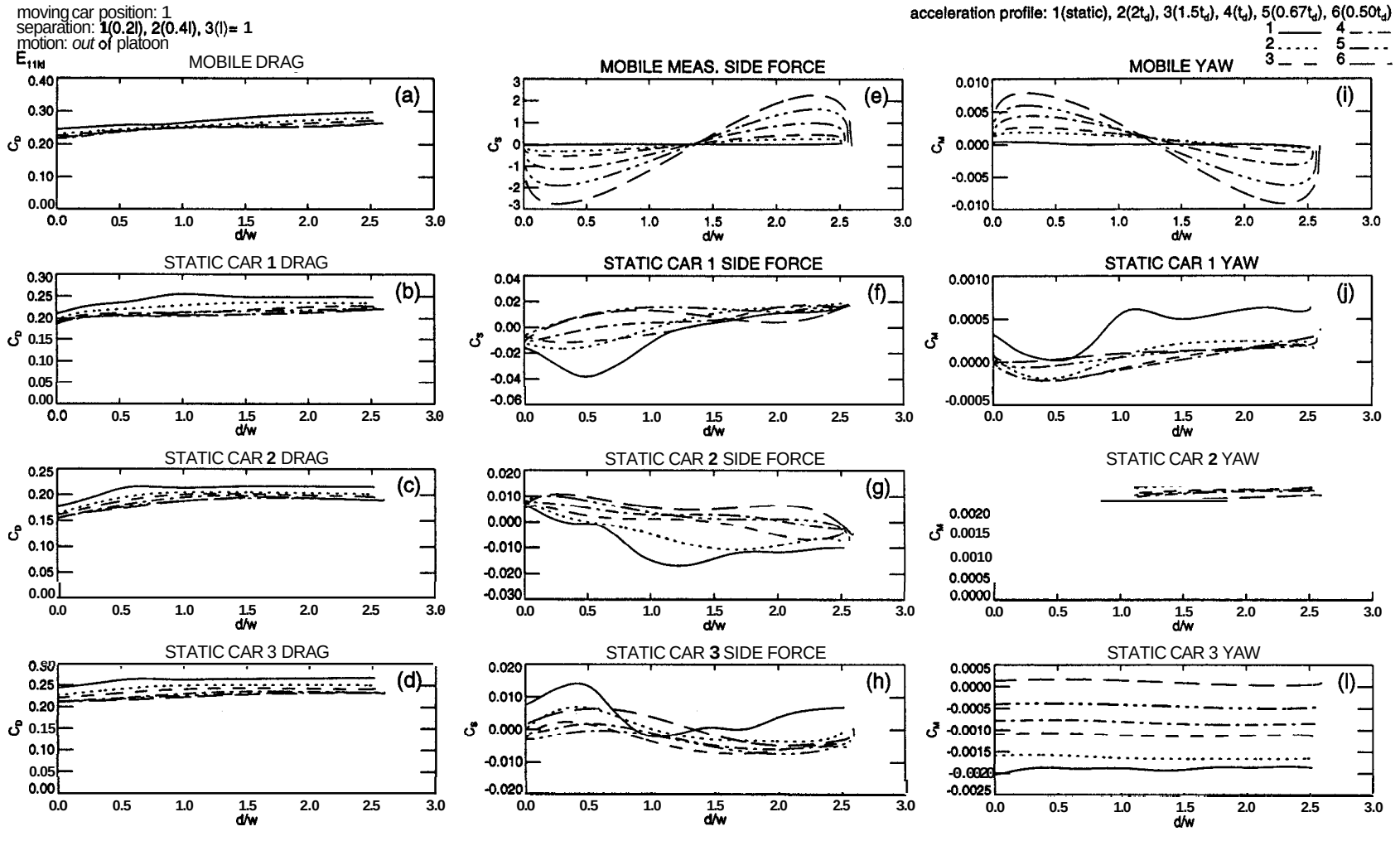

Figure ***6.8:*** Effect of acceleration (position = 1, separation = ***0.21,*** motion outward). The drag [frames (a)-(d)], side force [frames(e)-(h)], and yawing moment [frames(i)-(l)] coefficients on each car are shown with respect to lateral displacement of the mobile car. The different lines represent the *six* acceleration profiles of the mobile car.

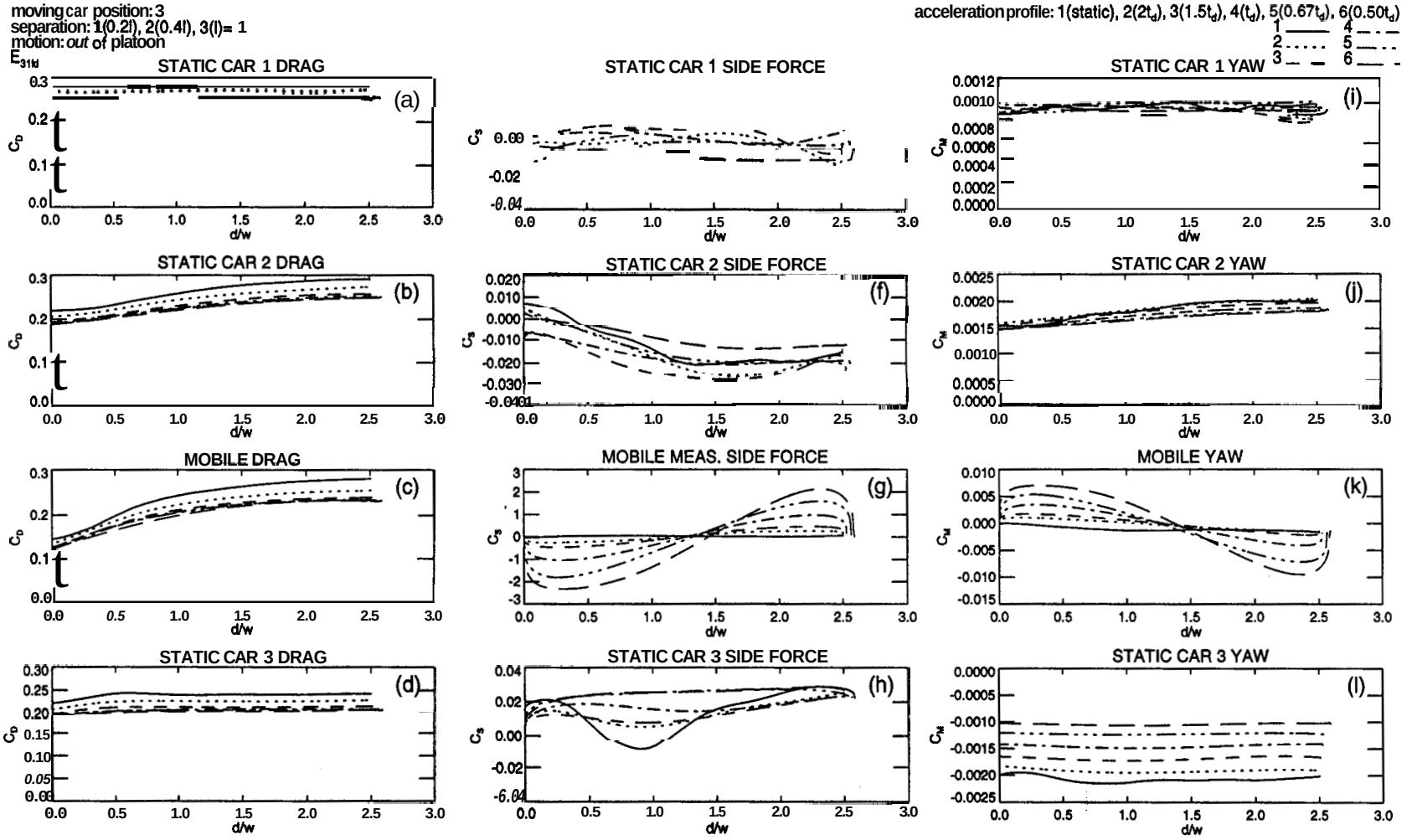

Figure **6.9:** Effect of acceleration (position = **3,** separation = **0.22,** motion outward). The drag [frames (a)-(d)], side force [frames(e)-(h)], and yawing moment [frames(i)-(l)] coefficients on each car are shown with respect to lateral displacement of the mobile car. The different lines represent the *six* acceleration profiles of the mobile car.

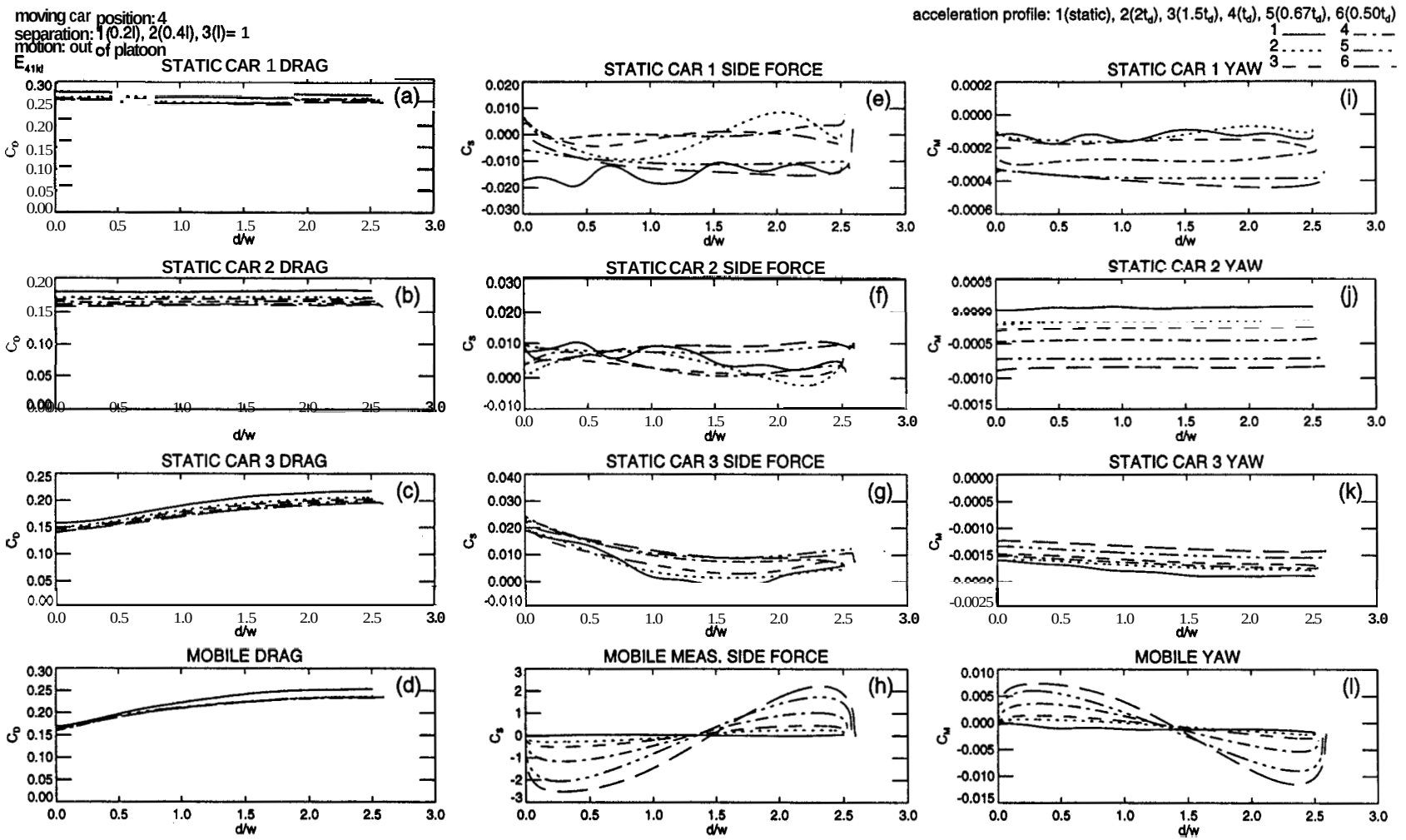

Figure 6.10: Effect of acceleration (position = **4,** separation = ***0.21,*** motion outward). The drag [frames (a)-(d)], side force [frames(e)-(h)], and yawing moment [frames(i)-(l)] coefficients on each car are shown with respect to lateral displacement of the mobile car. The different lines represent the ***six*** acceleration profiles of the mobile car.

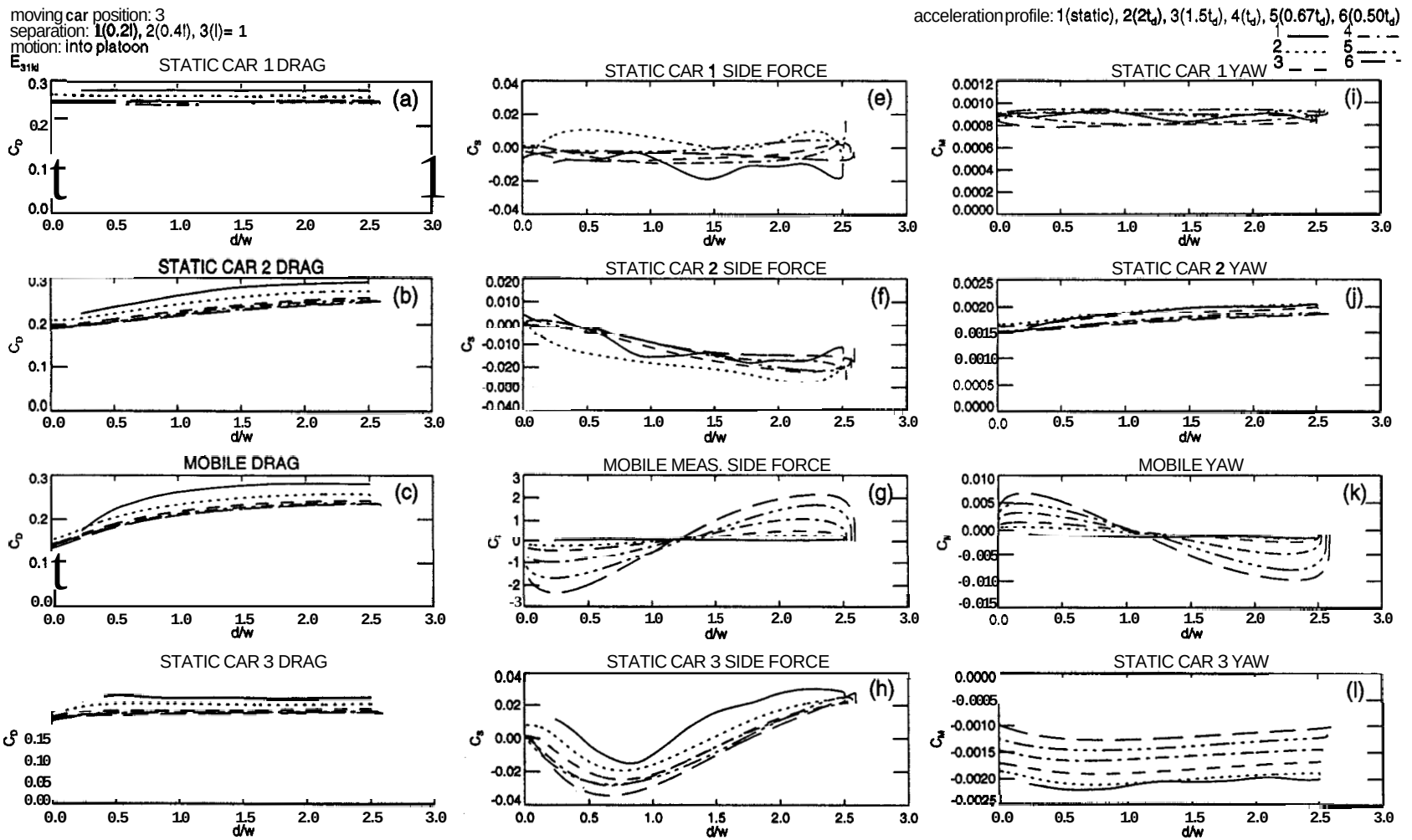

Figure 6.11: Effect of acceleration (position = 3, separation = *0.21*, motion inward). The drag [frames (a)-(d)], side force [frames(e)-(h)], and yawing moment [frames(i)-(l)] coefficients on each car are shown with respect to lateral displacement of the mobile car. The different lines represent the *six* acceleration profiles of the mobile car.

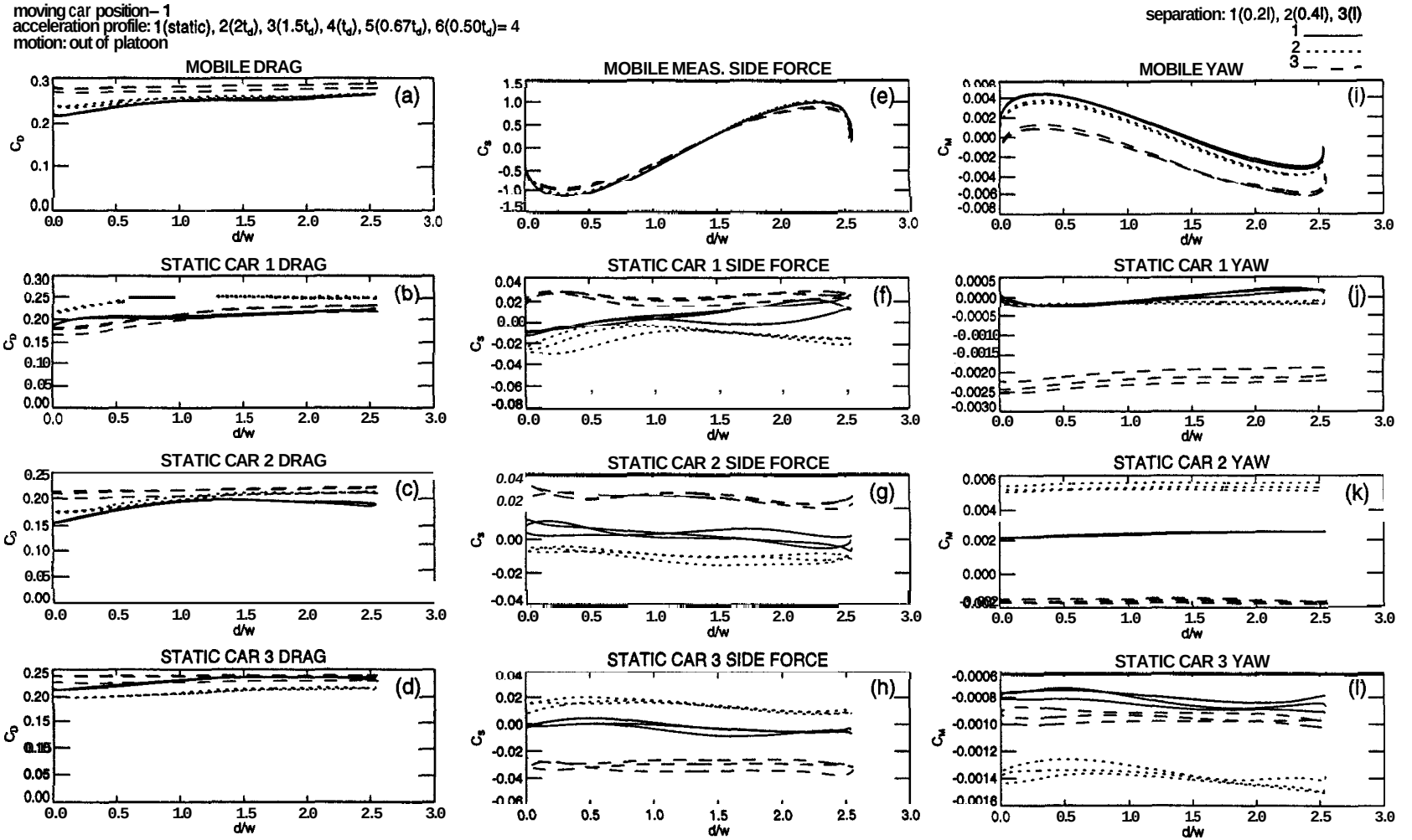

Figure **6.12:** Effect of spacing (position = **1,** acceleration = **4** motion outward). The drag [frames (a)-(d)], side force [frames(e)-(h)], and yawing moment [frames(i)-(l)] coefficients on each car are shown with respect to lateral displacement of the mobile car. The different lines represent the three inter-vehicle spacings.

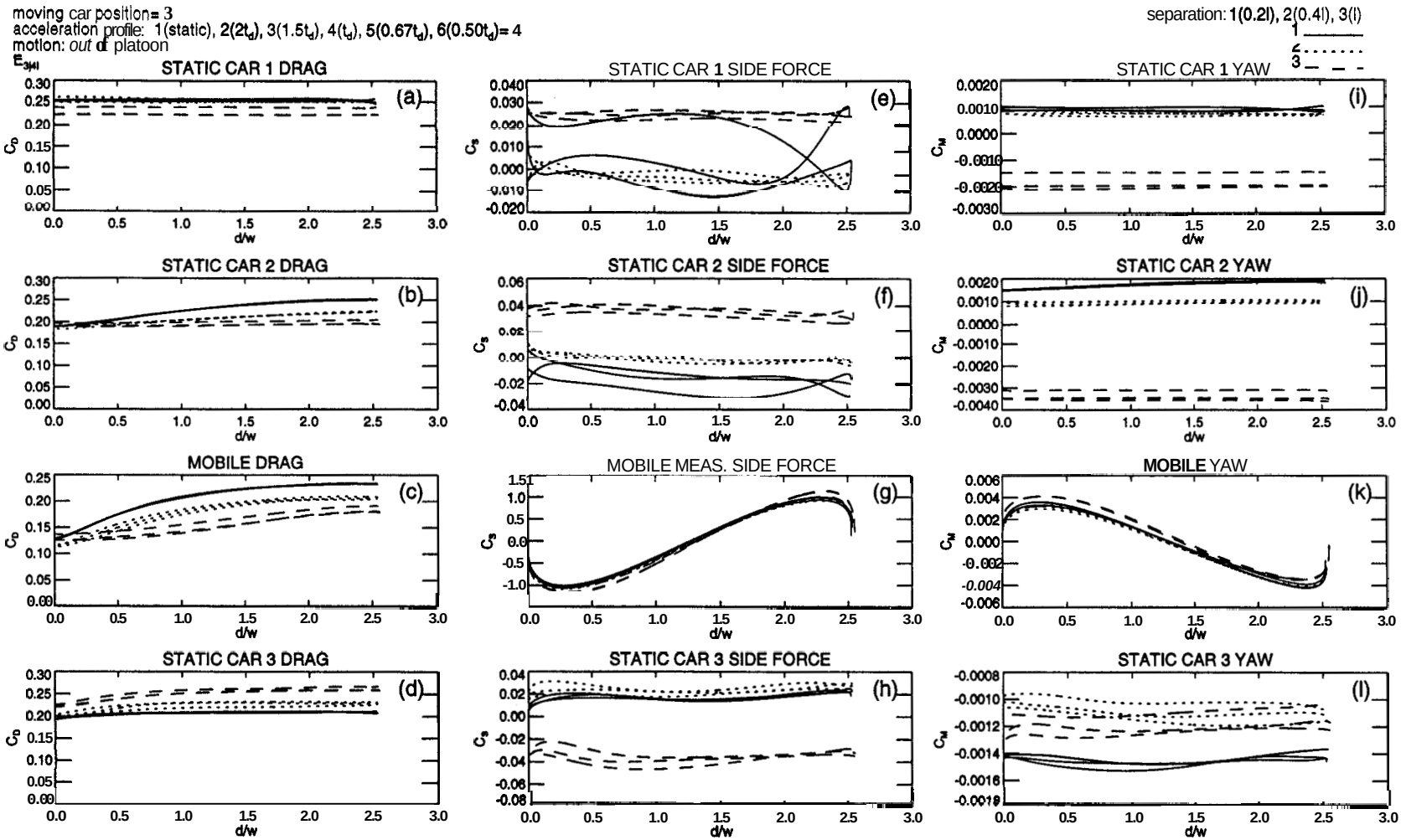

Figure 6.13: Effect of spacing (position = 3, acceleration = 4, motion outward). The drag [frames (a)-(d)], side force [frames(e)-(h)], and yawing moment [frames(i)-(l)] coefficients on each car are shown with respect to lateral displacement of the mobile car. The different lines represent the three inter-vehicle spacings.

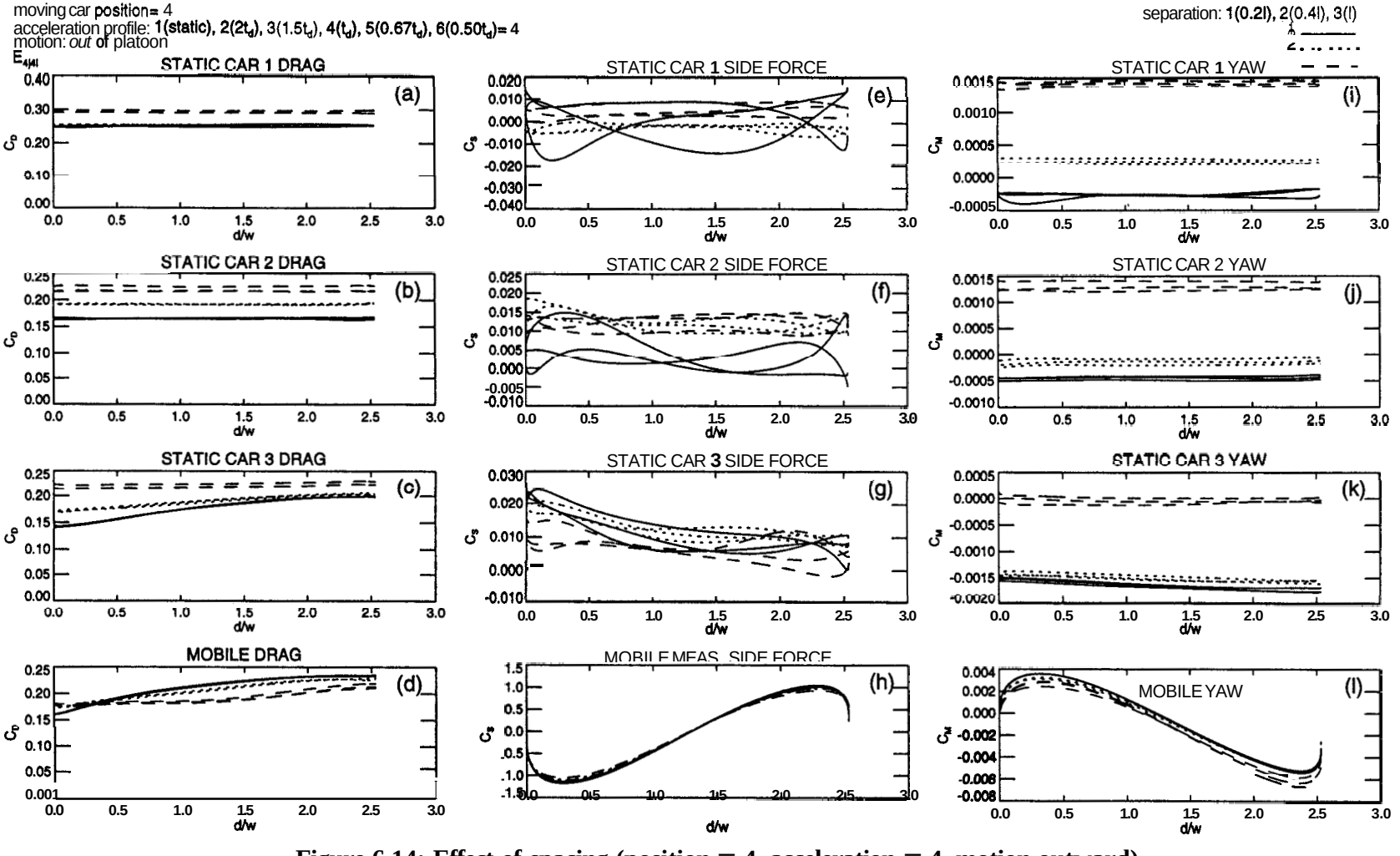

Figure 6.14: Effect of spacing (position = 4, acceleration = 4, motion outward). The drag [frames (a)-(d)], side force [frames(e)-(h)], and yawing moment [frames(i)-(l)] coefficients on each car are shown with respect to lateral displacement of the mobile car. The different lines represent the three inter-vehicle spacings.

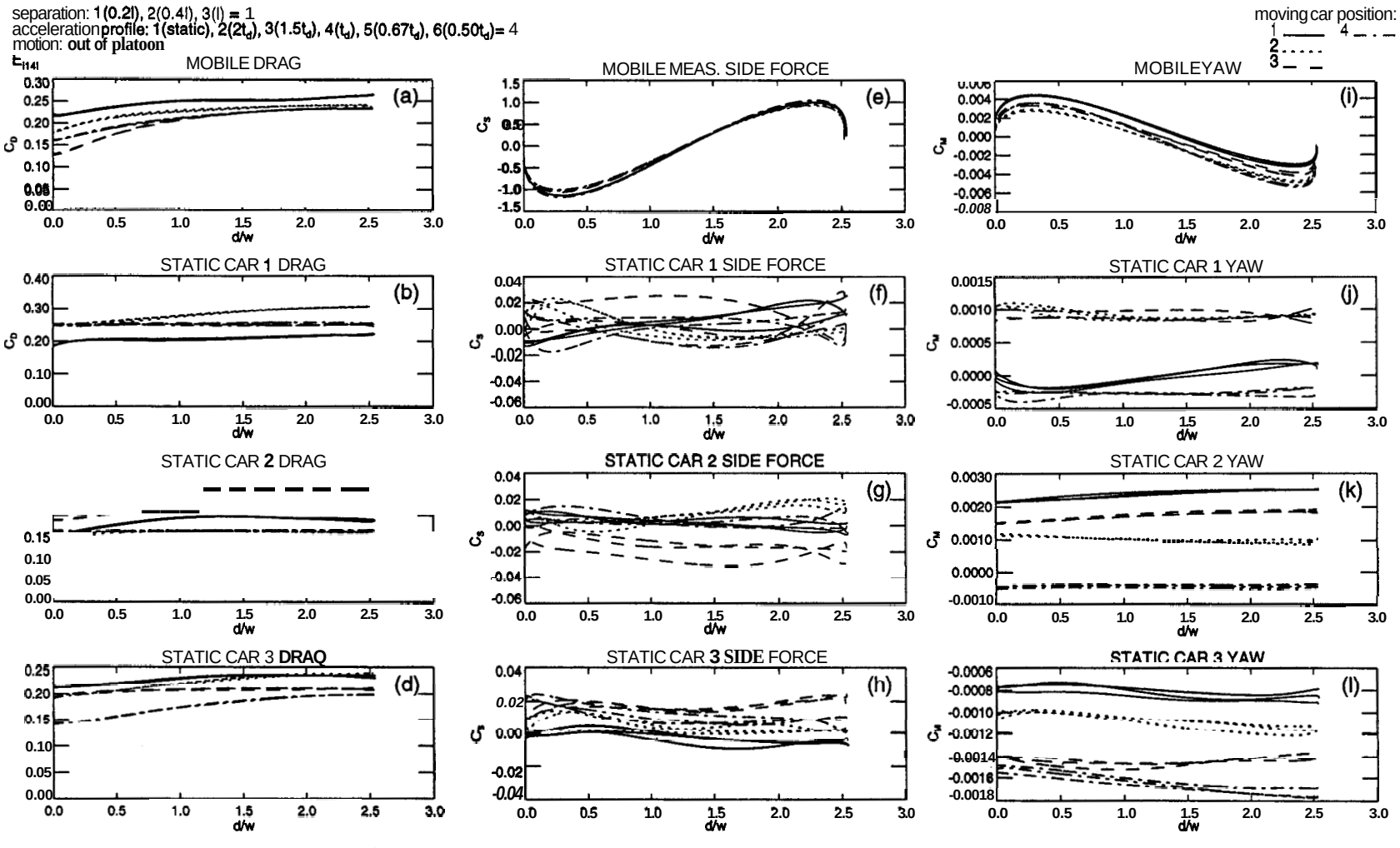

Figure **6.15:** Effect of location (spacing = **0.22,** acceleration = **4,** motion outward). The drag [frames (a)-(d)], side force [frames(e)-(h)], and yawing moment [frames(i)-(l)] coefficients on each car are shown with respect to lateral displacement of the mobile car. The different lines represent the four possible locations of the mobile car in the platoon.

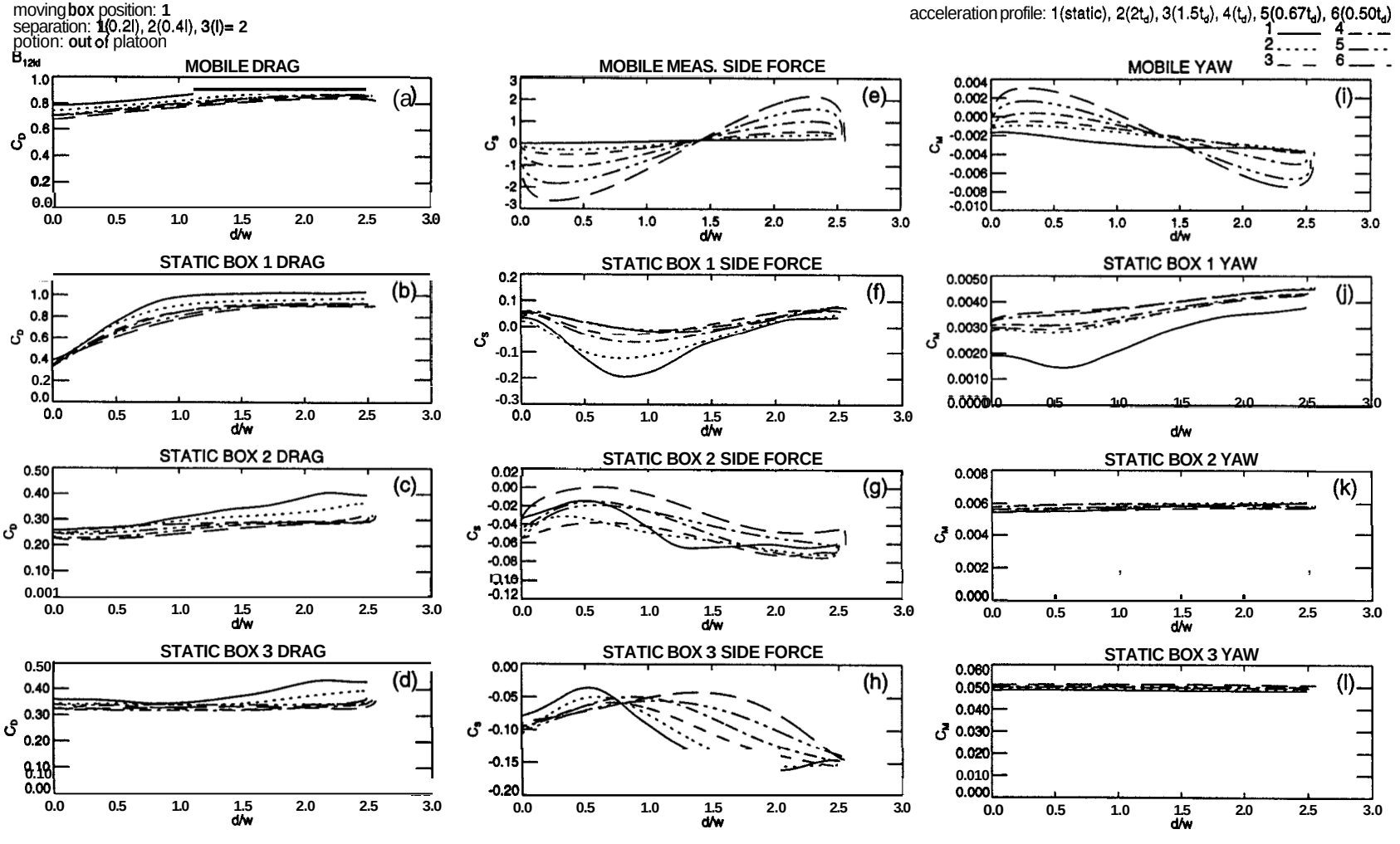

Figure **6.16:** Effect of acceleration, boxes (position = **1,** separation = **0.41,** motion outward). The drag [frames (a)-(d)], side force [frames(e)-(h)], and yawing moment [frames(i)-(l)] coefficients **on** each box are shown with respect to lateral displacement of the mobile box. The different lines represent the **six** acceleration profiles of the mobile box.

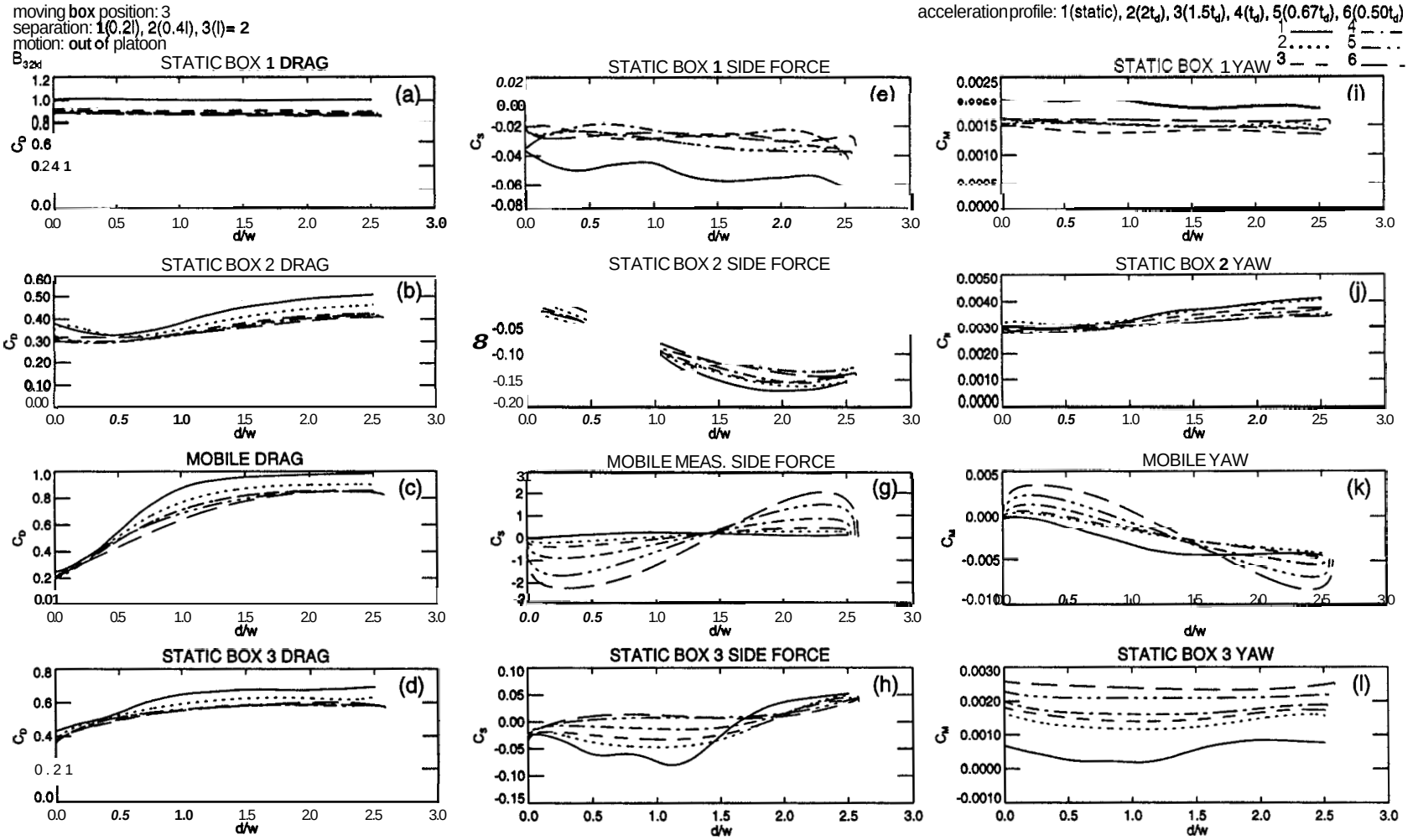

Figure 6.17: Effect of acceleration, boxes (position = **3,** separation = **0.41,** motion outward). The drag [frames (a)-(d)], side force [frames(e)-(h)], and yawing moment [frames(i)-(l)] coefficients on each box are shown with respect to lateral displacement of the mobile box. The different lines represent the *six* acceleration profiles of the mobile box.

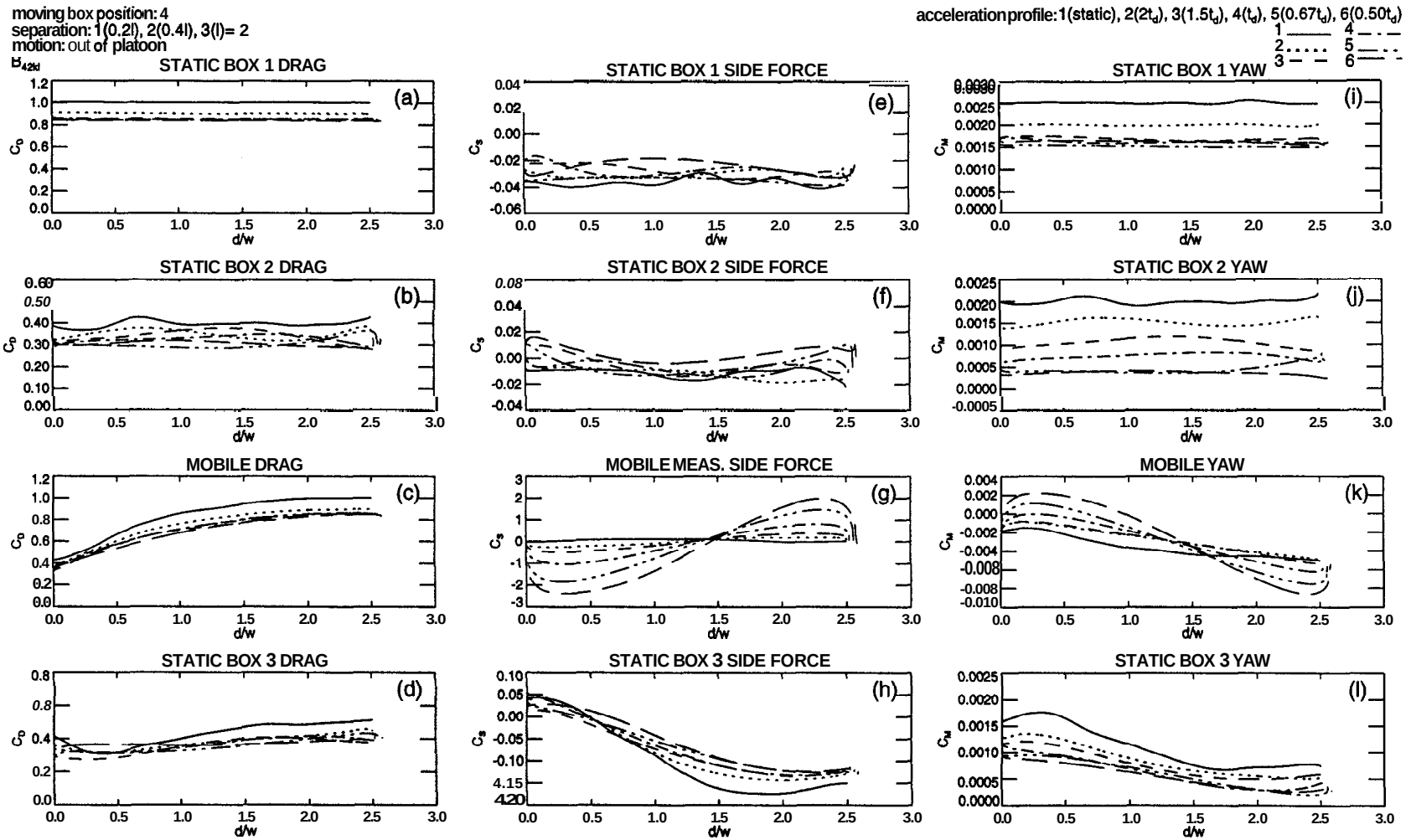

Figure 6.18: Effect of acceleration, boxes (position = **4,** separation = **0.42,** motion outward). The drag [frames (a)-(d)], side force [frames(e)-(h)], and yawing moment [frames(i)-(l)] coefficients on each box are shown with respect to lateral displacement of the mobile box. The different **lines** represent the *six* acceleration proiiles of the mobile box.

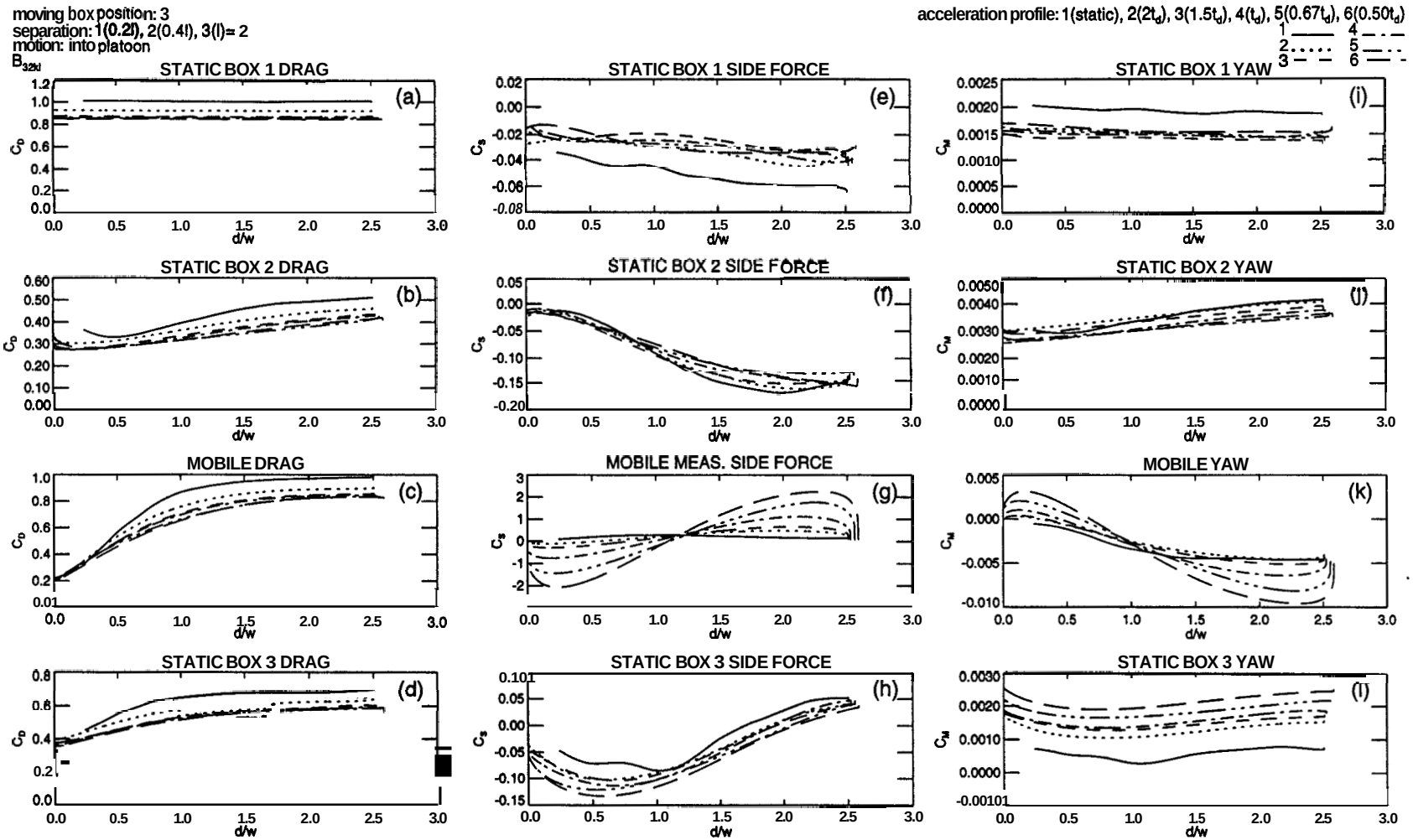

Figure 6.19: Effect of acceleration, boxes (position = 3, separation = $0.4l$, motion inward). The drag [frames (a)-(d)], side force [frames(e)-(h)], and yawing moment [frames(i)-(l)] coefficients on each box are shown with respect to lateral displacement of the mobile box. The different lines represent the *six* acceleration profiles of the mobile box.

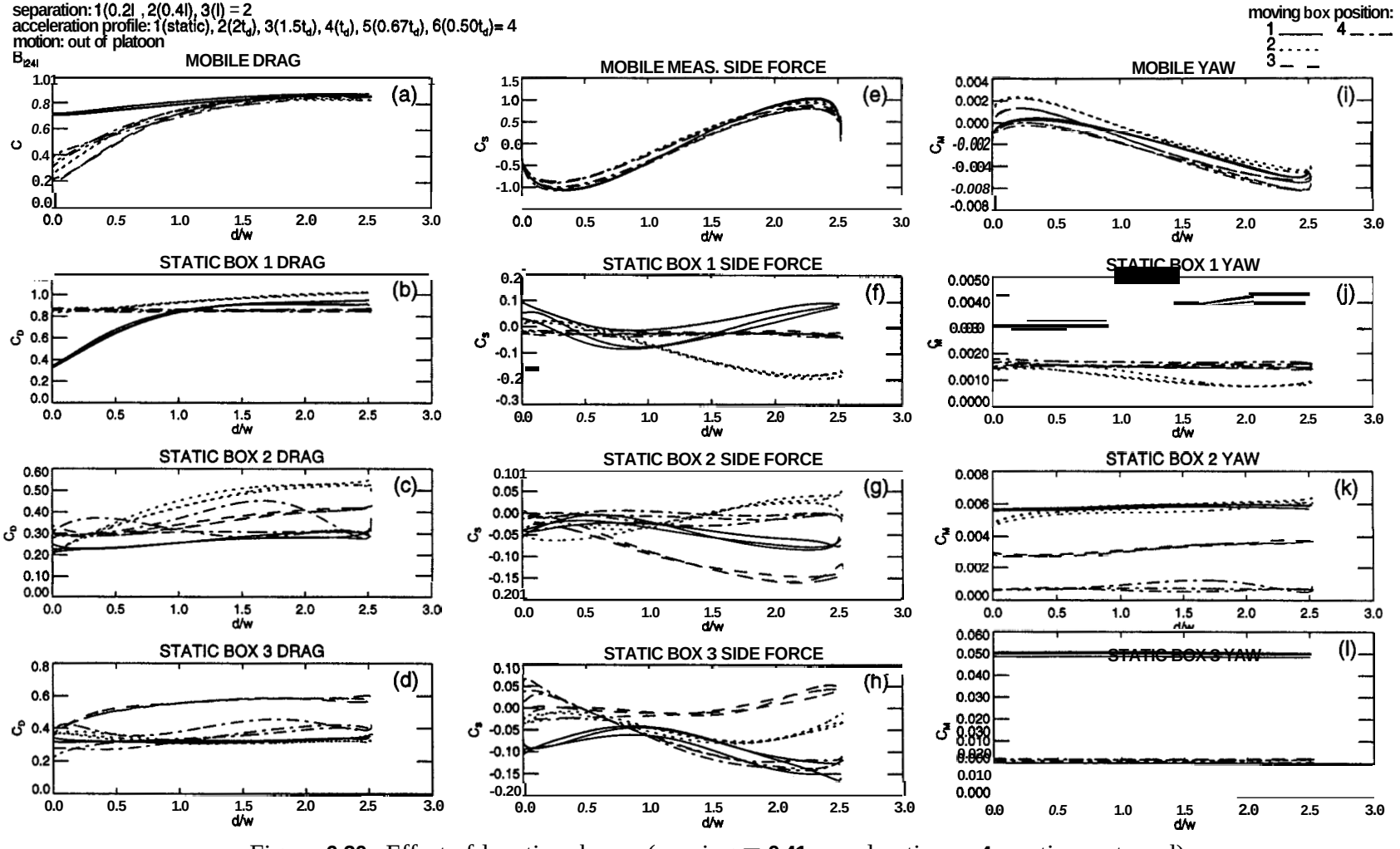

Figure **6.20:** Effect of location, boxes (spacing = **0.41,** acceleration = **4,** motion outward). The drag [frames (a)-(d)], side 'force [frames(e)-(h)], and yawing moment [frames(i)-(l)] coefficients on each box are shown with respect to lateral displacement of the mobile box. The different lines represent the four possible locations of the mobile box in the platoon.

Chapter 7

Platoon Aerodynamics

Placing vehicles in a platoon configuration results in several interesting effects. The behavior of the flow around a platoon of vehicles is markedly different from the flow around a single vehicle, as manifested in the different drag coefficients. During a lane change maneuver, side forces and moments are observed on all of the vehicles in a platoon. These forces and moments are a result of the transient aerodynamics of the flow. Some explanation for these observations are discussed below. Further explanation of the flow dynamics requires visualization of the flow.

7.1 Drag Coefficient

A significant reduction in drag is achieved for all vehicles in a platoon over the case of a single vehicle. By platooning, the separate vehicles are able to take advantage of the flow around other closely spaced vehicles. A single vehicle experiences drag as a result of pressure differences over the surface of the vehicle. The front of the vehicle experiences a high pressure from the oncoming flow, while the back of the vehicle experiences a low pressure due to separation of the flow from the vehicle surface and the resulting turbulent

wake. In a platoon, the vehicles experience smaller pressure differences over their surfaces. The lead vehicle in a platoon does not produce a low pressure turbulent wake because of the presence of the vehicle behind it. Thus, its drag is lower than that of a single vehicle. The last vehicle in the platoon does not experience the freestream velocity, resulting in smaller pressure differences over the vehicle and less drag. The internal members of the platoon experience neither the freestream flow nor the low pressure of a turbulent wake. The pressure differences over these vehicles are the smallest, resulting in the largest reduction in drag over that of an isolated vehicle. The closer the vehicles are spaced, the more they appear as a single vehicle to the oncoming flow. Therefore, a greater reduction in drag is possible, especially for the internal members of the platoon.

When a vehicle leaves the platoon, the streamlined flow is interrupted as the vehicle crosses the shear layer into the freestream flow. The resulting gap in the platoon results in an increase in drag for all of the vehicles, since the flow is no longer streamlined. The vehicle just ahead of the gap generates a turbulent wake, creating a low pressure area and causing an increase in its drag. The vehicle after the gap may experience shed vortices from the vehicle ahead or effects from the freestream, thus, increasing its drag. The maneuvering vehicle also experiences an increase in drag as it leaves the shelter of the platoon and is fully exposed to the oncoming flow. When it is located $2.5w$ away from the platoon, the maneuvering vehicle is not affected by the flow fields of the other members of the platoon and behaves as a single vehicle.

7.2 Transient Forces and Moments

Since the changes in the side force are on the same order as the changes in the drag, understanding the flow dynamics for the transient forces and moments generated

during a lane change maneuver is also important. When one vehicle is moved slowly out of the platoon, equivalent to making static measurements sequentially at several lateral displacements, the vehicles closest to the displaced vehicle are affected the most, since they are closest to the disturbance in the streamlined flow around the platoon. The side forces resulting on the remaining members of the platoon, both ahead of and behind the displaced vehicle, are in a direction opposite to the displacement up to a lateral distance of $0.5w - 1w$. This may be caused by vortex shedding from the edges of the vehicles as the displaced vehicle crosses the shear layer into the freestream. Once the displaced vehicle clears the edge of the platoon, the side forces on the vehicles behind it change direction to the same direction as the displacement. The turbulent wake of the displaced vehicle creates a low pressure area behind it. Thus, the pressure on the following vehicles is less on the same side as the displacement than the pressure on the freestream side, and the vehicles experience a force in the same direction as the displacement. If a vehicle is moved slowly into the platoon, mimicking static measurements, the side force exhibits the same trends, though the direction of displacement is different. Therefore, the side forces resulting from a vehicle displaced in slow increments out of the platoon are the same as those resulting from a vehicle entering a platoon in slow increments.

When the mobile vehicle moves out of the platoon on a *time scale of* t_d, which is equivalent to the time scale of an actual lane change, or faster, the following vehicles now experience a side force in the same direction as the motion for all lateral displacements. Apparently, the effects of vortex shedding from the edges of the vehicles are obscured in the quickly generated turbulent wake of the mobile vehicle. The low pressure of the wake causes the following vehicles to experience a force in the same direction as the motion of the mobile vehicle. However, when a vehicle moves into the platoon, the same side forces on the

vehicles following the maneuvering vehicle are not produced. For motion into the platoon, the following vehicles are pushed laterally out of the platoon by the fluid displaced by the mobile vehicle. This side force decreases as the maneuvering vehicle joins the platoon and the flow becomes streamlined. Thus, *the side force is now a direct result of the direction of the maneuver*. This nonmonotonic behavior is not observed in *steady measurements nor on the vehicles ahead of the maneuvering vehicle.*

7.3 Bluff Body Shapes

By comparing the results for a platoon of cars with the results for a platoon of rectangular boxes, the transient aerodynamics are obviously heavily influenced by the shape and size of the vehicles. The more streamlined shape of the cars results in smaller changes in the force coefficients. The rectangular boxes, with their more blunt shape and sharp corners, produce larger and more turbulent wakes [18]. These result in larger forces measured during the transient motion of the box simulating a lane change. A platoon of mixed vehicles will undoubtedly result in forces of different magnitudes, depending upon the specific arrangement of the vehicles. For example, a small vehicle in the wake of a larger vehicle will produce different forces compared to the case of a large vehicle in the wake of a smaller vehicle. The results here are useful in identifying trends which apply to the many cases of different vehicle shapes and sizes.

Chapter 8

Conclusions

This research has immediate application to the California Partners for Advanced Transit and Highways (PATH) automated highway system. In this system, computer controlled vehicles travel in "platoons" consisting of approximately twenty cars aligned in single-file and spaced less than one vehicle length apart. The vehicles in the platoon experience transient aerodynamic forces and moments as vehicles leave and join the platoon at various locations. A platoon of scale vehicle models is placed in a wind tunnel and measurements are made of the transient forces and moments as one of the vehicles is moved into and out of the platoon. The results from the wind tunnel experiments allow the computer vehicle control algorithms to better predict the transient aerodynamics that the vehicles in the platoon encounter during leaving and joining maneuvers. In addition, these results apply to bluff-body aerodynamics. First, a summary of the static results of these experiments is presented. The major conclusions of the transient results are discussed next. Some final comments on possible extensions of this research are also presented.

8.1 Summary of Static Results

The drag, side force, and yawing moment are measured for a single car and each car in a four-car platoon. Several spacings between the vehicles in the platoon are used. **All** cars in the platoon experience a reduction in drag over the single vehicle case. The largest reduction in drag occurs for the smallest inter-vehicle spacing. **A** maximum drag reduction of **40%** is achieved for the third car in the platoon. These results are comparable to previously published results on drag reduction in a platoon. In addition, by moving one car out of and into the platoon on a time scale much slower than that of the oncoming flow, measurements are obtained for several lateral displacements of one vehicle from the platoon. Measurements are made with the displaced vehicle as each of the four members of the platoon. The increase in the drag on the remaining cars in the platoon as one vehicle leaves confirms that the close spacing between vehicles in a platoon results in streamlined flow. **All** of the cars experience side forces and yawing moments resulting from the interrupted flow field caused by the displaced car. These results are consistent regardless of the location of the displaced car in the platoon and the direction of the lateral displacement, i.e. moving out of or into the platoon. These effects are more pronounced on the bluff shape of a single rectangular box and a platoon of boxes. **As** with the car platoon, the largest drag reduction is achieved at the smallest inter-vehicle spacing. Because of the bluff shape and, thus, higher drag coefficient of a single box, a larger reduction in drag is achieved for the boxes from platooning. The third box in the platoon experiences the largest drag reduction of 70%.

8.2 Summary of Transient Results

The major contribution of this research is characterization of the transient forces. When a lane change, either leaving or joining a platoon, maneuver occurs on the same time

scale as changes in the flow field, determining the transient forces and moments becomes of paramount importance. One vehicle is moved out of and into the platoon at six different accelerations to simulate lane changes at six different time scales, the longest (smallest acceleration) representing the static case and the shortest (largest acceleration) representing half of the nominal time of an actual lane change. The drag on a vehicle results from pressure differences in the flow direction and does not depend upon the direction of the lane change. However, the side forces experienced by the remaining members of the platoon behind the maneuvering vehicle depend upon whether a car is leaving or joining the platoon. When the maneuver occurs on a time scale *shorter than the design time scale* t_d, which is equivalent to the time scale of a lane change by an actual vehicle, the side forces on the cars *behind the maneuvering car differ when the car leaves and when the car joins the platoon.* This hysteresis is observable at all inter-vehicle spacings and all locations of the maneuvering vehicle in the platoon. Thus, the transients from the interacting flow fields retain knowledge of their history and are a direct result of the specifics of how they are generated. This nonmonotonic nature of the transient side force would not be observable in steady state measurements as the static results here have shown. Interestingly, this hysteresis in the side force *does not appear on cars ahead of the maneuvering car.* In addition, *changes in the side force are on the same order as changes in the drag* for all of the vehicles in the platoon. Therefore, the change in the side force experienced by a vehicle as a result of a lane change maneuver has as much effect on the vehicle's controllability as the change in the drag. To improve controllability of the IVHS vehicles and increase passenger safety, the behavior of these transient forces should be taken into account in designing the vehicle control algorithms. Changes in the yawing moment are difficult to measure with the current models; thus, no definitive conclusions about the moments experienced by the vehicles can

be made with the current data.

Measurements are made with the maneuvering vehicle as a different member of the four-car platoon in the experiments. The longitudinal spacing between the vehicles is also varied. The results show that the greatest changes occur at the smallest inter-vehicle spacing. In addition, the magnitude of the change depends upon the relative location of a member in the platoon to the maneuvering vehicle. The vehicles closest to the maneuvering vehicle experience the largest changes, but the transients also depend upon whether the vehicle is ahead of or behind the maneuvering vehicle.

Measurements on a platoon of boxes with the same overall dimensions as the cars show that the forces are heavily influenced by the shape of the bodies. Therefore, the aerodynamics of a platoon of mixed vehicles will depend upon the specifics of their various shapes, sizes, and arrangement. *The less streamlined shape of the boxes typically resulted in larger changes in the forces,* though the general trends are similar to those of the platoon of cars. In particular, the box platoon exhibited the same nonmonotonic behavior as the car platoon in the side forces on the boxes behind the maneuvering box. The side forces experienced by the boxes *following the maneuvering box during a leaving maneuver differed from those during a joining maneuver, when the maneuver occurred on a time scale shorter than the time scale* t_d of a lane change by a full scale vehicle. Again, this hysteresis in the side force *did not occur for boxes ahead of the maneuvering box.*

8.3 Final Remarks

These results can be summarized as functions of their variables to provide input to the vehicle controllers. The careful design and construction of the experimental hardware and software resulted in extreme robustness and linearity of the instrumentation. However,

finer measurements of the yawing moment require the use of lighter models. In addition, a more sensitive accelerometer should be used to measure the mobile car's acceleration and extract its inertial force from the measured side force to obtain the actual transient force due to the flow. Also, visualization of the flow and velocity field measurements will provide a better understanding of the flow dynamics.

The results of this research can be extended to the more general case of transient flow around bluff bodies. Some additional experiments are planned on basic shapes, such as cylinders, boxes, and spheres, and simplified scale vehicles in a water towing tank. Particle image velocimetry (PIV) measurements will provide velocity fields at cross-sections in the flow and some visualization. Other interesting situations include the passing of a platoon by a single car or another platoon of cars and the longitudinal oscillation of a car within a platoon. Preliminary measurements show that the members of a platoon are significantly affected by a car placed next to the platoon to simulate passing, and the degree of these effects depend upon their lateral separation [28]. These areas will be explored in future experiments as additions and modifications to this research.

Bibliography

[1] J. K. Hedrick, M. Tomizuka, and P. Varaiya. Control issues in automated highway systems. *IEEE Control Systems*, December:21–32, 1994.

[2] S. E. Shladover. The California path program: a state approach to ivhs research. 1992. SAE Paper No. 92C018.

[3] W.-H. Hucho and G. Sovran. Aerodynamics of road vehicles. In *Annual Review of Fluid Mechanics*, volume 25, pages 485–537. Annual Reviews Inc., Palo Alto, CA, 1993.

[4] G. Sovran, T. Morel, and W. T. Jr. Mason eds. *Aerodynamic Drag Mechanisms of Bluff Bodies and Road Vehicles*. Plenum Press, New York, 1978.

[5] A. J. Scibor-Rylski. *Road Vehicle Aerodynamics*. Pentech Press, London, 1975.

[6] M. Zabat, S. Frascaroli, and F. Browand. Drag measurements of a platoon of vehicles. 1994. PATH Report No. UCB-ITS-PRR-93-27.

[7] M. Zabat, N. Stabile, S. fiascaroli, and F. Browand. The aerodynamic performance of platoons: A final report. 1995. PATH Report No. UCB-ITS-PRR-95-35.

[8] N. Kobayashi and Y. Sasaki. Aerodynamics effects of an overtaking articulated heavy goods vehicle on car-trailer - an analysis to improve controllability. 1987. SAE Paper No. 871919.

[9] M. Sano, T. Nagahisa, and T. Kobayashi. Unsteady aerodynamical forces by interference of two bluff bodies moving closely. *Bulletin of JSME*, 27(226):675–682, 1984.

[10] D. P. Telionis, C. J. Fahrner, and G. S. Jones. An experimental study of highway aerodynamic interferences. *Journal of Wind Engineering and Industrial Aerodynamics*, 17:267–293, 1984.

[11] A. F. A. Azim. An experimental study of the aerodynamic interference between road vehicles. 1994. SAE Paper No. 940422.

[12] R. K. Heffley. Aerodynamics of passenger vehicles in close proximity to trucks and buses. 1973. SAE Paper No. 730235.

[13] N. Shiraishi, M. Matsumoto, and H. Shirato. On aerodynamic instabilities of tandem structures. *Journal of Wind Engineering and Industrial Aerodynamics*, 23:437–447, 1986.

[14] T. Ota and H. Nishiyama. Flow around two elliptic cylinders in tandem arrangement. *Transactions of the ASME Journal of Fluids Engineering*, 108:98–103, 1986.

[15] T. Morel and M. Bohn. Flow over two circular disks in tandem. *Transactions of the ASME Journal of Fluids Engineering*, 102:104–111, 1980.

[16] J. W. Alan. Aerodynamic drag and pressure measurements on a simplified tractor-trailer model. *Journal of Wind Engineering and Industrial Aerodynamics*, 9:125–136, 1981.

[17] J. Howell. Catastrophic lift forces on racing cars. *Journal of Wind Engineering and Industrial Aerodynamics*, 9:145–154, 1981.

[18] K. Koenig and A. Roshko. An experimental study of geometrical effects of the drag and flow field of two bluff bodies separated by a gap. *Journal of Fluid Mechanics,* 156:167–204, 1985.

[19] M. M. Zdravkovich. Review of flow interference between two circular cylinders in various arrangements. *Transactions of the ASME Journal of Fluids Engineering,* December:618–633, 1977.

[20] P. Michael. Ideal flow along a row of spheres, *Physics of Fluids,* 8(7):1263–1266, 1965.

[21] X. Cai and G. B. Wallis. Potentia3 flow around a row of spheres in a circular tube. *Physics of Fluids A,* 4(5):904–912, 1992.

[22] G. K. Batchelor. *An Introduction to Fluid Dynamics.* Cambridge University Press, New **York,** 1990.

[23] W. Chee and M. Tomizuka. Vehicle lane change maneuver in automated highway systems. 1994. PATH Report No. UCB-ITS-PRR-94-22.

[24] L. Rosenhead ed. *Laminar Boundary Layers.* Dover, New York, 1988.

[25] P. **A.** Snyder. Control implications in platoon aerodynamics. Master's thesis, University of California, Berkeley, 1998.

[26] W. H. Press, S. **A.** Teukolsky, W. T. Vetterling, and B. P. Flannery. *Numerical Recipes in Fortran 90.* Cambridge University Press, New York, 1996.

[27] A. L. Chen, K. Hedrick, and 0. Savaş. Transient aerodynamics in vehicle interactions: Data base summary. 1997. PATH Report No. UCB-ITS-PRR-97-50.

[28] L. Tsuei. Private communication, 1997. University of California, Berkeley.